Three-dimensional fluorescence image analysis of megakaryocytes and vascular structures in intact bone

Dreidimensionale Fluoreszenzbildanalyse von Megakaryozyten und Gefäßstrukturen in intaktem Knochen

Doctoral thesis for a medical doctoral degree
at the Graduate School of Life Sciences,
Julius-Maximilians-Universität Würzburg,
Section Biomedicine

submitted by

Patrick Alexander Gerhard Schmithausen

from

Neuss

Würzburg, August 2018

Submitted on:

…………………………………………………………..……..

Office stamp

Members of the Thesis Committee:

Chairperson:	**Prof. Dr. Andreas Rosenwald**
Primary Supervisor:	**Prof. Dr. Katrin Heinze**
Supervisor (Second):	**Prof. Dr. Dr. Andreas Beilhack**
Supervisor (Third):	**Prof. Dr. Bernhard Nieswandt**
Supervisor (Fourth): **(If applicable)**	

Date of Public Defence: …………………………………………….…………

Date of Receipt of Certificates: ………………………………………….

I. Acknowledgements

I would like to acknowledge the following people without whom this thesis could not have been completed.

Firstly, I would like to express my deep gratitude to my supervisor, Prof. Dr. Katrin Heinze, for her constant support, guidance and encouragement.

Furthermore, I would like to thank Prof. Dr. Dr. Andreas Beilhack and Prof. Dr. Bernhard Nieswandt for their support as members of my thesis committee and their insight during committee meetings.

I would also like to thank Oğuzhan Angay for his knowledge, patience and teamwork during the development of the imaging pipeline as well as the processing of the imaging data. Despite occasional despair due to a multitude of software crashes I will keep the time at the workstation next to Oğuzhan in good memory.

Additionally, I am grateful to Mike Friedrich, Jürgen Pinnecker, Dr. David Stegner, Dr. Judith M. M. vanEeuwijk and Maximilian G. Gorelashvili for constant and helpful feedback and fruitfuld discussions within the team of Teilprojekt B07.

Finally, I would like to thank my parents Birgit & Gerd for their constant support throughout the course of this thesis and during my whole studies.

II. Table of contents

III. List of abbreviations

Abbreviation	Description
2P-IVM	Two-photon intra-vital microscopy
AABB	American Association of Blood Banks
BABB	Benzylalcohol and benzylbenzoat
BM	Bone marrow
BN	Prof. Dr. Bernhard Nieswandt
CPU	Central processing unit
CRC	Collaborative Research Centre
CS	cryo-sectioning
CXCR4+	CXC chemokine receptor type 4
DMS	Demarcation membrane system
DS	Dr. David Stegner
e.g.	exempli gratia
ECM	Extrazellular matrix
EDTA	Ethylenediaminetetraacetic acid
FGF-4	Fibroblast growth factor-4
GP Ib	Glycoprotein Ib
HSC	Hematopoietic stem cell
JE	Dr. Judith vanEeuwijk
JP	Jürgen Pinnecker
JPEG	Joint photographic experts group
KH	Prof. Dr. Katrin Heinze
LSCM	Laser scanning confocal microscopy
LSFM	Light sheet fluorescence microscope
MF	Mike Friedrich
MG	Maximilian Gorelashvil
MIP	Maximum intensity projection
MK	Megakyroocyte
MK10	Megakaryocytes of diameter above 10µm
MK20	Megakaryocytes of diameter above 20µm
OA	Oğuzhan Angay
PFA	Paraformaldehyde
PNG	Portable network graphics
PPF	Proplatelet formation
PS	Patrick Schmithausen
RAM	Random access memory
RI	Refractive index

ROIs	Regions of interest
RVC	Rudolf-Virchow Center
SDF-1	Stromal-derived factor 1
SFB	Sonderforschungsbereich
SQP	Square pixels (sqp)
TIFF	Tagged image file format
TP B07	Sub-project B07
TPO	Thrombopoietin
VOXEL	Volumetric pixel
WAS	Wiscott-Aldrich syndrome
YFP	Yellow fluorescent protein

IV. List of figures

V. List of tables

1. Summary / Zusammenfassung

Summary

The thesis provides insights in reconstruction and analysis pipelines for processing of three-dimensional cell and vessel images of megakaryopoiesis in intact murine bone. The images were captured in a Light Sheet Fluorescence Microscope. The work presented here is part of Collaborative Research Centre (CRC) 688 (project B07) of the University of Würzburg, performed at the Rudolf-Virchow Center. Despite ongoing research within the field of megakaryopoiesis, its spatio-temporal pattern of megakaryopoiesis is largely unknown. Deeper insight to this field is highly desirable to promote development of new therapeutic strategies for conditions related to thrombocytopathy as well as thrombocytopenia. The current concept of megakaryopoiesis is largely based on data from cryosectioning or *in vitro* studies indicating the existence of spatial niches within the bone marrow where specific stages of megakaryopoiesis take place. Since classic imaging of bone sections is typically limited to selective two-dimensional views and prone to cutting artefacts, imaging of *intact* murine bone is highly desired. However, this has its own challenges to meet, particularly in image reconstruction. Here, I worked on processing pipelines to account for irregular specimen staining or attenuation as well as the extreme heterogeneity of megakaryocyte morphology. Specific challenges for imaging and image reconstruction are tackled and solution strategies as well as remaining limitations are presented and discussed. Fortunately, modern image processing and segmentation strongly benefits from continuous advances in hardware as well as software-development. This thesis exemplifies how a combined effort in biomedicine, computer vision, data processing and image technology leads to deeper understanding of megakaryopoiesis. Tailored imaging pipelines significantly helped elucidating that the large megakaryocytes are broadly distributed throughout the bone marrow facing a surprisingly dense vessel network. No evidence was found for spatial niches in the bone marrow, eventually resulting in a revised model of megakaryopoiesis.

Zusammenfassung

Im Rahmen dieses Dissertationsvorhabens wurden Segmentierungs- und Auswertepipelines dreidimensionaler Bilder von Zellen und Gefäßen im intakten Mausknochen erarbeitet. Die Bilder entstanden durch Fluoreszenzaufnahmen eines Lichtblattmikroskops. Das Dissertationsvorhaben war Teil des Sonderforschungsbereichs 688 (Teilprojekts B07) der Universität Würzburg und es wurde am Rudolf-Virchow-Zentrum durchgeführt. Trotz einer Vielzahl aktueller Forschungsprojekte auf dem Gebiet der Megakaryopoese sind Erkenntnisse über deren räumlich-zeitliche Zusammenhänge größtenteils unbekannt. Neuere wissenschaftliche Erkenntnisse auf diesem Gebiet wären insbesondere hilfreich für die Weiterentwicklung von Behandlungsstrategien für Patienten, die an Thrombozytopenien oder Thrombozytopathien leiden. Das aktuell vorherrschende Modell zur Erklärung der Megakaryopoese geht von der Existenz räumlicher Nischen im Knochenmark aus, in denen sich die einzelnen Schritte der Megakaryopoese vollziehen. Dieses Modell basiert hauptsächlich auf Auswertungen von Gefrierschnitten sowie *in-vitro* Experimenten. Da die klassische Bildgebung von Knochenschnitten nur auf eine bestimmte Anzahl zweidimensionaler Schnitte begrenzt ist und deren Qualität unter Schnittartefakten leidet, ist die Bildgebung des intakten Knochens von besonderem Interesse. Dennoch führt dies zu neuen Herausforderungen im Bereich der Bilddatenauswertung. Im vorliegenden Dissertationsvorhaben beschäftige ich mich in diesem Bereich mit der Erarbeitung von Auswerteprotokollen, welche beispielsweise den Einfluss unregelmäßiger Färbungen oder Signalabschwächungen sowie die extreme Heterogenität der Megakaryozytenmorphologie berücksichtigen. Spezifische Herausforderungen für die Bildgebung und Bildrekonstruktion werden in Angriff genommen und Lösungsstrategien sowie verbleibende Einschränkungen werden vorgestellt und diskutiert. Erfreulicherweise profitieren insbesondere die moderne Bildbearbeitung sowie die Objekterkennung in großem Ausmaß von fortlaufenden Entwicklungen aus dem Hard- sowie Softwarebereich. Dieses Dissertationsvorhaben zeigt auf exemplarische Art und Weise auf, wie gemeinsame Forschungsanstrengungen im Bereich der Biomedizin, des Maschinellen Sehens, der Datenverarbeitung sowie der Bildtechnologie zu einem tieferen Verständnis der Megakaryopoese führen. Die maßgeschneiderten Pipelines zur Bilddatenauswertung stützten letztlich die These, dass größere Megakaryozyten im Knochenmark breit verteilt sind und von einem überraschend dichten Gefäßnetz umgeben sind. Beweise für die Existenz räumlicher Nischen im Knochenmark konnten nicht gefunden warden. Dieses führte schließlich zur Vorstellung eines überarbeiteten Modells der Megakaryopoese.

2. Cell-cell interactions within the cardiovascular system

Research within this thesis is part of project B07 (TP B07) within Collaborative Research Centre (CRC) 688 of the University of Würzburg, performed at the Rudolf-Virchow Center. Primary research focus of CRC 688 aims at investigating cell-cell interactions within the cardiovascular system (SFB688 2018). Key aspects of TP B07 consist of the development of imaging procedures allowing for a robust analysis of the 2P-IVM data as well as the results from LSFM. Once working imaging protocols are in place, pathogenesis of the processes involved in the thrombo-inflammatory pathways in context of acute stroke may be investigated by genetically or pharmacologically inactivating factors within this cascade *in situ*. Research within this thesis is dealing with the development and improvement of protocols for image analysis of LSFM data in a spin-off project of TP B07. Chapter 4 provides a detailed overview of the contribution of this thesis to the LSFM project. The methods presented within this thesis contribute to the quantitative analysis of the LSFM imaging data as a basis for understanding new models of megakaryopoiesis.

Previous research within the Rudolf-Virchow Center (RVC) (University of Wuerzburg) and the Department of Experimental Biomedicine (University Hospital, University of Wuerzburg) demonstrated the applicability of 2P-IVM for *in vivo* imaging of megakaryocytes and vessel structures in murine bone (Bender, Stritt et al. 2014). Within this previous work it was shown that megakaryocyte-specific Profilin-1 deficiency alters microtubule stability and causes a Wiscott-Aldrich-syndrome-like (WAS) platelet defect consisting of thrombocytopenia and premature platelet release (Bender, Stritt et al. 2014). Developed protocols for image analysis of LSFM data contribute to follow up on this WAS-project (Bender, Stritt et al. 2014) and aim at deepening the understanding of megakaryopoiesis within murine BM on a larger scale

2.1. Clinical implications of this research

Despite WAS being a rare genetic disorder, numerous patients suffer from defects in thrombopoiesis and the clinical implications such as thrombocytopenia or bleeding tendency. Platelet dysfunction affects morbidity as well as mortality of patients in various disciplines. In general terms, thrombocytopenia is described as reduced number of platelets within the bloodstream (<150.000/µl). Bleeding diathesis is however usually not observed at platelet levels above 30.000/µl. Platelet levels below

30.000/µl may result in petechial bleeding, bleeding upon vessel injury as well as spontaneous bleedings of mucosal tissue.

Thrombocytopenia is the most abundant cause of hemorrhagic diathesis within clinical practice (Herold 2014). It may be caused by i) defective BM, ii) increased peripheral platelet turnover or iii) combined platelet-formation and depletion defects (Herold 2014). Defective BM may result from congenital disorders (such as WAS) or acquired disorders (e.g. effect of cytostatic or immunosuppressive drugs or a underlying hematological disease) affecting thrombopoiesis or MK maturation (Pschyrembel 2007, Herold 2014). Increased peripheral platelet turnover may stem from reduced platelet lifetime due to autoantibodies (e.g. Morbus Werlhoff), increased intravascular coagulation or mechanic damages (Pschyrembel 2007). A failure of distribution of platelets may further result from an enlarged pool of thrombocytes residing within the spleen in the situation of splenomegaly (Pschyrembel 2007). Thrombocytopathy generally describes any alteration of the individual thrombocytes. More specifically it describes the situation of increased bleeding tendency due to an alteration of platelet function not being caused by a reduced number of platelets themselves. Platelet dysfunction is similarly observed in hereditarily (e.g. Morbus Glanzmann-Naegeli) and acquired conditions (chronic renal failure or macroglobulinemia) (Pschyrembel 2007, Herold 2014). Even commonly used drugs such as salicylic acid may cause thrombocytopathy in clinical practice.

In order to reduce the risk of bleeding, in the United States over 1,3 Million transfusions of platelet doses were transfused within American Association of Blood Banks (AABB) institutions in 2013 with an average cost of $571,62 per unit of apheresis platelet transfusion (Whitaker, Rajbhandary et al. 2016). Unfortunately, the rate of complications associated with platelet transfusions is high. It is estimated that at least 30% of the transfusions are associated with at least one complication (Kruskall 1997, Kaushansky 2008). Platelets only account for a fraction of the corpuscular blood components whereas platelet transfusions account for more than 25% of reported adverse events recorded in the French hemovigilance system (Garraud, Cognasse et al. 2016). Adverse reactions manifest as anaphylactic febrile reactions, bacterial contamination, transfusion related acute pulmonary injury or graft-versus-host reactions (Kaushansky 2008, Kiefel 2008). Furthermore, the apheresis procedure for obtaining donor platelets is intricate. Platelet concentrates need to be stored in special platelet storage cabinets at a temperature of 22° (+/- 2°) Celsius and can only be transfused within four days after the donation aggravating provision of platelet concentrates needed in clinical practice (Böck 2015).

A deeper understanding of the process of thrombopoiesis may thus offer new therapeutic strategies for conditions related to thrombocytopathy as well as thrombocytopenia. It may help to reduce necessary platelet transfusions or treatments with Thrombopoietin (TPO) and facilitate the development of more targeted therapies for patients suffering from platelet disorders. Furthermore, insights of MK maturation and platelet formation processes may contribute to clinical implications for stroke patients. A deeper understanding of megakaryopoiesis and platelet formation supports the research of cell-cell interactions within TP B07 in respect of precursor cells and the platelet lifecycle.

2.2. Goals of this thesis

The overall goal of this thesis is to provide useful reconstruction and analysis pipelines to gain three-dimensional information of cell-vessel interactions in the murine bone marrow. The spatiotemporal analysis of intact bone samples as performed here should lead to a deeper understanding of megakaryopoiesis and thrombopoiesis. Even if essential elements of megakaryopoiesis have been identified (Junt, Schulze et al. 2007), the mechanism of platelet formation is still poorly understood. From visualization of thrombopoiesis within murine BM using 2P-IVM it can be concluded that megakaryocytes show extremely high morphological individualities (Junt, Schulze et al. 2007, Bender, Stritt et al. 2014) whereas they display considerably low mobility within the BM (Junt, Schulze et al. 2007). These studies underline the complexity of the platelet formation process and megakaryopoiesis within the limited field of view in 2P-IVM.

Here, LSFM can help to overcome these limitations. However, LSFM imaging also creates new challenges. The main goal of my research project was to work towards a comprehensive analysis of LSFM imaging data of intact murine bone. Along recent developments in image processing and analysis techniques, this thesis aims at identification of an image analysis workflow and adapting the latter to the challenges of bone imaging such as incomplete cell staining and others as presented in chapter 6. I aimed for providing a versatile tool that, in combination with complementary techniques, brings bone imaging to the next level.

3. Literature review – Where do we stand?

Interestingly, basic principles in biomedicine as well as microscopy were introduced already more than a century ago. WRIGHT (1906) investigated the origin of platelets and first described megakaryopoiesis as a result of proplatelet formation (Wright 1906). The author later provided an overview on theories about MK formation prior to his publication in 1906 including platelets i) being fragments of leukocytes, ii) originating from extruded nuclei of red blood cells, iii) originating from red blood cell components other than the nucleus, iv) being independent blood cells, v) consisting of albuminous precipitates and vi) being the precursor cells of red blood cells (Wright 1910). Shortly before, SIEDENTOPF AND ZSIGMONDY (1903) presented their idea of a microscope using a slit aperture to illuminate the specimen (Siedentopf and Zsigmondy 1903). Thus, fortunately we already have ideas at hand, with main breakthroughs have been made only recently thanks to advances in biomedicine, imaging technology and computer science. The remainder of this chapter serves as an overview on recent developments.

3.1. Platelets and megakaryocytes

Platelets are the second most common cell type within the blood (Guo, Wang et al. 2015) and decisively contribute to processes such as hemostasis and thrombosis. Due to their short lifespan of only about ten days, anucleate platelets are continuously replenished from megakaryocytes (MKs) within the bone marrow and are removed from circulation by macrophages in spleen and liver at the end of their lifespan (Lüllmann-Rauch 2012).

3.1.1. Purpose and origin of platelets

In case an injury of a blood vessel occurs, platelets provide the essential cellular reaction of an organism to stop the bleeding by activation of a mechanical coagulation pathway (Periayah, Halim et al. 2017). In a first step, the leakage is reduced by quickly aggregating platelets within the process of *primary hemostasis* (Lüllmann-Rauch 2012). Within primary hemostasis, platelets form a clot of aggregated cells temporarily reducing the bleeding (Lüllmann-Rauch 2012). Collagen in the extracellular matrix of the blood vessels leads to the adhesion of platelets via membrane receptor glycoprotein Ib (GP Ib) (Lüllmann-Rauch 2012). GPIb binds to collagen directly or using von-Willebrand-Faktor as a mediator (Behrends, Bischofberger et al. 2012, Lüllmann-Rauch 2012). After adhesion, platelets are activated leading to conformational changes and the secretion of the content of their granule (Behrends, Bischofberger et al. 2012, Lüllmann-Rauch 2012). The conformational changes within the platelets are followed by expression of glycoprotein IIb/IIIa on the outer membrane increasing the adhesion of additional platelets from the bloodstream (Behrends, Bischofberger et al. 2012). Furthermore, activated platelets perform a change of their flat discus like structure forming pseudopodia to the surroundings (Behrends, Bischofberger et al. 2012). At the end of this process, the newly formed clot of platelets stops the bleeding temporarily.

Final closure of blood vessel injury is reached in secondary hemostasis (Behrends, Bischofberger et al. 2012). Here, a cascade of soluble coagulation factors results in permanent closure of the tissue using fibrin as stabilizing factor (Behrends, Bischofberger et al. 2012). Besides processes such as hemostasis and wound healing, platelets are essential for angiogenesis, inflammation, innate immunity (Machlus and Italiano 2013) and tumor metastasis (Chang, Bluteau et al. 2007).

3.1.2. Thrombopoiesis – Origin of megakaryocytes

Already in 1906, James Homer Wright made observations that platelets are a distinguished cell type originating from specific progenitor cells called megakaryocytes. The author observed the similarity of granule within the small anucleate platelets and the MKs found in blood producing organs (Wright 1906, Wright 1910).

Megakaryocytes constitute a cell type that is highly specialized in the formation of blood platelets as well as maintaining appropriate levels of platelets in the bloodstream (Machlus, Thon et al. 2014). Platelet formation approximately takes eight days from the stadium progenitor cells are recognized morphologically for the first time (Lüllmann-Rauch 2012) until they are released from terminally differentiated MKs (Tozawa, Ono-Uruga et al. 2014). Such as other hematopoietic cells, MKs originate from multipotent hematopoietic stem cells (HSC) (Tozawa, Ono-Uruga et al. 2014). These cells are capable of self-renewal and can be primarily found in the bone marrow (Machlus, Thon et al. 2014). During their development, HSCs follow a stepwise approach in committing for a specific cell type. They sequentially lose the ability of self-renewal and in later stages their multipotency. The loss of multipotency leads to monopotent progenitors committed to a specific cell line such as MK progenitors (Chang, Bluteau et al. 2007). Mitotic activity of the HSCs is low (Lüllmann-Rauch 2012). Cell amplification mainly occurs on the level of progenitor cells (Chang, Bluteau et al. 2007, Lüllmann-Rauch 2012). During fetogenesis, proliferation of HSCs primarily takes place in the fetal liver whereas after migration to the bone marrow, the HSCs turn into a quiescent condition to prevent exhaustion (Bluteau, Langlois et al. 2013).

3.1.3. Thrombopoietin – Driver of megakaryocyte maturation

The hematopoietic growth factor thrombopoietin (TPO) is a major cytokine triggering platelet production and HSC proliferation via its receptor c-MPL (Machlus, Thon et al. 2014). It supports self-renewal of HSCs and induces transcription factors leading to the expression of proteins like CD41 or CD42 that commit HSCs to the platelet lineage (Patel, Hartwig et al. 2005, Grozovsky, Giannini et al. 2015). These designated MKs then increase significantly in size and become polyploid (Machlus and Italiano 2013). They accumulate platelet specific granule, increase content of cytoskeletal proteins and progressively develop an invaginated membrane system (Machlus and Italiano 2013). Production of platelets and maturation of megakaryocytes is a complex process that requires the interplay of hematopoietic cytokines as well as the microenvironment within the bone marrow. Despite TPO being a primary factor for regulation of megakaryopoiesis, it was shown that absence of this protein or its receptor in TPO- or c-MPL deficient mice may still result in a successful platelet production (Ito, Ishida et al. 1996, Machlus and Italiano 2013). TPO is thus thought to act as a major factor for the development of large and mature MKs whereas this factor seems to be less important in final stages of platelet development (Kaushansky and Drachman 2002).

Plasma concentration of TPO was thought to be regulated within an “autoregulatory loop” based on platelets binding TPO with their c-MPL receptors and thus removing TPO from the circulation (Machlus, Thon et al. 2014). In this context, falling platelet levels would offer fewer c-MPL binding possibilities for TPO resulting in increased plasma concentration of TPO. In a recent study, GROZOWSKY ET AL. (2015) identify a feedback mechanism involving hepatocytes in a sensing mechanism for hepatic TPO production. The authors suggest that aging platelets loose sialic acid from their surface triggering removal of the platelets from circulation by hepatocytes. They show that the removal of platelets stimulates TPO production via JAK2 and STAT3 pathways. (Grozovsky, Begonja et al. 2015, Kile 2015) It can thus be noted that regulation of TPO levels is an intricate system involving megakaryocytes, platelets as well as hepatocytes (Grozovsky, Giannini et al. 2015).

3.1.4. Maturation of megakaryocytes

During their maturation process, MKs undergo drastic changes. To provide the contents of future platelets, MKs grow considerably in size and enlarge their cytoplasm including proteins of the cytoskeleton. The increasing content of ribosomes enables the production of platelet-specific proteins (Patel, Hartwig et al. 2005). During this process, MKs grow up to a size of 100 µm (Patel, Hartwig et al. 2005, Schulze, Korpal et al. 2006) showing high variability in their diameter depending on the ploidy of the MK (Tozawa, Ono-Uruga et al. 2014). To provide the large quantities of mRNA and proteins necessary, MKs undergo an endomitotic process. In an endomitotic process MKs reach a nuclear content of up to 128 N (Machlus and Italiano 2013, Tozawa, Ono-Uruga et al. 2014) in a single multilobed nucleus (Patel, Hartwig et al. 2005, Machlus, Thon et al. 2014) with a median content of 16 N in human and murine marrow (Zimmet and Ravid 2000, Bluteau, Lordier et al. 2009). In this context, TPO appears to drive the polyploidization process (Zimmet and Ravid 2000, Patel, Hartwig et al. 2005, Machlus, Thon et al. 2014) as TPO or c-MPL deficient mice show lower ploidy (Gurney, Carver-Moore et al. 1994, Zimmet and Ravid 2000). MKs realize endomitosis by inhibiting the formation of a complete cleavage furrow and initiating its regression leading to the MK re-entering the G1 phase with a single nucleus (Geddis, Fox et al. 2007, Machlus and Italiano 2013, Tozawa, Ono-Uruga et al. 2014). It seems that endomitosis is necessary for the provision of sufficient protein levels and the development of the invaginated membrane system (IMS) (Machlus and Italiano 2013, Machlus, Thon et al. 2014), possibly facilitating a larger increase of cytoplasm volume compared to mitotic processes (Bluteau, Lordier et al. 2009).

The IMS represents an elaborated network of membranous structures which is connected to the plasma membrane of the MKs spreading through the cytoplasm (Patel, Hartwig et al. 2005, Machlus, Thon et al. 2014, Tozawa, Ono-Uruga et al. 2014). It was shown that the IMS serves as a membrane reservoir for the formation of proplatelets and that a colocalization of actin fiber assembly with the IMS can be observed (Radley and Haller 1982, Schulze, Korpal et al. 2006).

3.1.5. Platelet formation - Models of thrombopoiesis

The biogenesis of platelets is currently theorized to stem from two distinct models. In this context the *proplatelet/flow model* as well as the *platelet territory/rupture-type model* have been introduced.

Proplatelet model

Early observations of the histogenesis of blood platelets revealed that mature MKs form *"pseudopod-like processes"* from their cytoplasm projecting into the venous system penetrating the vessel wall (Wrigth 1906, Wright 1910). It was observed that nearly the complete cytoplasm of the MKs is formed into the "pseudopods" and that characteristic granules can be found in large MKs as well as in mature MKs when forming these pseudopods (Wrigth 1906, Wright 1910). Formation of pseudopods starts from a single pole on the plasma membrane of the MK resulting in long platelet sized swellings which are connected via cytoplasmic bridges (Cramer, Norol et al. 1997, Italiano, Lecine et al. 1999, Italiano 2013).

In studies, it was shown that elongation of the pseudopod-like processes depends on the elongation of microtubules driven by dynein (Tablin, Castro et al. 1990, Italiano 2013) and that the production of platelets is realized in conjunction with actin and spectrin (Italiano 2013). Cortical bundles of microtubule are abundant in proximity to the MK body and thin out at the tip of the proplatelets (Italiano 2013). Here, the microtubule bundle forms coils similar to those found in mature platelets in the bloodstream (Italiano 2013). In order to increase the number of proplatelet tips, bending and branching on the proplatelet shaft occurs creating a multitude of daughter pseudopods (Italiano 2013). Actin cytoskeleton seems to be responsible for the bending and branching as this process is inhibited by toxins blocking actin polymerization (Italiano 2013). Organelles and granules are transported along the microtubules between the MK body and the tips of the proplatelets bidirectionally driven by the motor protein Kinesin (Richardson, Shivdasani et al. 2005, Italiano 2013). The direction of organelle transport is determined by the polarity of the microtubule bundle and its alignment along the proplatelet shaft (Richardson, Shivdasani et al. 2005, Italiano 2013).

It has been shown *in vivo* that proplatelets extend into BM vasculature through sinusoidal walls and release fragments into the lumen (Junt, Schulze et al. 2007). The released fragments show properties of immature proplatelets exceeding dimensions of mature platelets (Junt, Schulze et al. 2007). These "*preplatelets*" are considerably larger in size than mature platelets and possess the ability to form barbell-shaped structures which go through a fission process before turning into individual platelets (Junt, Schulze et al. 2007, Thon, Montalvo et al. 2010, Italiano 2013). The morphological changes of the preplatelets occur within the bloodstream and seem to be driven by shear-stress within the vascular system (Junt, Schulze et al. 2007). Comparison of proplatelet counts in pre- and post-pulmonary vessels indicate that this process might particularly take place in pulmonary arterioles (Junt, Schulze et al. 2007) comprising the first capillary bed the proplatelets pass after being released from the BM (Kowata, Isogai et al. 2014). Proplatelets are released from the MK until the “naked nuclei” are left over in close proximity to the sinusoids which was previously observed in light microscopic studies with rat MKs (Behnke 1969).

Platelet territory model

Calculations using *in-vivo* fluorescent images indicate that the bulk of thrombopoiesis results from platelet shedding from perisinusoidal MKs (Junt, Schulze et al. 2007). Studies with bone marrow explants however show that another mode of platelet production can observed *in vitro*. The process of fragmentation of the MK in this environment was compared to an explosion taking several hours to complete (Albrecht 1957, Kosaki 2005). TONG ET AL. (1987) show that MKs can alter their mode of platelet release in reaction to acute thrombocytopenia. The authors observed that MKs react with the release of long and beaded proplatelets into the venous system prior to an increase of MK size, ploidy or number (Tong, Seth et al. 1987). Similar observations were made in other studies (Handagama, Feldman et al. 1987, Radley and Hartshorn 1987) which are reviewed in KOSAKI (2005) and support the theory that fragmentation of MK cytoplasm constitutes another mode of platelet production (Kosaki 2005). This model was termed “*platelet territory model*” as it suggests that the demarcation membrane system (DMS) – later called IMS - results from invagination of the plasma membrane of MKs in order to form “*platelet territories*” which basically rupture within the BM releasing platelets (Kosaki 2005, Kowata, Isogai et al. 2014). KOWATA ET AL. (2014) similarly observed that in a situation with acute platelet need MKs increasingly release thick protrusions instead of proplatelets into the bloodstream (Kowata, Isogai et al. 2014). This indicates that MKs are able to alter their mode of platelet release depending on the urgency of platelet demand. However, these studies on the platelet territory model do not elucidate the origin of the microtubule bundle underneath the plasma membrane (Behnke 1969, Kowata, Isogai et al. 2014). The microtubule bundle constitutes a key feature of platelets and a corresponding arrangement of microtubule is not found in “platelet territories” as it is within the barbell-shaped proplatelets (Behnke 1969, Italiano 2008, Kowata, Isogai et al. 2014).

In a recent study NISHIMURA ET AL. (2015) support the theory of an alternative mode of thrombopoiesis besides the proplatelet model. The authors based their reasoning on observations made using 2P-IVM and they demonstrate that formation of proplatelets cannot explain rapid platelet turnover in acute situations such as inflammatory reactions (Nishimura, Nagasaki et al. 2015). This rapid mode of platelet release was termed "*rupture thrombopoiesis*" and it was shown that IL-1 α is a primary driver of this mode of platelet release as serum levels were elevated after acute platelet loss or in inflammatory reactions in mice (Nishimura, Nagasaki et al. 2015). It was thus suggested that chronic platelet need is met by proplatelet formation driven by TPO and that in situation with acute and rapid need of platelets IL-1 α serves as a driver for rupture-type thrombopoiesis and inhibiting proplatelet formation (Nishimura, Nagasaki et al. 2015).

3.1.6. Hematopoietic stem cell niches

As introduced above, MKs originate from hematopoietic stem cells (HSC) residing within the BM. During embryogenesis, HSCs migrate to the fetal liver and spleen until they finally reside within the BM (He, Zhang et al. 2014). Within the BM, most of the HSCs remain in a nonproliferating quiescent state in order to provide a long term supply of HSCs and consequently to prevent exhaustion of hematopoiesis and the stem cell pool (Day and Link 2014). It is theorized that maintenance of this non-proliferative state is realized by stromal cells which are localized in special microenvironments called stem cell niches (Day and Link 2014) which were first introduced by SCHOFIELD (1978) (Schofield 1978). Various stromal cell types and signaling pathways are involved in control of the survival of HSCs and their self-renewal as well as their differentiation within the specific microenvironments (He, Zhang et al. 2014). Studies indicate the influence of stromal cells such as osteoblasts (Calvi, Adams et al. 2003), endothelial cells, pericytes, reticular cells, sympathetic nerves and Schwann cells on the regulation of the stem cell niche (Day and Link 2014). KUNISAKI ET AL. (2013) show that quiescent HSCs are preferentially localized in close proximity to small arterioles in the endosteal BM supporting the theory of distinct niches within the BM (Kunisaki, Bruns et al. 2013). It is suggested to distinguish two distinct microenvironments within the BM termed osteoblastic and vascular niche (Yin and Li 2006, Yoon, Cho et al. 2012, He, Zhang et al. 2014). Among these, the osteoblastic niche provides a microenvironment favoring the quiescence of HSCs maintaining the long-term HSC pool (Yin and Li 2006, Yoon, Cho et al. 2012, He, Zhang et al. 2014).

The vascular niche on the other hand serves as a microenvironment regulating the proliferation, differentiation and mobilization of HSCs (Yin and Li 2006, Yoon, Cho et al. 2012, He, Zhang et al. 2014).

Furthermore, a correlation between the location of HSCs within the bone marrow in respect to the vessel system and thus their hypoxic profile was postulated (Parmar, Mauch et al. 2007, Eliasson and Jonsson 2010, Mohyeldin, Garzon-Muvdi et al. 2010, Nombela-Arrieta, Pivarnik et al. 2013). Using flow cytometric analyses, it was shown that the highest amount of long-term repopulating HSCs in a quiescent stage can be found in hypoxic niches distant from capillaries (Parmar, Mauch et al. 2007). NOMBELA-ARRIETA ET AL. (2013) however indicate, that a characteristic hypoxic state of HSCs is rather regulated by cell-specific mechanisms than their location in specific niches with low oxygenation (Nombela-Arrieta, Pivarnik et al. 2013).

3.1.7. Niches of megakaryocyte differentiation

The current model of thrombopoiesis similarly assumes that platelet precursors migrate from an osteoblastic towards a vascular niche in close proximity to vessel sinusoids during maturation (Avecilla, Hattori et al. 2004, Bluteau, Lordier et al. 2009, Grozovsky, Giannini et al. 2015, Malara, Abbonante et al. 2015). The concept of this model is however mainly based on qualitative and quantitative evaluation of specific progenitor cell populations localized in confined spatiotemporal niches (Stegner, vanEeuwijk et al. 2017). AVECILLA ET AL. (2004) observe the synergy of chemokines including stromal-derived factor 1 (SDF-1) and fibroblast growth factor-4 (FGF-4) with BM endothelial cells in mice deficient TPO (*Thpo*$^{-/-}$) in promoting thrombopoiesis (Avecilla, Hattori et al. 2004). The authors suggest that SDF-1 and FGF-4 ultimately enhance localization of CXC chemokine receptor type 4 *(*CXCR4) MK progenitors to the vascular niche facilitating survival, maturation and platelet release (Avecilla, Hattori et al. 2004). This was first observed by HAMADA ET AL. (1998) who report that SDF-1 drives the migration of MKs through the endothelial cells within the BM resulting in an enhanced platelet release (Hamada, Mohle et al. 1998). This theory is supported by studies investigating mice lacking SDF-1 whose phenotype exhibits substantial defects in BM hematopoiesis (Nagasawa, Hirota et al. 1996). Based on this it was theorized that the osteoblastic niche provides factors inhibiting proplatelet formation (Larson and Watson 2006). Such factors include contact to stromal cells (Larson and Watson 2006) as well as collagen I (Reddi, Gay et al. 1977, Nilsson, Debatis et al. 1998, Pallotta, Lovett et al. 2009) suppressing proplatelet formation via RhoA activation (Sabri, Jandrot-Perrus et al. 2004). As reported above, SDF-1 and FGF-4 seem to induce a migration of MKs towards the vascular niche which is comprised of factors promoting proplatelet formation (Larson and Watson 2006, Bluteau, Lordier et al. 2009). It is suggested that these factors include Von Willebrand factor, fibrinogen, laminin, vitronectin (Larson and Watson 2006) and type IV collagen (Larson and Watson 2006, Pallotta, Lovett et al. 2009). These observations support the hypothesis of microenvironments being crucial for the maturation of MKs and that a corresponding journey from the osteoblastic niche to the vascular niche might be necessary for completion of the maturation cycle (Figure 1).

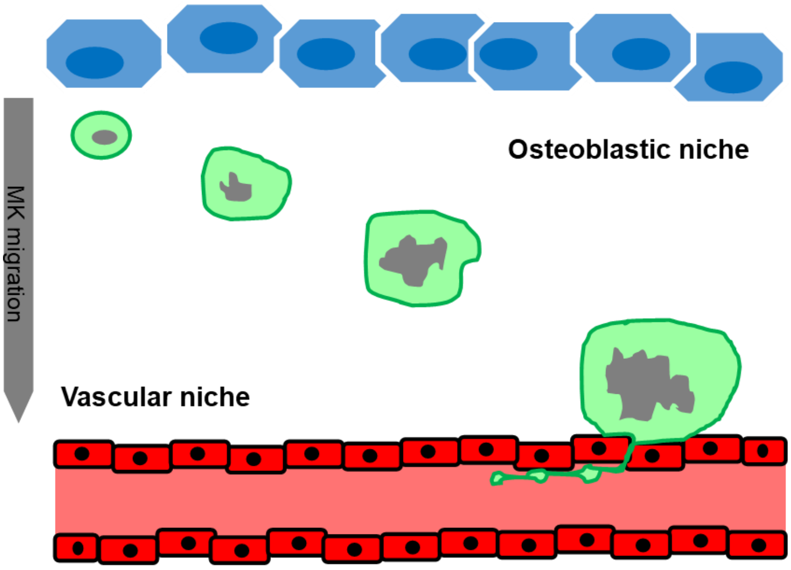

Figure 1: Current model of megakaryopoiesis: journey of MKs from the osteoblastic to the vascular niche during maturation; adapted from (Stegner, vanEeuwijk et al. 2017).

3.2. Imaging technology

This section briefly introduces basic principles of imaging technology applied in this research. This project is based on recent advances in microscopy technology as well as clearing procedures of dense tissue.

3.2.1. Light sheet fluorescence microscopy

LSFM is an imaging technology which allows optical sectioning of sample tissue enabling a high resolution three-dimensional reconstruction of the image. Three dimensional imaging of fixed samples has previously been realized by physically sectioning the samples and imaging was performed slice by slice (Huisken and Stainier 2009). In contrast to physically sectioning, optical sectioning simplifies the imaging procedure and allows for imaging of intact specimen. Previous studies demonstrate the feasibility of optical sectioning by deconvolution without the need for a specific microscope (McNally, Karpova et al. 1999, Huisken, Swoger et al. 2004). Also, laser scanning confocal microscopy (LSCM) offers an approach of optical sectioning

(Paddock 2000) whereas the imaging volume is limited by penetration depth of illuminating laser caused by light scattering (Huisken and Stainier 2009).

LSFM however follows a different approach of optical sectioning of sample tissue. The principle of LSFM was initially described by SIEDENTOPF AND ZSIGMONDY (1903). The authors introduce a microscope setup in which a light sheet is generated from incident sunlight using a slit aperture in order to observe gold particles (Siedentopf and Zsigmondy 1903). This suggested concept of illuminating a specimen from the side and obtaining the image in the perpendicular axis was not reportedly applied until VOI ET AL. (1993) used a similar imaging technique called orthogonal-plane fluorescence optical sectioning to investigate the structure of the cochlea (Voie, Burns et al. 1993) and the intact guinea pig tympanic bulla (Voie 2002). DODT ET AL. (2007) used LSFM for visualization of neuronal networks within the mouse brain (Dodt, Leischner et al. 2007).

Modern applications of LSFM use a cylindrical lens to focus the light sheet for illuminating the focal plane of the detection optics (Huisken, Swoger et al. 2004, Huisken and Stainier 2009). Illumination plane and focal plane of the detection optics are aligned accordingly and the sample specimen is placed within the focal plane of the detection optics (Huisken and Stainier 2009, Santi 2011). Images gathered from detection optics are captured onto a CCD-camera (Huisken and Stainier 2009). In order to create a three-dimensional image, the specimen is positioned along the detection axis in a stepwise fashion resulting in a corresponding stack of images which are stored and used for three-dimensional reconstruction (Huisken, Swoger et al. 2004, Dodt, Leischner et al. 2007, Huisken and Stainier 2009). LSFM has been recently applied at the RVC in Würzburg on mapping immune processes in intact murine and human tissues (Brede, Friedrich et al. 2012).

3.2.2. Methods for optical clearing of dense tissue

Specimen transparency is a prerequisite of imaging large intact structures such as brain or bone using LSFM (Dodt, Leischner et al. 2007). Light scattering substantially reduces the quality of the image and photon propagation through the specimen is hampered by interaction of photons with cellular and other structures (Ntziachristos 2010). When imaging brain tissue, differences in refractive indices constitute predominant factors in light scattering (Dodt, Leischner et al. 2007). Various clearing protocols have been suggested to minimize light scattering and to align refractive indices within the specimens.

Imaging of intact bone was realized in this project by application of a clearing protocol using benzylalcohol and benzylbenzoat (BABB) (Stegner, vanEeuwijk et al. 2017). The BABB method was initially applied for imaging of brain tissue after fixation and dehydration (Dodt, Leischner et al. 2007). This clearing method results in remarkable specimen clearing due to the high refractive index (RI) of the specimen and the clearing solution (Susaki, Tainaka et al. 2014). However, clearing with BABB causes quenching of fluorescent proteins (Becker, Jährling et al. 2012, Susaki, Tainaka et al. 2014). Based on BABB, a revised clearing protocol was introduced resulting in less quenching of fluorescent proteins by using dibenzyl ether instead of BABB (Becker, Jährling et al. 2012, Erturk, Becker et al. 2012) and tetrahydrofuran for the dehydration process (Erturk, Becker et al. 2012). HAMA ET AL. (2011) introduce a urea-based clearing protocol resulting in reduced quenching of fluorescent proteins (ScaleA/ScaleA2) (Hama, Kurokawa et al. 2011). The applicability of this method is however limited due to its tendency to cause tissue swelling as well as required long treatment times (Susaki, Tainaka et al. 2014). KE ET AL. (2013) propose a fructose- and thioglycerol-based clearing method called *SeeDB* (Ke, Fujimoto et al. 2013) resulting in a relatively fast protocol preserving detailed structures and fluorescent signals (Susaki, Tainaka et al. 2014). Unfortunately resulting transparency of the specimen remains insufficient for LSFM (Susaki, Tainaka et al. 2014). CHUNG ET AL (2013) reported a clearing method termed CLARITY leading to highly transparent tissue (Chung and Deisseroth 2013). However, electrophoresis is needed for the clarification process and clearing of larger specimens becomes increasingly difficult (Susaki, Tainaka et al. 2014). Resulting from the experience with existing clearing protocols, SUSAKI ET AL. (2014) suggest a revised reagent termed CUBIC as a result of extensive screening of chemical properties based on chemical components of ScaleA2 consisting of i) polyhydric alcohols (glycerol), ii) detergents (Triton-X) and iii) urea-like chemicals (Hama, Kurokawa et al. 2011, Susaki, Tainaka et al. 2014). The authors demonstrate the applicability of the CUBIC protocol to imaging of fluorescent proteins, large volume samples, immunostained samples and specimen with nuclear counterstaining (Susaki, Tainaka et al. 2014, Susaki, Tainaka et al. 2015). Figure 2 provides an overview of existing clearing protocols introduced above and summarizes advantages and shortcomings of each method.

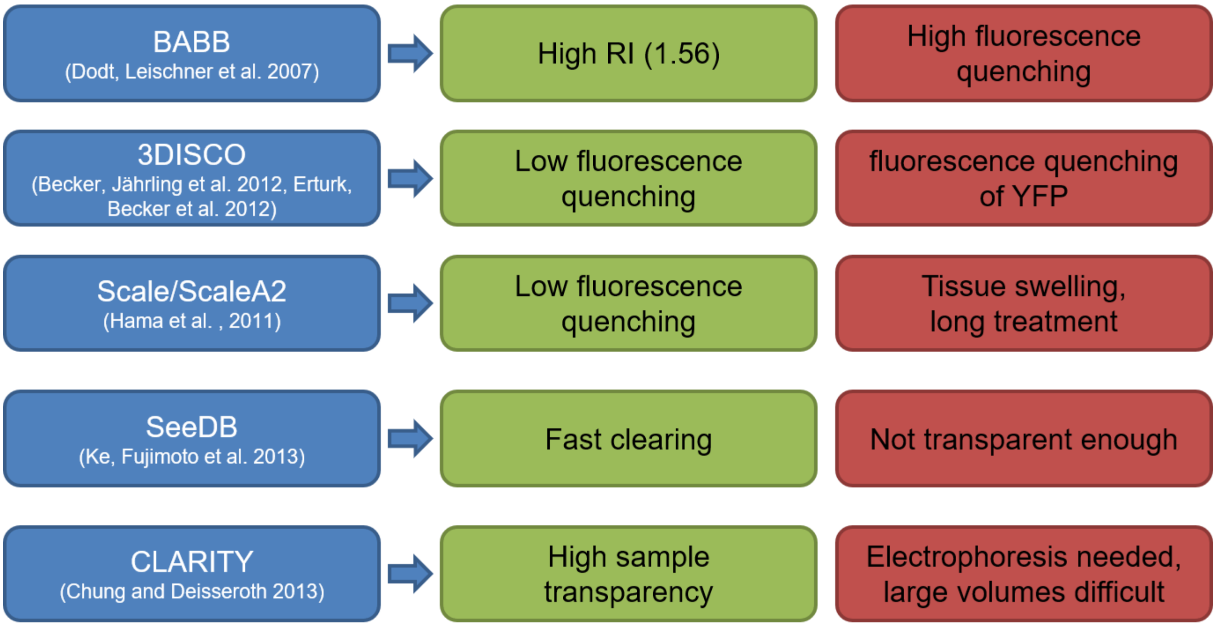

BABB (Dodt, Leischner et al. 2007)	High RI (1.56)	High fluorescence quenching
3DISCO (Becker, Jährling et al. 2012, Erturk, Becker et al. 2012)	Low fluorescence quenching	fluorescence quenching of YFP
Scale/ScaleA2 (Hama et al. , 2011)	Low fluorescence quenching	Tissue swelling, long treatment
SeeDB (Ke, Fujimoto et al. 2013)	Fast clearing	Not transparent enough
CLARITY (Chung and Deisseroth 2013)	High sample transparency	Electrophoresis needed, large volumes difficult

Figure 2: Comparison of clearing protocols.

3.3. Developments in image processing and image analysis

Microscopy technologies such as LSFM offer new applications for scientists of various fields. Data and digital image stacks arising from these technologies however require diligent processing and analysis. In this context new fields such as computer vision emerge enlarging the circle of specialties involved in research projects in biology, medicine or various other fields.

3.3.1. Challenges arising from computational imaging and biology

With new imaging techniques in fluorescence and multidimensional imaging available, new challenges arise for researchers in dealing with the increasingly larger volumes of image data (Dorn, Danuser et al. 2008). In light of these developments it has been recognized that management and analysis of the datasets lag behind (Swedlow, Goldberg et al. 2003, Swedlow, Goldberg et al. 2009) whereas reliability and efficiency of image processing for studies in cell biology is increasingly important (Dorn, Danuser et al. 2008). Similar to the field of neuroscience or medicine, in biomedical imaging researchers are increasingly faced with bioinformatics when dealing with handling of data (Langer 2011, Hornick and Hinchcliffe 2015) and transforming it into quantitative information or statistic evaluation (Dorn, Danuser et al. 2008). Image analysis is however subject to limitations within the sequential process of storing, processing and analyzing large datasets (Swedlow, Goldberg et al. 2003). Major challenges arise from i) generation of massive amounts of imaging data by high-throughput imaging, ii) visualization of these massive datasets and iii) quantitative analysis, statistical evaluation and mathematical simulation of non-standardized datasets (Walter, Shattuck et al. 2010).

Self-evaluation of biologists and computer-scientists indicates potential benefit from cooperation, as the self-evaluated skillset seems to complement each other in the fields of Image analysis, Programming and Biology (Cardona and Tomancak 2012). It is recognized that it requires specific expertise for selection of algorithms applicable and setting of control-parameters (Dorn, Danuser et al. 2008). At the intersection of biology and microscopy, challenges arise in bioimage informatics accessing and analyzing data as image generation often exceeds processing capability (Peng, Zhou et al. 2016). Researchers face first obstacles when defining appropriate measurements for image analysis and choosing the software tool to analyze the data (Dorn, Danuser et al. 2008). Additionally, complexity of multidimensional images challenge computational methods, as information such as time or various color channels are embedded within the dataset (Walter, Shattuck et al. 2010, Peng, Zhou et al. 2016). A fully automated cell-detection algorithm has been realized for detection of mainly ellipsoid HSCs in bright-field microscopy (Buggenthin, Marr et al. 2013) or surfaces of embryos in 3-D (Bootsma and Brodland 2005). Until now, human-machine interaction is however often necessary for image analysis to realize a complete understanding of image contents (Dorn, Danuser et al. 2008). The human eye has a particular strength in object recognition and thus helps to account for inhomogeneities within the images improving the effectiveness of computational algorithms (Dorn, Danuser et al. 2008).

Data stemming from the microscope represent raster-based computer files. In contrasts to vector-based image files, the former consist of a grid of pixels containing intensity information (Hornick and Hinchcliffe 2015). For storage of these original data, a multitude of file formats are available such as TIFF, JPEG/, RAW/DNG as well as proprietary file formats (Swedlow, Goldberg et al. 2009, Hornick and Hinchcliffe 2015). For generation of primary data from the microscope, uncompressed file formats such as TIFF or RAW need to be selected containing the necessary information for analysis (Hornick and Hinchcliffe 2015). For data presentation in later stages these data can be transformed into compressed file formats such as joint photographic experts group

(JPEG) or portable network graphics (PNG) (Hornick and Hinchcliffe 2015). After compression, files can however not be transformed into uncompressed formats.

The data volume of bioimages are often in the scale of several gigabytes per dataset (Scholl, Aach et al. 2010). In brain imaging, datasets easily reach the size of terabytes of raw data per brain (Peng, Zhou et al. 2016, Landhuis 2017). For access to these large multidimensional datasets, efficient data structures are necessary for simply accessing and evaluating the datasets after capturing. Hardware requirements for accessing these datasets often exceed the available computing power so that downsampling of the Voxel-data becomes necessary to realize fast browsing through the samples (Peng, Zhou et al. 2016). Data structures such as Octree organizing data into hierarchical levels to increase efficiency in data access and computational processing represent potential solutions in reducing hardware requirements (Peng, Zhou et al. 2016, Lucas, Rodrigues et al. 2017). Besides simple storage and access of these significant amounts of data, management of numerous datasets associated with various experiments within a single imaging project turn into critical requirements (Swedlow, Goldberg et al. 2009, Landhuis 2017). For saving of these datasets and to overcome challenges resulting from a multitude of proprietary file formats, open-source tools as part of the Open Microscopy Environment (OME) may support the handling and analysis of large imaging data (Moore, Allan et al. 2008).

Despite these challenges arising from of the use of computational techniques in quantitative biology, *efficiency, consistency and completeness* of computational imaging projects justify the efforts and promote advances in the field (Dorn, Danuser et al. 2008). Similarly to the design of wet-lab experiments, imaging and data processing techniques with strengths and limitations need to be accounted for when designing experiments (Dorn, Danuser et al. 2008).

3.3.2. Typical image analysis workflow

Detection of features within images and quantification of numeric parameters which can be exported for further analysis represent the major objectives of image processing (Dorn, Danuser et al. 2008). An image analysis workflow begins after image acquisition and makes use of the raw data presented in the specific file formats.

Preprocessing

Within a first preprocessing step, basic image processing techniques such as application of filters are typically applied to improve the signal-to-noise ratio and for selective enhancement of specific image features (Eils and Athale 2003, Dorn, Danuser et al. 2008). Low-Pass filters such as a Gaussian filter reduce imaging noise at the cost of image details (Dorn, Danuser et al. 2008). Other filters such as edge-filters (Canny 1986) or line-filters (Koller, Gerig et al. 1995) can be applied for enhancing edges or lines (Dorn, Danuser et al. 2008).

Visualization via volume rendering

For a simple display of imaging data, volume rendering offers a visualization method for transformation of 2D-stacks into three-dimensional images (Chen, Swedlow et al. 1995, Eils and Athale 2003). Within a first step, individual voxel in the 3-D volume are assigned a specific level of opacity, contrast and color (Chen, Swedlow et al. 1995, Eils and Athale 2003). Shading of the individual voxel is consequently calculated from the position of the light source and the position of the observer (Chen, Swedlow et al. 1995, Eils and Athale 2003). A projection of the image is realized by computing single voxel colors based on a ray casting through each grid point on the projection plane when continuously updating the current color based on a transparency formula (Chen, Swedlow et al. 1995, Eils and Athale 2003). Once this ray is reaching a new sample volume for calculation of the new voxel color, it is taking into account the color value of the previous position as well as interpolated color and opacity values (Chen, Swedlow et al. 1995). The ray only transfers a sample position unaltered, if the opacity is close to zero (Chen, Swedlow et al. 1995). This volume rendering provides a good visualization of three-dimensional structures whereas extraction of quantitative data is not possible (Eils and Athale 2003).

Data extraction using surface rendering

Data can be extracted from objects created with a surface-rendering-technique (Eils and Athale 2003) also known as 3D graphics (Chen, Swedlow et al. 1995). In these techniques, objects are represented by polygons (Lorensen and Cline 1987, Cline, Lorensen et al. 1988, Chen, Swedlow et al. 1995, Eils and Athale 2003), triangular structures (Bootsma and Brodland 2005) or Voroni diagrams (Klauschen, Qi et al. 2009). Most commonly the marching cube algorithm is used based on polygonal structures (Eils and Athale 2003) initially presented by CLINE ET AL. (1988) (Cline, Lorensen et al. 1988). A threshold value needs to be set for the dataset as a whole for the construction of an isosurface (Eils and Athale 2003). Based on this, the algorithm evaluates whether each individual neighboring voxel belongs to a specific surface object (Cline, Lorensen et al. 1988). A shaded image is created by calculation of polygons interpolating the voxel edges (Cline, Lorensen et al. 1988). Based on the objects created with surface rendering, quantitative image analysis and statistical evaluation can be performed (Eils and Athale 2003).

4. Positioning of this thesis

As discussed in the previous chapter, current models of thrombopoiesis hypothesize the existence of spatiotemporal niches within the BM during the maturation cycle of HSCs as well as MKs. Based on data from 2P-IVM studies, JUNT ET AL. (2007) however report that MKs only perform low migratory movements are primarily found in close proximity to vessel structures (Junt, Schulze et al. 2007). Unfortunately, the field of view in 2P-IVM is limited and the fluorescent labelling of the CD41-YFP reporter mice used was confined to a third of the MKs (Junt, Schulze et al. 2007, Zhang, Varas et al. 2007, Stegner, vanEeuwijk et al. 2017). Thus, only a relatively small number of MKs could be assessed. The data presented however contradict the model of a directed migration of the MKs during their maturation cycle (Stegner, vanEeuwijk et al. 2017). NOMBELA-ARRIETA ET AL. (2013) present similar evidence for the distribution of HSCs within the BM as their location was found to be predominantly perivascular (Nombela-Arrieta, Pivarnik et al. 2013). This discrepancy between the current model of megakaryopoiesis and the data presented in the latter studies has been recently assessed by ACAR ET AL. (2015) who present evidence from deep confocal imaging of optically cleared bone marrow (Acar, Kocherlakota et al. 2015). Results indicate that most of the HSCs (in this study approximately 85%) are located within 10 µm distance from vessels and the sinusoids leading to the hypothesis that HSCs are primarily located in the perisinusoidal niches (Acar, Kocherlakota et al. 2015).

4.1. Major research questions

Based on the previous work within the research group at Rudolf Virchow Center in Würzburg, the work within this thesis is sought to contribute development of image reconstruction and analysis pipelines to the MK-project within CRC 688. Ultimately this thesis aims at elucidating the following research questions:

i) How does the **amount** of MKs change during megakaryopoiesis?
ii) How does the **volume** of MKs and the **MK density** change during megakaryopoiesis?
iii) How does the **position** of MKs in relation to vessel structures change during megakaryopoiesis?

The analysis of the spatiotemporal pattern of MKs requires a stepwise approach encompassing information about the position, volume and thus the density of MKs in a specific BM region.

4.2. Point of departure

Recent developments in optical clearing, imaging technology and data processing techniques allow an analysis of MKs within the BM in a larger scale. Visualization of megakaryopoiesis is often tedious and usually requires bone sectioning (Patel, Hartwig et al. 2005). Techniques as Light Sheet Fluorescence Microscopy (LSFM) offer large volume imaging without cutting effort and artefacts. Within this project, our research group developed an approach allowing the analysis of sections within intact murine sternum as well as femur bone (Stegner, vanEeuwijk et al. 2017). Unlike other specimen such as soft tissue, imaging of firm structures such as bone are accompanied by inherent challenges resulting from the material properties. Imaging of intact bone requires a uniform optical clearing even though bone is inherently inhomogeneous in consistency as well as density. Bone structures are a result of a dynamic equilibrium between bone loss and bone building orchestrated by osteoblasts and osteoclasts. This results in vast differences in bone density across one piece of bone depending on the local strain situation. This is reflected in an irregular calcium intercalation within the bone aggravating optical clearing. Local inhomogeneity of the bone marrow is accompanied by irregular light penetration of the bone as well as irregular staining of the specimen. Imaging of intact bone furthermore requires careful preparation of the specimen so that surrounding tissue such as muscle is completely removed without affecting the intact bone structure as well as the specimen staining.

4.3. Positioning within the research team

As introduced in Chapter 2, this project is embedded in CRC 688. It consists of main task groups as depicted in Figure 3 collaborating on the realization of the project considering specific features of the project to investigate the research question. Previous work within the research group around *Prof. Beilhack* at the University Hospital in Würzburg provided substantial input in terms of sample preparation and optical clearing of dense tissue (Brede, Friedrich et al. 2012). Based on this experience, collaboration partners from the research groups around *Prof. Nieswandt* and *Dr. Stegner* at the Rudolf Virchow Centre in Würzburg developed sample preparation and staining procedures laying the foundation for imaging of intact bone.

This thesis was mainly performed within the research group around *Prof. Heinze* and deals with image analysis as highlighted in Figure 3. The microscope used for data capture is a custom-built light sheet fluorescence microscope constructed by engineers and physicists from the research group around *Prof. Heinze* at the Rudolf-Virchow Centre in Würzburg. They provided further insights to the optical engineering necessary for the construction and optimization of the microscope for intact bone imaging and supervised my thesis.

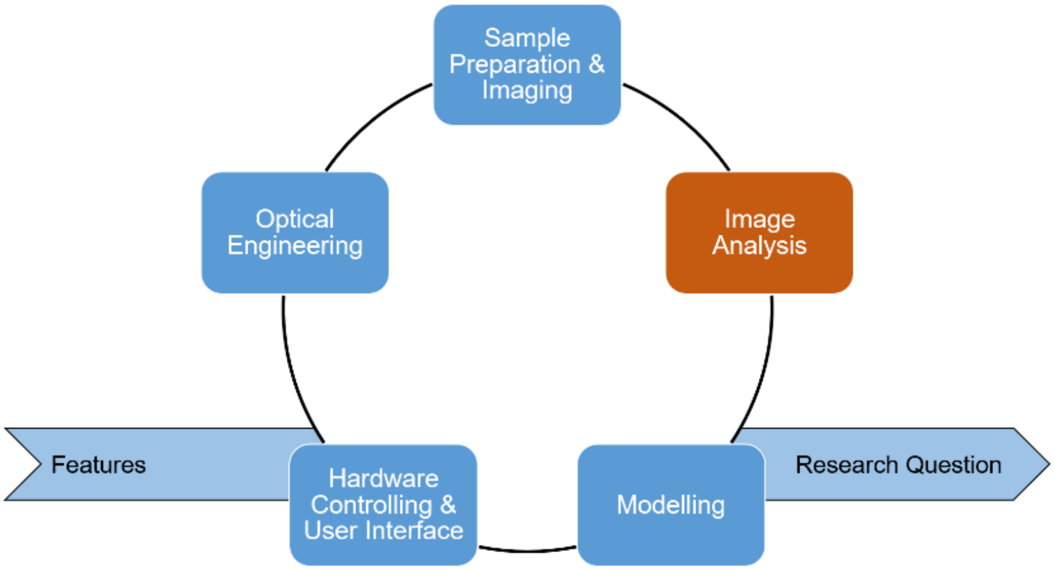

Figure 3: Task groups of TP B07; field of this thesis highlighted in orange.

Division of tasks in image analysis

Image Processing and Segmentation was performed in close collaboration with Oguzhan Angay (AG Heinze). At the time of the beginning of this thesis project, work within TP B07 had already started. This thesis work was sought to provide additional input to the image analysis team at the Heinze research group from a medical as well as engineering standpoint.

Tasks of Image analysis primarily consisted of i) promoting the development of image analysis protocols of Tiff-stacks provided to optimize MK recognition ii) feedback from an image analysis standpoint to collaborators for optimization of hardware as well as sample preparation and iii) provision of working power for the semi-automated processing of the analytical work at hand. Table 1 provides an overview on the division of tasks within the MK project whereas an emphasis is put on the depiction of input from Oguzhan Angay (OA) as well as input from this thesis (PS) during the development of the image analysis protocol (i.). Accounting of individual process-steps in part C to an individual person collaborating serves as an indicator of the person contributing most, whereas each of the processing steps were developed in close collaboration. Major input of work within this thesis is highlighted. Statistical results and images presented originate from the close collaboration within the research team at the RVC.

Experimental prerequisites

Experimental prerequisites are outlined in detail in STEGNER ET AL. (2017) (Stegner, vanEeuwijk et al. 2017). Data was acquired using a home-built LSFM-setup similar to those reported previously (Keller and Stelzer 2008) with three detection channels (MK channel, vessel channel, autofluorescence channel) with laser lines in the red spectrum (642 nm and 730 nm). Immunostaining of the vascular structure was realized by anti-CD105 (anti-Endoglin) antibody (BioLegend, San Diego, CA, USA; 0,4 µg/g body weight) or tetramethylrhodamine dextran (2 MDa; Life Technologies, Darmstadt, Germany) in conjunction with Alexa 647 protein labelling kits (Alexa Flour 647, Life Technologies, Darmstadt, Germany) (Stegner, vanEeuwijk et al. 2017). The MKs were immunostained using an anti-GPIX (CD 42a) antibody (0,6 µg/g body weight) in conjunction with Alexa Fluor 750 (Alexa Flour 750, Life Technologies, Darmstadt, Germany) (Stegner, vanEeuwijk et al. 2017).

Overview of collaborators responsible for development of individual project steps with focus on Image analysis			
Project Part	**Working Step**	**Realization**	**Supervision**
A. Sample Preparation	Provision of wilt-type and knock-out mice	BN	
	Provision of home-made antibodies	BN	
	Induced Thrombocytopenia	JE	BN
	In vivo Immunostaining	JE	BN
	Perfusion & Fixation	JE	BN
	Dehydration and Clearing	JE	BN
B. Imaging	Design of LSFM setup	MF, JP, KH	KH
	Imaging of the specimens	JE	KH
C. Image Processing and Segmentation	Transfer of Input Data to 3D stack	OA, **PS**	KH
	Median Filter 2pixel	**PS**	KH
	Removal of Speckles	**PS**	KH
	Crosstalk-Removal	OA	KH
	3D-Gauss (32 bit)	OA	KH
	Unsharp mask	OA	KH
	Median Filter 2pixel	OA	KH
	Baseline Subtraction (after Gauss)	**PS**	KH
	Background Subtraction	**PS**	KH
	Creation of binary image and filling holes	OA, **PS**	KH
	Image calculation to create core channel	**PS**	KH
	Particle Remover	**PS**	KH
	MK core Iso-Surface and MK filling	OA	KH
	Removal of antibody-agglomerates (Iso)	OA	KH
	Vessel segmentation (Cell)	OA, **PS**	KH
	Distance transformation	OA	KH
	Vessel Filling	OA	KH
	Marrow generation	OA, **PS**	KH
	Separate Segmentation of MK20/MK10	OA, **PS**	KH
	Segmentation of MK20/MK10 (Cell)	OA, **PS**	KH
	Spots	OA	KH
D. Statistics and Modelling	Statistics of output Excel-files	DS	
	Modeling	MG / KH	KH

Table 1: Overview of collaborators MK project: Prof. Dr. Bernhard Nieswandt (BN), Prof. Dr. Katrin Heinze (KH), Dr. David Stegner (DS), Dr. Judith vanEeuwijk (JE), Oğuzhan Angay (OA), Maximilian Gorelashvil (MG), Jürgen Pinnecker (JP), Mike Friedrich (MF) Patrick Schmithausen (PS).

4.4. Detailed contributions of this thesis to the results of the overall research project

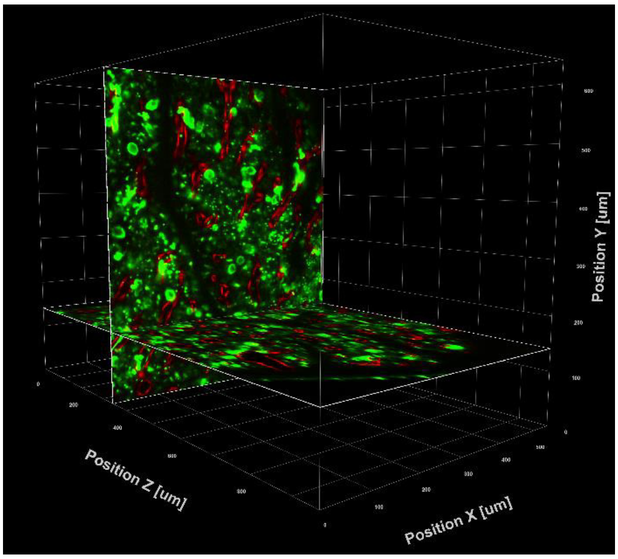

Figure 4: Representation of the three-dimensional maximum intensity projection in x/y- and x/z-planes: Vessel (red), MK (green); grid: 100µm.

Section 4.3 outlines how this thesis is embedded in the MK project within CRC 688. In the following section it is pointed out in detail, how independent contributions of this thesis are part of the results from this complex research project. Work within this thesis primarily contributed to the development of an image analysis protocol and subsequent image analysis. The image analysis protocol was tailored to specific challenges when imaging MKs and vessel structures in intact murine bone as presented in the following section 6. To my best knowledge, a comparable image analysis protocol dealing with intact bone imaging had not been introduced before at the time of this research project. Tutorials and manuals served as literature background and provided theoretical insights to image analysis and software handling. Parameters chosen for the analysis workflow were critically determined in an empirical fashion whereas the sequence of the individual steps was defined by the characteristics of this project. During the development phase of the image analysis protocol, a multitude of reasonable protocols were tested and evaluated. Results were continuously compared with the original data to verify effects of a change of parameters, setting of a specific threshold or a change of the sequence of individual steps. Using clipping planes in Imaris® (such as Figure 4), the entire image stacks were evaluated for the effect of every change within the analysis protocol. Implications from image analysis were discussed with project collaborators dealing with probe development, imaging as well as microscope development for an optimization of imaging conditions (Figure 3).

A major shortcoming of a semi-automated image analysis protocol stems from missing objectivity and generalizability of crucial steps. Setting of parameters such as intensity thresholds is inherently biased. Despite a direct visual feedback in a two- or three-dimensional preview, parameters are set based on a choice of the spectator as result from individual perception. For reduction of this bias, steps were performed individually by OA and PS during development of the image analysis protocol. This allowed for a comparison of the effect of each change to identify possible bias. Changes of the analysis protocol were adopted if results from OA and PS were comparable. This thesis therefore also serves the purpose of bias-reduction and a control of pipeline development for subsequent image analysis. A misalignment of resulting data indicated a potential bias when results were non-reproducible. In summary my contributions provided an analysis protocol that allowed statistical evaluation of key parameters such as size, morphology, location of MK- and vessel structures.

5. Method development: From the mouse to the cell…

The following paragraphs provide a brief overview on the methods and the equipment used for image processing and analysis of the MK project as published in STEGNER ET AL. (2017).

5.1. Image analysis setup and technology

The analysis setup used for image processing and data extraction consisted of a custom-built desktop-PC setup with an Intel i7 Hexacore (3930K) @ 3,6 GHz. It was equipped with 64 GB DDR3 RAM and a 128GB SSD reserved for caching page files. Initially, a Nvidia GeForce Titan (1. Gen) with 6 GB GDDR5 graphics memory was used for graphics display and image processing. During the course of analysis, the system was upgraded to an AMD Radeon Sapphire Vapor-X R9 290X Graphics module with 8 GB GDDR5 graphics memory. The stacks were evaluated using a 27-inch Fujitsu Siemens monitor with a resolution of 2560 x 1440 Pixel. The analysis was later performed additionally on a second system with dual Intel Xeon CPU (E5-2643 v3, 6 cores with hyperthreading), 512 GB DDR4 RAM and a Sapphire AMD FirePro W9100 16GB GDDR5.

Data from LSFM was saved as multicolor tagged image file format (TIFF) stacks where each of the images represent an individual x/y plane of a single color channel. Within the x/y plane, the LSFM setup was set to provide images with a resolution of 1080 x 1280 pixels. Each pixel was set to correspond to 0,5 µm in x and y direction covering an approximate area of 0,25µm^2 in the x/y plane. Stacks were generated sequentially by imaging all three color channels in the x/y plane with z-increments of 2µm. The resulting volumetric Pixel (VOXEL) was therefore measuring 0,5µm x 0,5µm x 2µm depicting a volume of 0,5 µm^3 of the specimen. This setting represents an a priori information loss (binning), as the setup used provides a maximum resolution of 0,25µm in x/y for each Pixel and increments in z can be reduced further resulting in significantly larger data volume. Imaging depth in z-direction was individually selected depending on the clearing efficiency within each specimen. Figure 5 shows a screenshot of the resulting three-dimensional image compounded from the x/y images within the z-stack.

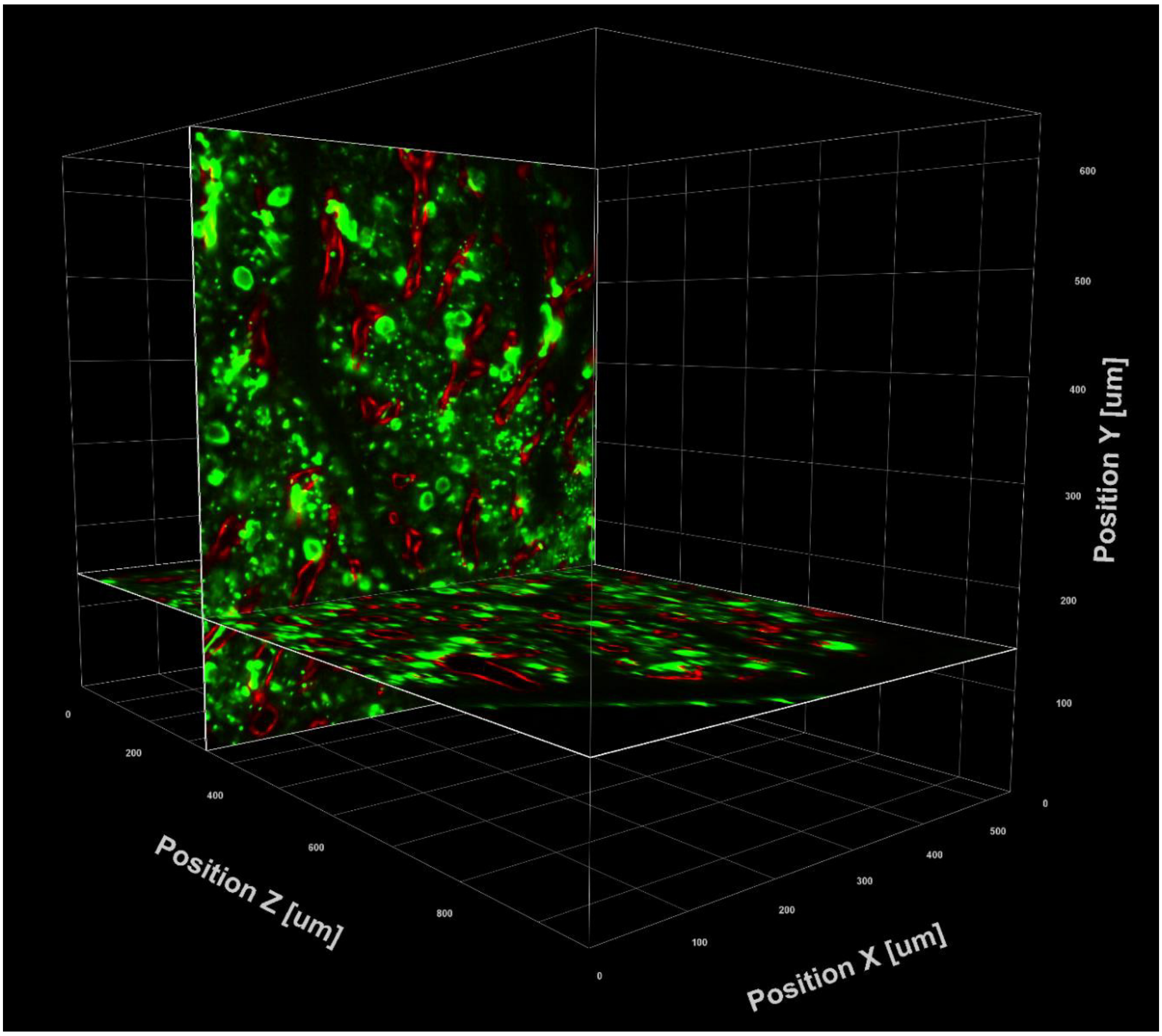

Figure 5: Maximum intensity projection (MIP) in selected x/y- and x/z-planes: Vessel (red), MK (green); grid: 100µm.

5.2. Crucial steps of the image analysis protocol

Visualization and data analysis were performed in three major steps: i) Image preprocessing using Imaris® 7.7.2 / 8.3.1 (Bitplane AG, Zürich, Switzerland) and FIJI (Schneider, Rasband et al. 2012), ii) segmentation of objects in Imaris® using Iso-surface and cell-algorithms and iii) data extraction from Iso-surfaces in Imaris® 7.7.2 / 8.3.1 (Bitplane AG, Zürich, Switzerland) (Stegner, vanEeuwijk et al. 2017). A detailed description of the image analysis protocol and a discussion of methods used is provided in chapter 6 of this thesis.

i) Image preprocessing

Image preprocessing within this research consists of three major steps: i) Removal of imaging noise as well as crosstalk (bleeding-through) of vessel signal within the MK channel, ii) enhancement of contrast in the image conserving object details and iii) Debris and background removal. Image preprocessing mainly utilized FIJI (Schneider, Rasband et al. 2012) including the Particle Remover plugin (Rasband 2000). Section 6.4.1 provides a detailed discussion of the customized image preprocessing pipeline applied to the MK project.

ii) Segmentation of objects

For segmentation of vessel- and MK objects within the 3D-stack, cell-algorithm was used in Imaris® 7.7.2 and 8.3.1 (Bitplane AG, Zürich, Switzerland). For generation of MK objects and for artificial filling of MK soma, additional steps utilized FIJI (Schneider, Rasband et al. 2012). Vessel-cell-objects were transformed to Iso-surface objects and processed using MAtlab software (Mathworks, USA) and the Imaris® XTension module for creation of distance transformation maps. Bone structures were derived from the auto fluorescence channel using Imaris® cell-algorithm for definition and estimation of the sample volume.

iii) Data extraction

Statistical analysis of data extracted consisting of object positions, numbers and volumes (MK, vessel, bone marrow), distance from MK to vessel (edge-to-edge) as well as quantification of the vessel interspace. Statistical analysis was performed using Microsoft Excel (ver. 2013, Microsoft Corporation, Redmond, WA, USA), Origin (ver. 8.6, OriginLab Corporation, Northampton, MA, USA) and Matlab software (Mathworks, USA) (Stegner, vanEeuwijk et al. 2017). Within the context of statistical analysis, a maximum distance of a single voxel (dimensions 0,5x0,5x2 μm^3) between vessel walls and the edge of MKs was classified as associated to the vessel structures (Stegner, vanEeuwijk et al. 2017).

6. Image analysis

The main scope of this dissertation deals with the processing of the imaging data and the subsequent reconstruction and volume rendering of the structures within the murine BM as discussed in Chapter 4. Within the following chapter, specific challenges resulting from this imaging project are discussed and a detailed problem-oriented description of the analysis protocol is provided.

6.1. Advantages of light sheet fluorescence microscopy

In the following section two gedankenexperimente are presented to portray the shortcomings of the CS-approach for imaging MKs and to put efforts for LSFM imaging of this project into perspective. Besides technological challenges such as limited field of view, specific morphology of MKs requires a tailored image acquisition and analysis.

6.1.1. Technological challenges of imaging megakaryocytes

Limited field of view in two-photon intravital microscopy

The setup of a two-photon microscopes is similar to a conventional confocal microscope. Major difference between these imaging techniques stem from the use of a specific excitation laser and modifications in the detection pathway (Helmchen and Denk 2005). 2P-IVM makes use of a nonlinear process in which two low-energy photons achieve a high-energy electronic transition in a fluorophore resulting in emitting of a higher-energy photon (Helmchen and Denk 2005, Svoboda and Yasuda 2006). In confocal microscopy as well as 2P-IVM, imaging is realized by a focused laser beam scanning the sample in a raster in a fashion (Svoboda and Yasuda 2006). When compared to LSCM, the principle of 2P-IVM has two key advantages (Svoboda and Yasuda 2006). First, the setup allows for an excitation of fluorophores almost exclusively within the focal volume (Zipfel, Williams et al. 2003) and therefore results in improved three-dimensional contrast and resolution (Svoboda and Yasuda 2006). Second, 2P-IVM significantly reduces the influence of light-scattering as near infrared photons penetrate tissue better and scattered photons are too weak to cause fluorescence excitation (Svoboda and Yasuda 2006). Reduced scattering and deeper penetration depth of near-infrared photons thus constitute the special advantage of 2P-IVM of an increased imaging depth (Helmchen and Denk 2005).

So far imaging depth of up to 1 mm have been reached for imaging of brain tissue (Theer, Hasan et al. 2003, Svoboda and Yasuda 2006). The depth-limit of imaging samples however depends on the properties of the sample tissue. Bone tissue particularly hampers photon penetration. Previous studies realized an imaging depth of up to 60µm for *in vivo* imaging of MKs in intact bone (Nishimura, Nagasaki et al. 2015). A small field of view of the raster scanning procedure as well as a limited penetration depth of the imaging technology thus drastically limit the field of view of the microscope. Despite being able to visualize the dynamics within the BM *in vivo*, this limitation of a small field of view restricts the amount of MKs within the specimen for a statistical analysis.

Imaging large-volume bone samples using cryosectioning and technological shortcomings

Traditionally, studies of larger volumes were performed by slicing the specimen and imaging the slices piece by piece in a conventional microscope or LSCM. Early studies hypothesizing elements of the current concept of megakaryopoiesis already made use of sectioning of organs in order to enable staining and subsequent microscopic observation of solid organs (Wright 1910). Each slice of the specimen represents a specific z-plane and can be aligned to a z-stack accordingly. Inherent challenges however hamper the applicability of this method for three-dimensional imaging. It is important to maintain the sequence of sliced samples for alignment as the thin slices might easily get mixed up. Moreover, individual slices may be damaged thus being excluded from imaging and alignment of the individual slices is almost impossible unless defined orientation points are provided. Ultimately, cutting artefacts lead to loss of information on the surfaces of the planes in z-direction (e.g. shear stress during the CS procedure). This loss of information on the three-dimensional structure may lead to a distorted representation of the original sample. It can thus be hypothesized that CS only provides an estimate of processes within the intact specimen and results of studies solely relying on CS might be limited in their validity.

Shortcomings of cryosectioning when imaging large objects reaching through multiple sections

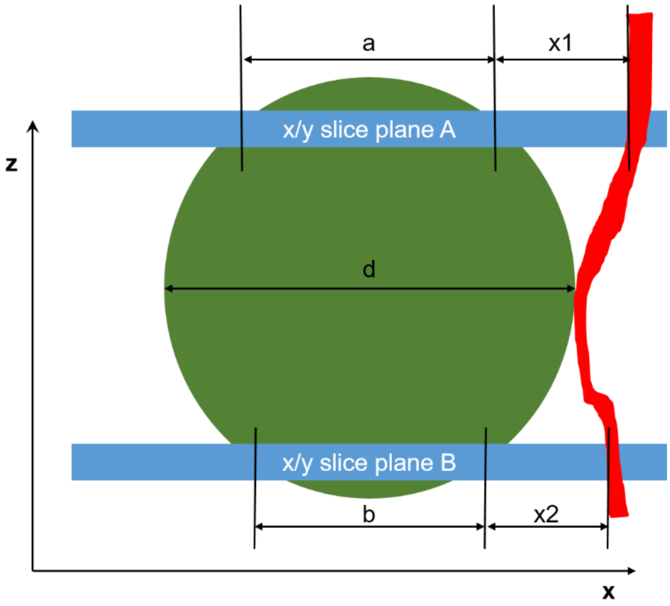

Figure 6: Gedankenexperiment 1.

Figure 6 portrays the impact of this loss of information in-between the imaging slices in the case of a perfect sphere on the resulting data in a first gedankenexperiment. Assumed the corresponding study seeks to evaluate the diameter *d* of this hypothetical sphere. The loss of information for CS is simulated in this case by limiting the information gain to data stemming from slices A and B. Depending on the position of the adjacent planes, resulting information might be distorted. For the case of Figure 6, the actual diameter d of this sphere would thus be significantly underestimated when only information *a* and *b* from slices A and B is available. An approximation and extrapolation of diameter and volume are in this case additionally hampered by potential offsetting due to difficulties in alignment and loss of information in-between slices.

In a next step we assume that the simulated CS study also aims at describing the distance of the sphere from vessel structures (red structure). Similar to the previously described situation for evaluating the diameter, the information in-between slices A and B is lost. An adequate evaluation of distances in three dimensions can therefore not be realized for this purpose. In the worst case, data derived from the simulated CS study in Figure 6 results in a portrayal of two different objects with diameters a and b which are located distant from the vessel (distances x1 and x2). A reconstructed 3D image from CS thus only provides an estimate on the position of individual cells in respect to blood vessels and other structures within the BM.

6.1.2. Influence of morphologic variability of megakaryocytes

As introduced in chapter 3, MKs perform drastic changes during their maturational cycle. During this cycle, MKs grow considerably in size and drastically change their morphological structure. The diameter of MKs reaches up to 100µm (Patel, Hartwig et al. 2005) whereas the size of MKs seems to correspond to DNA ploidy (Tozawa, Ono-Uruga et al. 2014). Furthermore, MKs show a highly variable morphologic structure when forming pseudopodial extensions (Wright 1910, Cramer, Norol et al. 1997, Italiano, Lecine et al. 1999, Italiano 2013).

The morphological inhomogeneity of MKs however particularly challenges the technique of CS as commonly used technology for studies on MKs. Key shortcomings of the CS approach for imaging MKs are demonstrated by expanding the gedankenexperiment introduced in Figure 6 in section 6.1.1. In this second gedankenexperiment, the spherical structure in Figure 6 is replaced by a complex form in Figure 7 representing an individual MK forming two distinct pseudopod-like extensions in z-directions in a x/z-plane. It is assumed that when performing CS, the MK in focus is represented in two adjacent sections (x/y slice plane A/B in Figure 8). Given the information-loss between the x/y-slices as discussed above, the resulting data from a CS approach is limited to data resulting from the x/y slices A and B. Given that the spectator is lacking information on an additional dimension as displayed in Figure 7, data resulting from planes A and B result in an identification of three individual objects. Without information of Figure 7, a coherence of these three segmented objects in Figure 8 may not be drawn.

Recognition of coherent objects when using CS for imaging MKs is thus hampered and in addition to shortcomings of CS discussed above, MK numbers might be overestimated whereas volume of individual MKs might be drastically underestimated. This second gedankenexperiment demonstrates the limitations of CS for imaging MKs. It shows that CS may yield

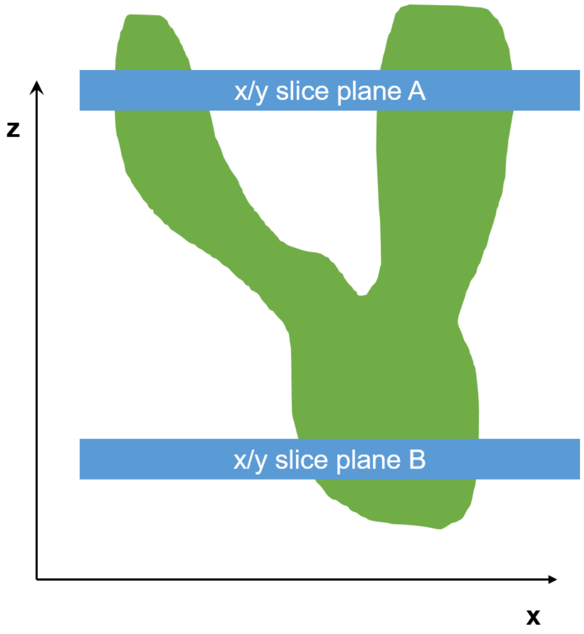

Figure 7: Gedankenexperiment 2.

insufficient data resulting in misinterpretation, faulty distance and incorrect description of MK morphology and volume.

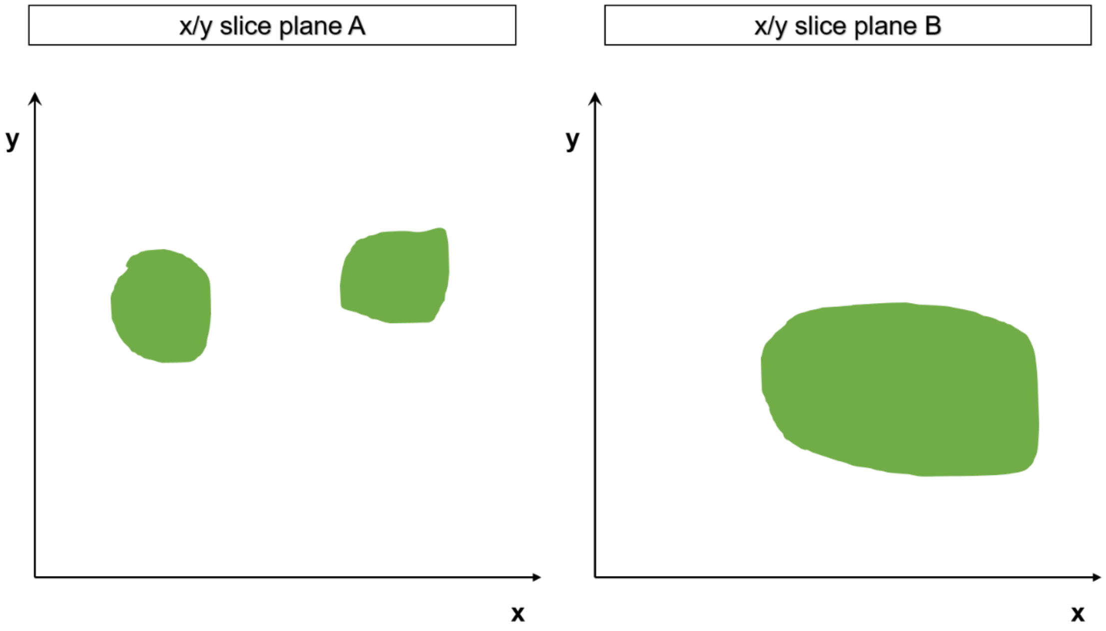

Figure 8: x/y of planes A and B of gedankenexperiment 2.

6.2. Biological challenges of imaging megakaryocytes in intact bone

When imaging intact bone, two major challenges arise. First, bone tissue is inherently inhomogeneous resulting in uneven clearing. Second, the inhomogeneous structure results in irregular staining and considerable crosstalk.

Inhomogeneous tissue

Bone structures form the endogenic skeleton of vertebrates consisting of a multitude of cells and structures collaborating in a manner to guarantee structural integrity. These organs have to meet specific mechanical properties to support the body structure. In a tightly controlled manner, osteoblasts and osteoclasts continuously build up and degrade the bone structure. This leads to increased bone density in areas of high mechanical stress and a lower density in areas where less strain occurs. Continuous modification of the bone structure in respect of local mechanical stress results in a highly inhomogeneous tissue considerably aggravating the clearing process. Remaining variations of refractive indices of tissue within the cleared specimen cause light scattering and irregular attenuation in the x, y and z dimensions. Strong background signal stemming from abundant tissue inhomogeneities reduce contrast for MK as well as vessel recognition (see Figure 20 as an example). Ultimately, information within the image is lost leading to unsharp images.

Irregular staining/crosstalk

For visualization of MKs as well as vessel structures, immunostaining was performed using cell surface markers combined with commercially available fluorophores. The result of the staining procedure depends on perfusion of tissue with antibody-labelled fluorophores as well as concentration of antigen on the surfaces of targeted structures. Figure 9 represents a typical image of MKs within this project and outlines the obstacles arising. Staining of MKs is particularly affected by staining inhomogeneities as their membrane is only partly or inhomogeneously labelled (see two top left cells in Figure 9). When setting threshold for cell recognition in these images, the cells may only be partly identified and the resulting segmented cells may not correspond to the original in shape or volume as intensity values of parts of the cell body are below the chosen threshold (see lower cell in Figure 9). Similarly, segmented cells may also be fragmented resulting in misinterpretation of volume and quantity.

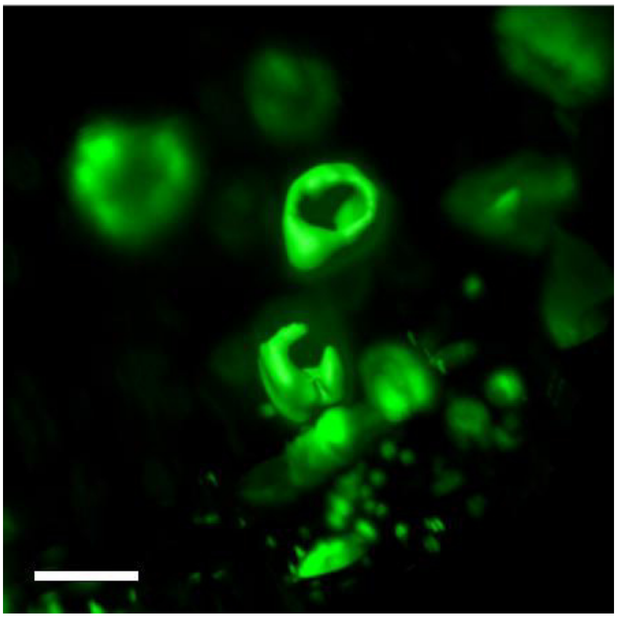

Figure 9: Mixed rendering; MK (green) voxel and isosurface; scalebar: 20µm; courtesy of Oguzhan Angay.

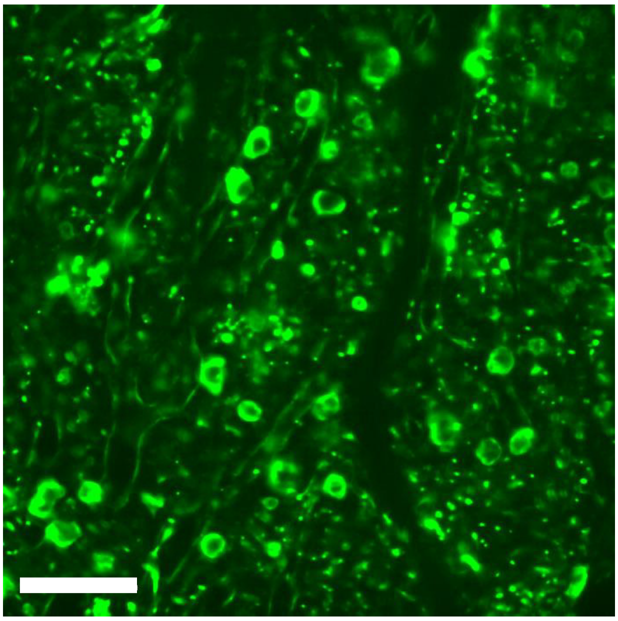

Figure 10: MK channel after imaging with significant crosstalk from vessel channel and background signal; scalebar 100 µm.

Furthermore, images of the MK channel within our project show significant fluorescent crosstalk from the vessel channel as can be seen in Figure 10. On average, the intensity of the fluorescence crosstalk corresponds to a signal intensity of 41% (minimum: 0,19, maximum: 0,78; σ = 0,14; *Table 2*) of the signal intensities in the MK channel. The intensity-values of the bleed-through channel are thus within the range of intensity-values of poorly stained MKs.

Result of membrane staining

The use of cell surface markers for staining large objects such as MKs may lead to a misinterpretation of the cell morphology. The lack of immunostaining of the MK cytoplasm may lead to the recognition of hollow structures. When applied to MK structures from the second gedankenexperiment in section 6.1.2, images from the x/y-planes gathered with LSFM microscopy technique may consist of hollow structures as displayed in Figure 11. An image segmentation protocol might therefore lead to a misinterpretation of MK shape and volume as MKs are recognized as hollow structures without a core or are simply identified as doughnut-like structures (Figure 9 and Figure 11).

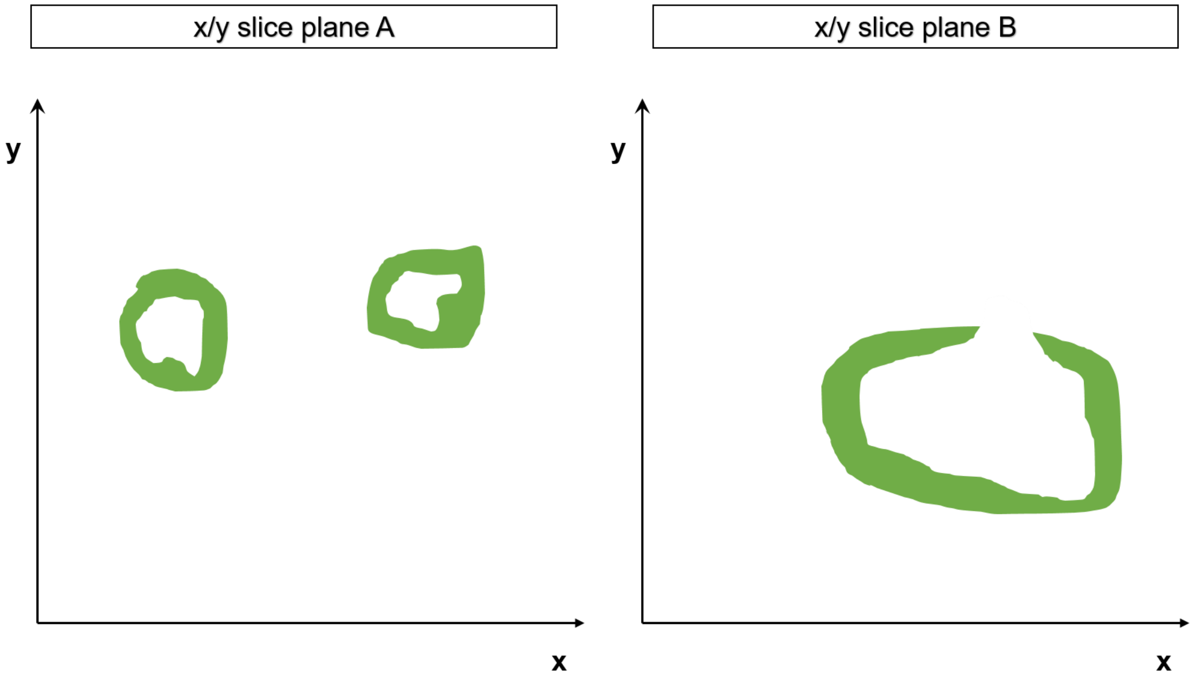

Figure 11: Follow-up on x/y of planes A and B of gedankenexperiment 2 (assumed membrane staining was applied)

Close contact of cells

Due to the considerable size of MKs, the cells are often located in close proximity to each other and tend to contact each other. This proximity and the irregular staining of cell membranes of individual cells additionally impairs a clear distinction between two neighboring MKs.

6.3. Technological challenges

In addition to the imaging challenges arising from the specimen characteristics, image analysis protocols need to account for specific properties of the imaging technology. The specifics of the microscopy setup are beyond the scope of this thesis; however, properties of the imaging setup need to be taken into account for design of an image analysis protocol. During image reconstruction, limited resolution in z-direction mainly hampered the reconstruction of MK and vessel structures from 3D LSFM data. A trade-off between field-of-view and light sheet thickness limited the maximum resolution in the z-direction. Each volumetric pixel (VOXEL) measures 0,5µm x 0,5 µm x 2µm and contains information on local signal intensity measured on a 11-bit intensity scale saved in a 16-bit container format when imported from the microscope. Within this project, the z-dimension particularly limited the accuracy of the segmented structures. A characterization of our LSFM setup demonstrates that thickness of the light sheet (calculated as 2 * 1/e²) depends on the excitation wavelength and approximately lies within a range of the 20-fold value of the z-increments (Figure 12).

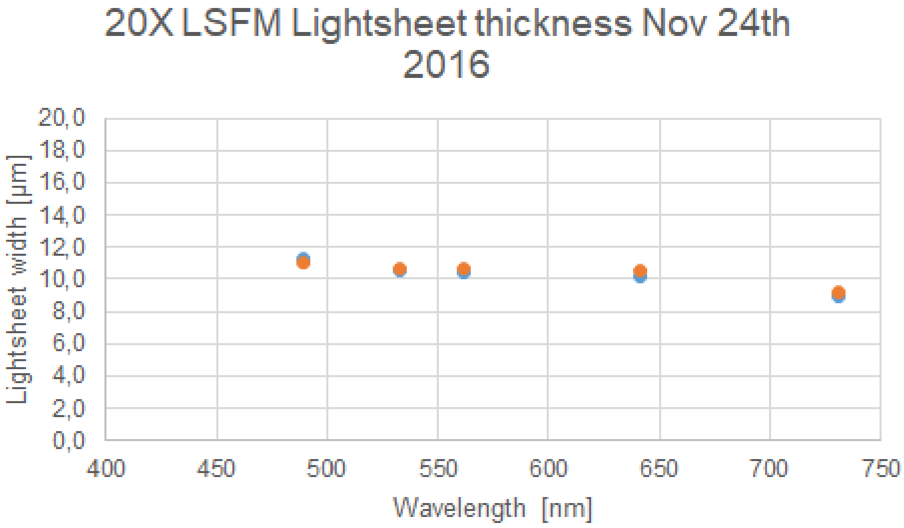

Figure 12: Light sheet thickness Nov 24th 2016; courtesy of Oguzhan Angay.

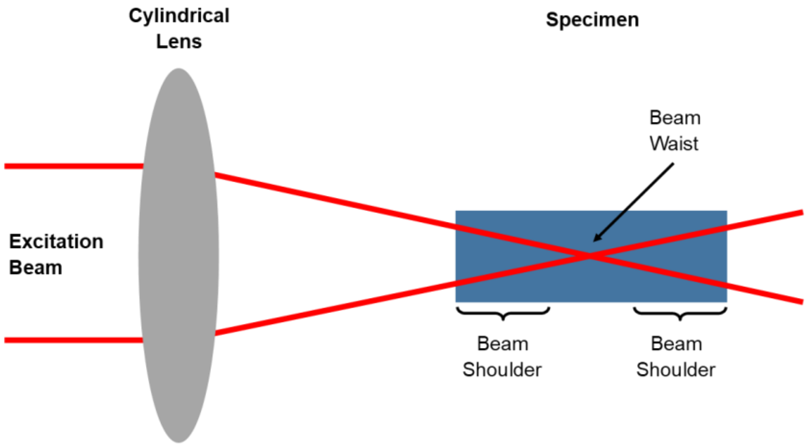

Figure 13: Simplified beam path; birds-eye view orthogonal to the light sheet

Furthermore, the beam path of the illumination light sheet does not exhibit this minimal thickness throughout the whole field of view as the light sheet is focused by a cylindrical lens. This is demonstrated in a simplified visualization of the excitation beam path in Figure 13.

Despite the step size of 2µm, the resulting three-dimensional reconstruction of the image stack therefore results in a long-drawn-out image of the cells in the z-direction when compared to the x/y plane (Figure 14). Each image thus partly corresponds to an overlay of fluorescence signals from the illuminated plane adjacent to the current position in z.

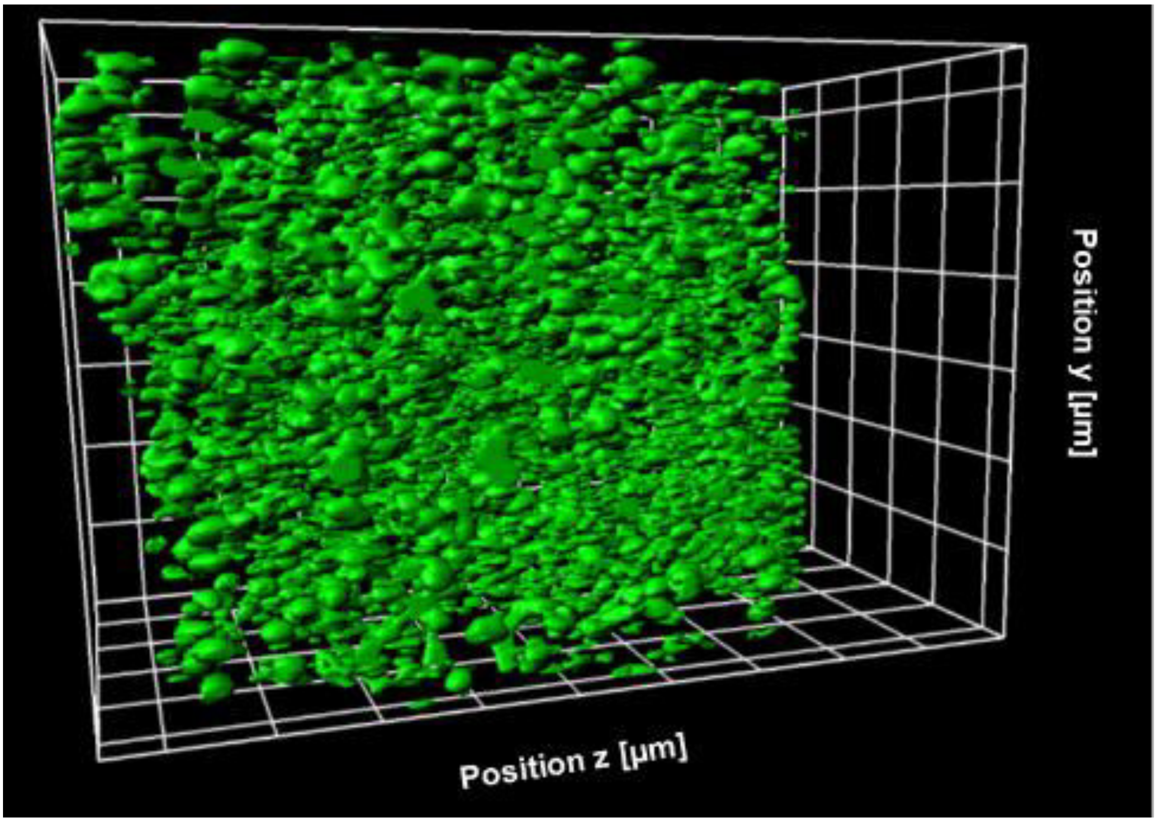

Figure 14: Isosurface rendering; MK (green); grid size: 100µm.

6.4. Image processing and object segmentation

The biological and technological challenges of imaging MKs in intact bone account for the need of a tailored image processing and segmentation pipeline. An approach for a robust processing and segmentation pipeline is introduced within the following section of this thesis. First, preprocessing is performed on raw imaging data to optimize the input data. In a second step, MK and vessel objects are segmented. Finally, statistical data from the segmented objects is exported to excel files for statistical evaluation and simulation.

6.4.1. Image pre-processing

i) Reduction of salt and pepper noise

In order to reduce the background noise within the image, in a first step a median filter is applied in Fiji (Schindelin, Arganda-Carreras et al. 2012, Schneider, Rasband et al. 2012, Schindelin, Rueden et al. 2015). Median filtering achieves efficient noise removal while preserving edges of the images and is generally used for “salt and pepper noise” removal in digital images (Jayaraman, Esakkirajan et al. 2009, Navjeet, Punetha et al. 2016, Tania and Rowaida 2016). Imaging noise may stem from transmission errors (e.g. bit errors), might be introduced during signal acquisition (e.g. dead pixels) (Arce, Paredes et al. 2000, Navjeet, Punetha et al. 2016) or may be the result of faulty file conversion. The median filter replaces each pixel within the image with the median value of the neighboring pixels within a defined region around the central pixel (Jayaraman, Esakkirajan et al. 2009, Tania and Rowaida 2016). Outliers of high or low intensity are removed (Arce, Paredes et al. 2000) while small details may be blurred (Sun and Neuvo 1994). The effect of median filtering is depicted in a simplified visualization in Figure 15. The ‘pixels’ with high intensity in positions 3, 10 and 17 are removed while the edges at positions 7/8 and 14/15 are preserved.

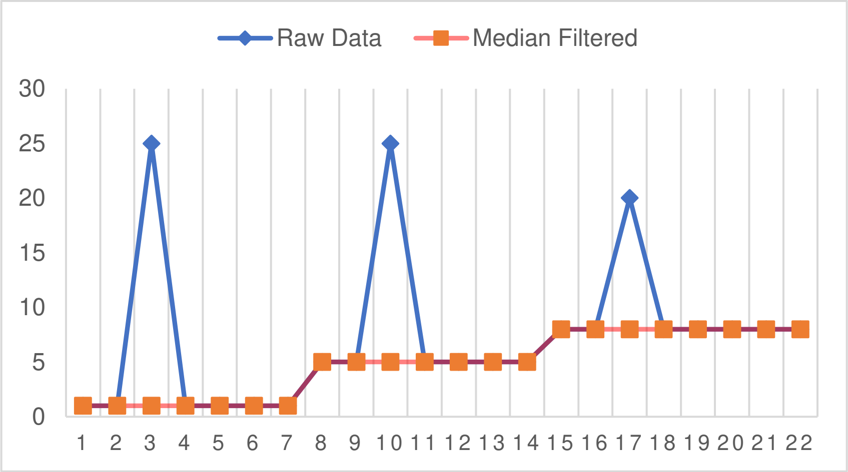

Figure 15: Simplified visualization of the principle of the median filter

For the purpose of this research, a median filter was applied to all channels recorded with the LSFM microscope consisting of the MK channel, the vessel channel and the autofluorescence channel with a radius of 2 pixels corresponding to a diameter of 2,5µm in orthogonal direction. A radius of 2 pixel thus corresponds to a box of 5x5 pixel. A radius larger than two pixel showed to be associated with loss of information on details of the MK protrusions and cell walls. Smaller radius did not effectively remove background noise. The filter was automatically applied slice by slice for the whole image stack.

ii) Removing fluorescence crosstalk

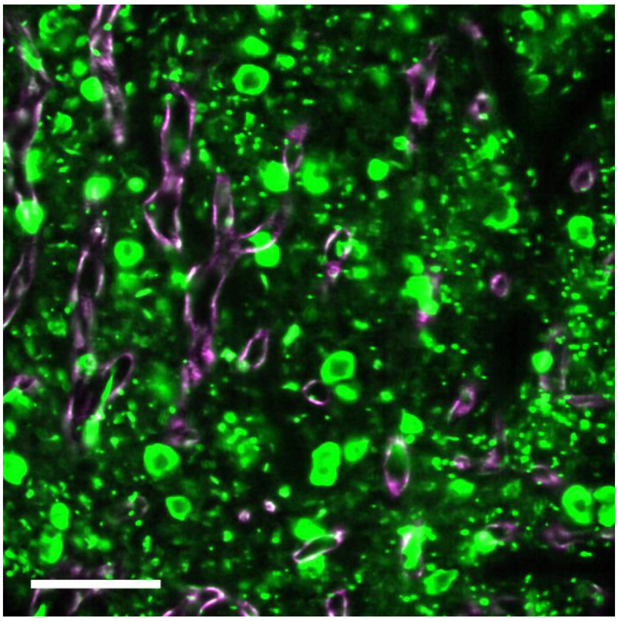

Figure 16: MK channel after imaging with significant crosstalk from vessel channel highlighted in purple; scalebar 100 µm.

Mature MKs are located in close proximity to vessel structures to release proplatelets. Data from 2P-IVM (Junt, Schulze et al. 2007) as well as a first impression from raw data within this project support the notion of MKs being in close contact with vessel structures. This proximity of MKs to vessel structures however aggravates distinction between individual MKs and vessel structures. Fluorescent crosstalk from the vessel channel seems to link the MKs in the stack to one another as crosstalk intensity values are within the range of intensity values of lightly stained MKs (Figure 10, fluorescent crosstalk highlighted in Figure 16). Image analysis software may therefore not be able to separate MK cells touching vessel walls. MK Segmentation without crosstalk removal thus results in a bulky structure where a large amount of MKs touching vessel structures are connected and interpreted as coherent objects. Removal of fluorescent crosstalk is therefore necessary to enable the detection of individual MKs.

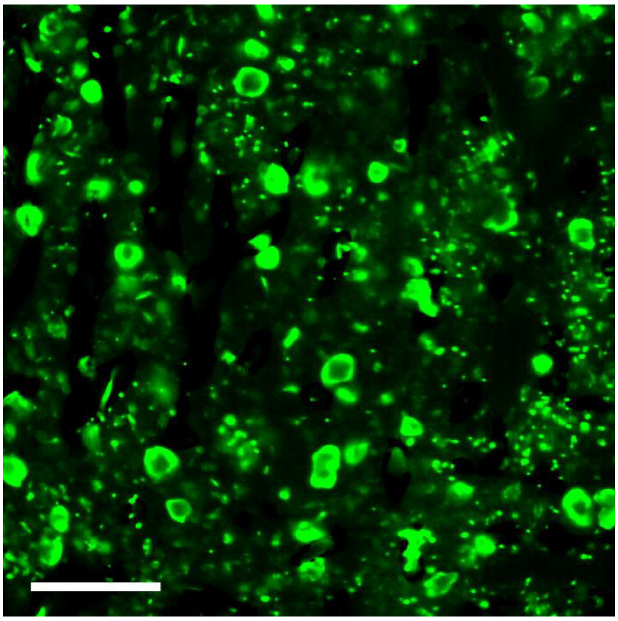

Figure 17: MK channel after removal of vessel crosstalk; scalebar 100 µm.

Crosstalk is removed by subtracting a weighted copy of the vessel channel from the MK channel. The weight is calculated from comparison of average intensity values of selected vessel structures exhibiting substantial crosstalk in the in the MK channel with the original channel. Mean pixel values are calculated for the vessel structures selected in individual regions of interest (ROI) in both channels. The quotient of the mean pixel value in the MK channel and the mean pixel value in the vessel channel constitutes the weight factor. Crosstalk removal needs to be performed in each image stack individually. This process cannot be performed using a standard weight factor for the whole project due to significant inhomogeneities within the different samples. Calculated weight factors ranged from 0,19 to 0,78 in this project with a mean of 0,41 (σ 0,14). Figure 17 demonstrates the effect of vessel crosstalk removal for the MK channel.

Removal of fluorescence crosstalk within the vessel channel did not benefit the object recognition in later stages and was thus only performed within the MK channel. It caused “holes” or notches in vessel walls where MKs touch the vessel structures.

iii) Removal of speckles within the megakaryocyte channel

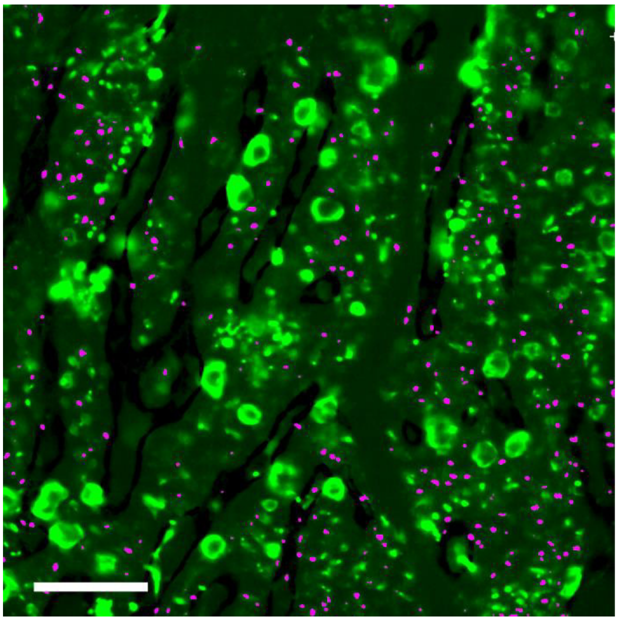

Figure 18: MK channel after removal of vessel crosstalk with highlighted speckles (purple); scalebar 100 µm.

After reduction of imaging noise and fluorescent crosstalk, a multitude of high intensity signals without connection to MK or vessel structures were still present within the image stacks (highlighted in purple in Figure 18). Due to their significant size, these high intensity signals were not removed by median filtering in the first filtering step. We assumed these ‘speckles’ to be originating from local accumulation of antibodies or platelets within the tissue or in capillaries. Before application of additional filters, these speckles were reduced in each imaging slice using “Particle Remover” plugin to Fiji in a binary image (Rasband 2000). Particles were removed in a binary version of the image stack. Definition of a threshold for transformation of the 16bit image stack to binary images is however highly user specific and prone to subjective evaluation. Careful setting of the threshold so that MKs and Vessel structures visible within each stack are represented as connected structures in this step ensured that neither MK nor vessel structures were affected (exemplary image of a typical threshold for binary transformation in MK channel is shown in Figure 19).

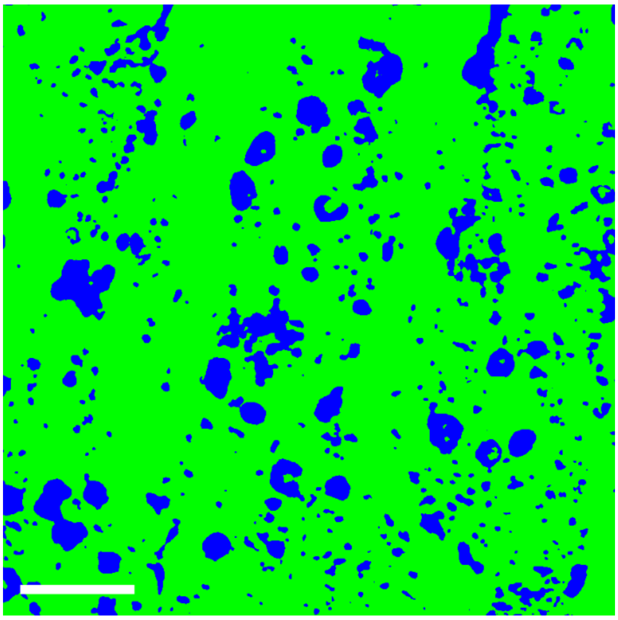

Figure 19: Typical threshold level for binary transformation during speckle-removal; scalebar 100µm.

From the binary images, speckles were identified by assuming that these structures are i) mostly circular structures and ii) within the size range of platelets. The particle remover was thus set in a first step to remove structures with circularity between 0 and 0,4. It was assumed that antibody or platelet accumulations are forming rather circular than complex structures. The size limit was set to an area of 100 square pixels (sqp) in the MK and 71 sqp in the vessel channel corresponding to a diameter of 2-5µm. Larger structures were removed so that the resulting channel consisted of information of potential speckles within the image stack. Subsequently the “speckle-channels” (purple structures in Figure 18) were subtracted from the original data eliminating the speckles. Resulting image stacks were transferred to Imaris®.

6.4.2. Attenuation correction and contrast enhancement

In a next step, a series of image filtering steps is applied to correct for heterogeneous attenuation, enhance the contrast and to minimize the influence of varying tissue densities.

i) Layer normalization

In a first filtering step, the heterogeneous attenuation of the image stack is reduced using the ‘Normalize Layers’ function in Imaris®. Heterogeneous attenuation between the individual imaging planes mainly occurs because of impairment of the light sheet entering the specimen (e.g. remaining muscle tissue at the illumination side) or due to absorption of the fluorescent signal with increasing z (when imaging deeper within the specimen). In a perfectly cleared specimen, these factors would be negligible. Despite advances in clearing bone tissue, these factors impede threshold definition for the whole image-stack for object segmentation. As result of irregular attenuation, threshold-levels are different for the individual imaging planes. Threshold values defined for image planes on the top of the stack for example are likely to be too high for planes deeper in the sample, as average intensity is reduced with increasing z as the fluorescent signal is mitigated through the sample. Correction of the attenuation is realized by adjusting the intensities of each z-slice with a linear transformation matching the mean and standard deviation values calculated for the whole stack (Bitplane 2013). Volumetric pixel with an intensity value of zero are considered background and are not included in the calculation.

ii) Application of a three-dimensional gaussian blur

Tissue and clearing inhomogeneities account for similar variation of intensity levels of specific regions within the image stack. Using three-dimensional Gaussian blurring with a large σ of 100 in x, y and z in FIJI (Schindelin, Arganda-Carreras et al. 2012, Schneider, Rasband et al. 2012, Schindelin, Rueden et al. 2015), intensity levels of regions within the image stack are adjusted. The Gaussian Blur filter acts as a low-pass filter (Ferreira and Rasband 2012) where high-frequency signals are reduced and details are blurred (Deng and Cahill 1993, Buades, Coll et al. 2005). By inverting the blurred image and adding the result to the initial stack, local variations of intensity levels are reduced. Baseline intensity values in the image stack vary in a similar fashion and subtraction of the blurred image preserves details while adjusting the low-pass baseline values.

Subsequent to the Gaussian Blur, an unsharp mask filter was applied to the image stacks in Fiji (Schneider, Rasband et al. 2012) to realize local contrast enhancement and sharpening of the images (Ferreira and Rasband 2012). The unsharp mask filter creates an unsharp version of an image and subtracts this version from the original image (Fisher, Perkins et al. 2003). As a result, high frequency components such as edges are enhanced when choosing a small filter radius (Fisher, Perkins et al. 2003). Choosing a larger filter radius results in contrast enhancement for areas or objects within the image (Ferreira and Rasband 2012). In this project, a relatively large filter radius was chosen (r = 50 pixel) so that the signal of poorly stained MKs in areas with high background signal was enhanced. This chosen radius of 50 pixel proved to be most efficient for image processing, as larger values resulted in halo-signals around MK objects. Finally, two-pixel median-filtering was applied subsequently to reduce imaging noise introduced by image-processing similarly to 6.4.1 i).

iii) Background subtraction in Imaris®

The image processing so far accounted for heterogenous attenuation and intensity variations within the individual planes as well as locally. However, despite application of the three-dimensional Gaussian Blur and other filtering steps, the background signal within the image stack remains uneven. The uneven background hampers a global threshold selection for object segmentation and therefore needs to be reduced. In Imaris®, background subtraction using a “rolling ball” algorithm is performed based on application of a Gaussian filter for each voxel (Bitplane 2013). The algorithm subtracts smooth and continuous backgrounds from the images using a ball-like or parabolic structure with a defined radius (Sternberg 1983, Ferreira and Rasband 2012). To ensure preservation of MK or vessel details within the imaging stack, the diameter of the largest MK or vessel structure is measured for an estimate on the optimal radius for background subtraction in each channel. Structures with a diameter larger than this are basically considered as background and subtracted from the image. Each slide within the 3D-stack is processed sequentially.

Figure 20 visualizes the impact of pre-processing on the slices within the 3D stack. It depicts one of the x/y planes within an image stack. Image A represents the unprocessed image and Image B shows the effect of the image preprocessing as introduced so far.

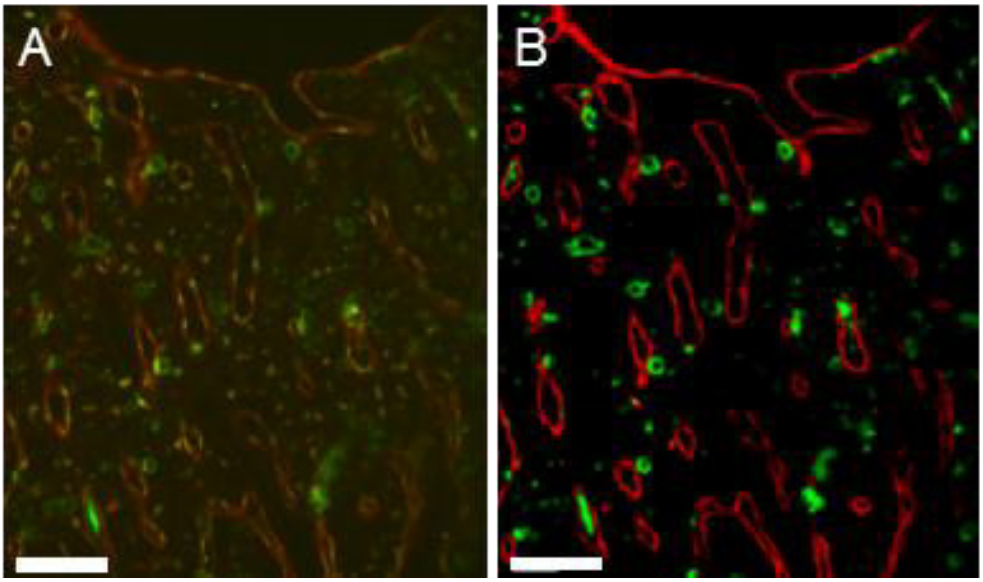

Figure 20: Stack slide before (A) and after (B) pre-processing; vessel (red), MK(green); scalebar: 100µm

6.4.3. Megakaryocyte core volume generation

For recognition of MK structures, immunostaining of the MK membrane with an anti-GPIX (CD 42a) antibody was performed as introduced in chapter 4.3. Due to the relatively large size of MKs in conjunction with the thin imaging plane realized, MKs appear as hollow circle- or doughnut-like structures as depicted in Figure 21. Using these images for object segmentation with Imaris® cell-module resulted in segmentation of similarly hollow objects in 3D. Furthermore, these hollow objects were often not recognized as individual cells during cell segmentation. In many cases, the cell-algorithm separated these hollow objects and performed incorrect splitting. Segmentation of data from Figure 21 with Imaris® results in a hollow structure which is separated into several smaller objects (Figure 22).

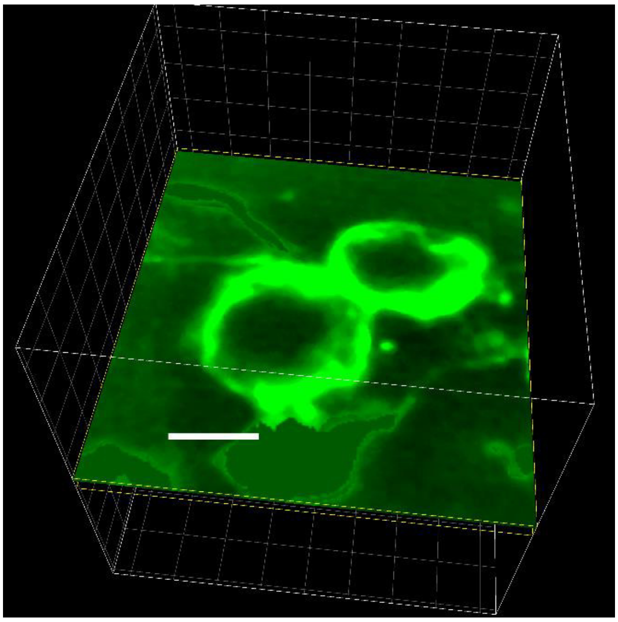
Figure 21: Voxel image (MIP) in selected clipping plane; MK (green); grid: 20µm.

For proper MK segmentation, hollow MK structures thus need to be filled and the MK somata reconstructed. Within this project, MK somata were reconstructed in 2D for each of the x/y slices in Fiji (Schindelin, Arganda-Carreras et al. 2012, Schneider, Rasband et al. 2012, Schindelin, Rueden et al. 2015) using a binary mask of the MK data. The most critical step for MK soma generation consisted of threshold definition for a transformation of MK data to a binary image similarly to 6.4.1 iii). The threshold is defined for each image stack individually so that the majority of MKs is captured in the binary image. Using the 'fill holes' operation in Fiji, hollow and circular structures within the individual binary slices are detected and signal is assigned to the center of these structures (Ferreira and Rasband 2012). Information on the artificial soma added to the binary image was extracted by subsequent subtraction of the original binary channel prior to the 'fill holes' operation. To reduce newly introduced imaging noise and influence of smaller 'somata' resulting from artifacts such as MK protrusion

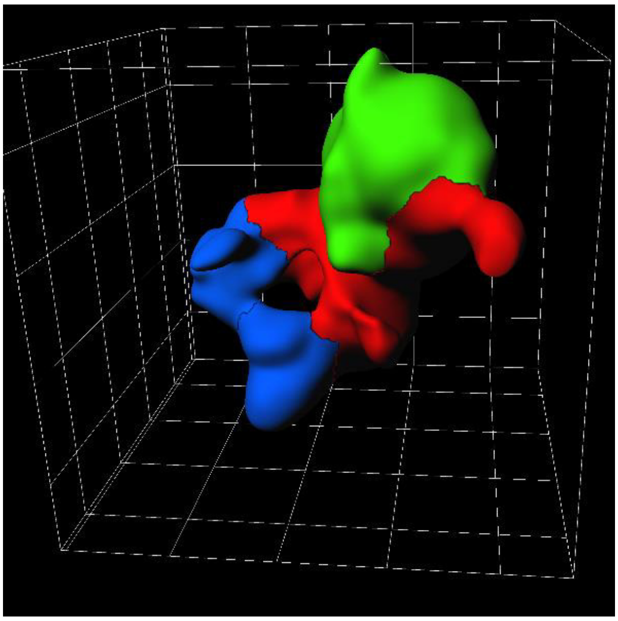
Figure 22: MK object rendering; individual MK objects (green, red, blue); grid: 20µm.

entanglement, it was assumed that all objects with a sphericity of 0 to 0,5 or a size of 0 to 100 pixels do not constitute MK soma and were excluded from further image processing using the Particle Remover (Rasband 2000) in Fiji (Schneider, Rasband et al. 2012). The resulting image stack was transformed to 32 bit for further processing in Imaris®. In Imaris®, artificial somata were segmented using the iso-surface algorithm with automatic threshold detection. Within the segmentation algorithm filters ensure only MK soma are considered which at least span over three consecutive planes and represent relatively round structures following the above-mentioned assumption. The settings for these two filtering steps were empirically found and proved to be most effective in critical selection of real MK somata. The resulting MK soma of the objects in Figure 21 are represented in (purple objects in Figure 23). Consequently, the MK channel was masked using the newly created MK soma Iso-surfaces for filling of the structures. Figure 24 demonstrates the effect of this operation, as the two neighboring MKs are now recognized and separated correctly in the following MK segmentation steps.

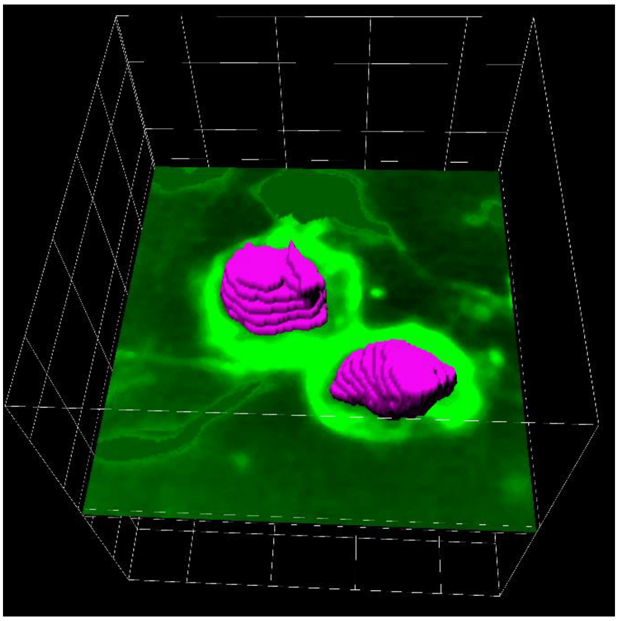

Figure 23: Mixed rendering; MK (green) voxel and MK soma isosurface (purple); grid: 20µm.

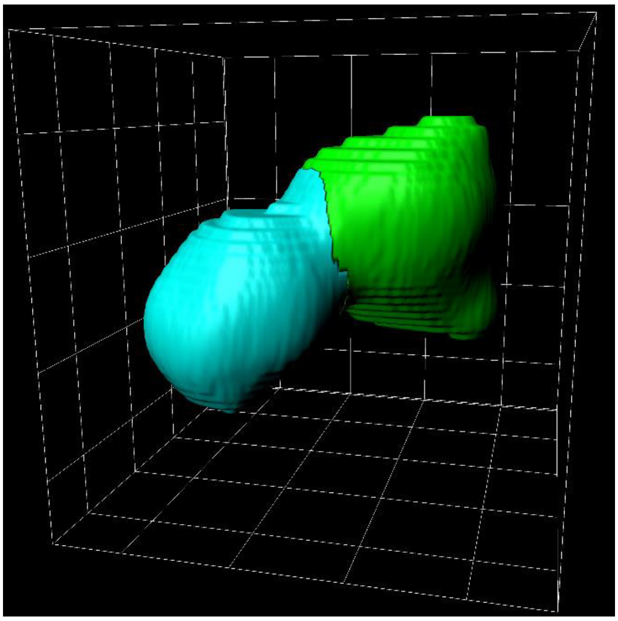

Figure 24: MK object rendering; individual MK objects (green, light blue); grid: 20µm.

6.4.4. Sequential segmentation of megakaryocytes

Segmentation of the individual MKs in a semi-automated manner using the Imaris® cell-algorithm was considerably improved after preprocessing of the MK channel and filling of MK somata. The Imaris® Cell module was designed for identification of cell, nucleus and vesicles in two and three-dimensional images (Bitplane 2013). When generating iso-surfaces, the segmentation algorithm performs identification of voxels belonging to an object based on the intensity value of the voxel in relation to the selected threshold (Bitplane 2013). The cell-algorithm on the other hand is specifically designed to detect cell objects and provides features such as cell membrane or cytoplasm detection (Bitplane 2013). Cytoplasm detection resulted in a more accurate detection of MKs during the course of this research. The setting of cell membrane detection resulted in additional artifacts; possibly due to the thickness of the “membranes” in captured images. On the other hand, artificial filling of MK objects (section 6.4.3) rationalizes the selection of cytoplasm detection in Imaris® Cell.

Prior to final MK segmentation, remaining artifacts were reduced by a final “garbage-removal” in 3D. It was assumed that structures (segmented as iso-surfaces) with a volume smaller than 524µm^3 with a relatively high sphericity (0,75-1) in the MK channel with a low intensity threshold (approx. 1/4 of the automatic threshold) were considered artifacts (e.g. accumulation of antibodies or platelets or imaging noise) and consequently removed from the channel. A threshold as low as a quarter of the automatic threshold ascertains that most of the voxel carrying signal intensity information are included in the surface generation. On average, the intensity values of immunostained objects (MKs) are by far higher. These appear as large structures which tend to cluster together to form coherent objects with a volume larger than or equal to 524µm^3 preventing loss of information for MK objects.

For a semi-automated MK recognition, the significant variations of MKs in volume and morphology particularly hamper the object segmentation. MKs in close proximity or cohesive to one another may appear as single large volume MKs. Large volume MKs on the other hand may be split up. Additional methods to characterize segmented objects within the cell-algorithm such as sphericity or dimensions in x/y/z were not applicable due to the morphologic heterogeneity of MKs.

For characterization of MK objects, the intensity threshold as well as volumetric characterization therefore constituted the critical parameters in MK segmentation. The MK intensity thresholds were adapted for each image stack individually to maximize MK recognition based on a preview of the segmented objects in the Surpass View. In the Imaris® cell-algorithm, setting thresholds serves as definition of regions in which the algorithm is expected to run (Bitplane 2013). To accommodate the volumetric heterogeneity of MKs, segmentation was performed in a sequential approach.

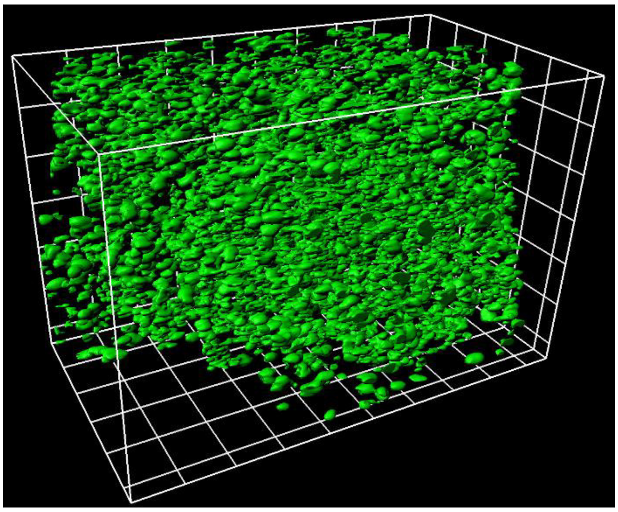

Figure 25: Cell-surface rendering; combined MK20- and MK10-objects (green); grid: 100µm.

In a first step, MKs were segmented with volume ranging from 4188µm³ to 45.000 µm³ (MK20). Segmentation 'trial runs' with different settings showed, that objects larger than 45.000 µm³ of volume consist of an agglomeration of smaller MKs. These can be more easily separated when segmenting smaller volume MKs in the following step. Subsequently MKs with volume larger than or equal to 524µm³ corresponding to a sphere of 10µm diameter (MK10) were segmented from the preprocessed and filled MK channel without already segmented objects from the previous steps. Smoothing was applied for segmentation in both steps as it helps to overcome minor staining inhomogeneities. For separation of coherent objects (such as objects in Figure 24), splitting of objects was performed using the "split cells by seed points" option (Bitplane 2013). Seed point diameters were set to 20µm and 10µm for MK20 and MK10 objects and defined by a theoretical value of "seed point quality". When splitting objects, seed points are placed at the center of each potential object. The region around the individual seed points grow and it is continuously evaluated if neighboring voxels are part of this object until an edge or border is found (Bitplane 2013). Cell objects were transferred to Iso-surfaces to allow for creation of the MK10 source channel as cell objects cannot be used for masking operations. MK20 and MK10 objects were ultimately combined to form the segmented MKs within the image stack (Figure 25).

6.4.5. Segmentation of vessel structures

For the segmentation of vessel structures in Imaris® Cell, a specific segmentation pipeline was developed to account for characteristics of input data from the pre-processed vessel channel. Just as MK objects, vessel structures show a high morphologic diversity. Small capillaries as well as afferent and efferent vessel structures represent an interconnected structure spanning the whole image stack. Vessel structures thus consist of fine structures connected to large-volume components. Furthermore, immunostaining of vessel structures performed within this research resulted in an uneven staining appearing as net-like structure of vessel walls

(Figure 26). Finally, due to immunostaining of the vessel endothelium (anti-CD105) as well as the inherent nature of vessel structures being hollow, lumen of vessel structures could not be stained (highlighted volume in Figure 27). This resulted in a representation of hollow structures for larger vessel structures possibly leading to misinterpretation of volume information on these objects.

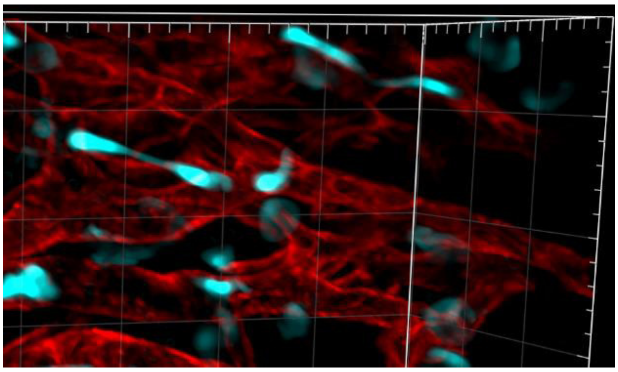

Figure 26: Maximum intensity projection of vessel (red) and MK (cyan) pre-processed data; grid: 50µm.

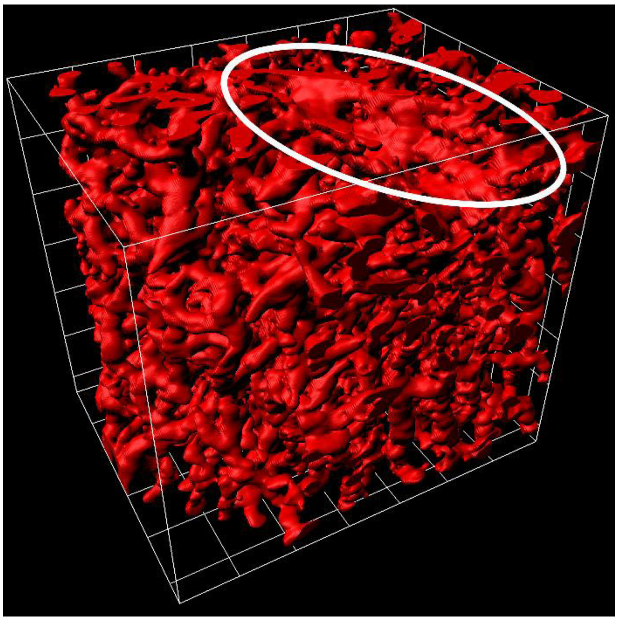

Figure 27: Cell-surface rendering; vessel objects (red); grid: 100µm.

Within this research, a smoothing parameter of 4µm proved to be most efficient in fulfilling a compromise of sufficient detail preservation (capillaries) and compensation for staining inhomogeneities (net-like staining). This parameter was empirically determined by critical evaluation of segmented structures in comparison with the pre-processed images. Smoothing parameters greater than 4 µm resulted in loss of detail whereas parameters less than 4 µm did not result in homogeneously closed vessel walls.

Hollow vessel structures on the other hand were manually filled by reconstructing the vessel trunk for larger vessel structures. In contrast to MK segmentation, reconstruction of vessel trunks was not contributing to the segmentation of the vessel structures themselves. Vessel trunks primarily served statistical purposes in later stages for an evaluation of the vessel volume and to avoid being included in calculation of vessel interspace (section 6.4.7). Vessel trunks were reconstructed using a supplementary channel created from Vessel- and BM Iso-surfaces (section 6.4.6). In a first step all Voxels outside vessel structures were assigned to a high intensity value. Voxel within the segmented BM were subsequently defined to hold an intensity value of zero. Remaining signal within this supplementary channel is neither part of vessel structures nor the BM and thus represents the vessel lumen and is segmented using the Iso-Surface algorithm in corresponding ROIs. Intensity thresholds for vessel segmentation were defined for each image stack individually using the automatically generated threshold value as a reference point and the preview within the Surpass view for finetuning. Figure 28 displays the segmented vessel trunk segmented for vessel objects from Figure 27. The segmented trunk fills hollow vessel structures as illustrated in Figure 29.

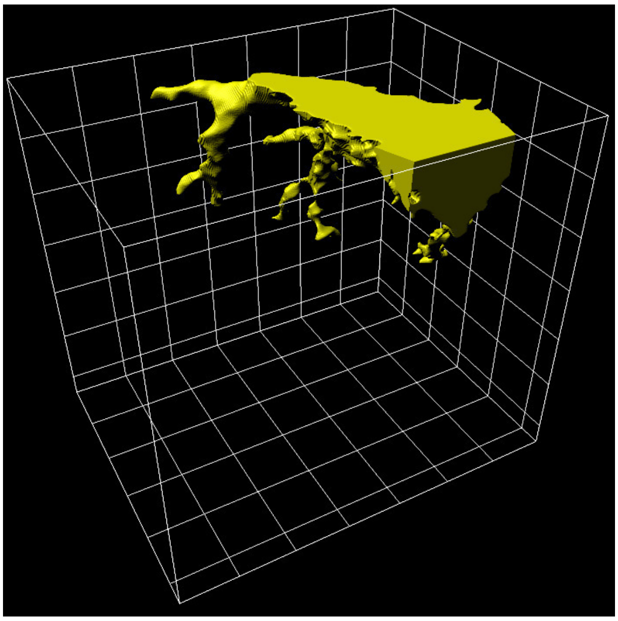

Figure 28: Cell-surface rendering; segmented vessel trunk (yellow); grid: 100µm.

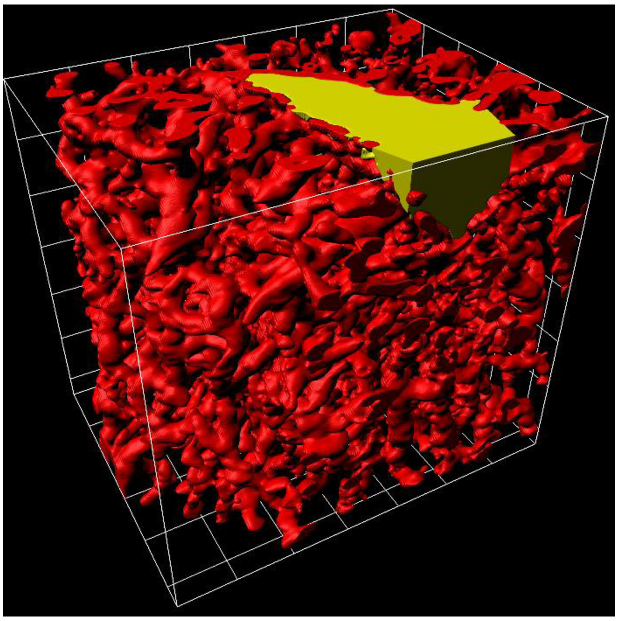

Figure 29: Iso-surface and cell-surface rendering; vessel objects (red) and vessel trunk (yellow); grid: 100µm.

6.4.6. Segmentation of bone marrow

For a deeper understanding of hematopoietic processes within the bone as well as for segmentation of vessel trunks (section 6.4.5), the BM within each image-stack needed to be segmented. The BM can be described as unique environment within the interspace between vessel and solid bone structures such as bone trabecula. Information on the volume of BM supports an understanding of the relation between vessel, MK and BM volume as it provides a quantification of the space theoretically available for megakaryopoiesis.

Within this research, efforts in immunostaining were focused on the identification of vessel and MK structures (Stegner, vanEeuwijk et al. 2017). The BM thus had to be reconstructed from information within channels available including autofluorescence. The autofluorescence channel had only been processed with the 2-pixel median filter so far to reduce imaging noise. After being masked with the previously segmented vessel structures (set voxel intensity-values inside to zero), we received an image stack in a swiss-cheese fashion providing autofluorescence information on the vessel interspace. BM was segmented from this masked channel using the Imaris® Cell algorithm (Figure 30). Intensity thresholds were defined for each image stack individually. A preview in the Surpass view allowed threshold definition as autofluorescence signal proved to be significantly higher in BM areas. By careful determination of the threshold, a clear distinction between BM structures and bone grafts or surrounding tissue could be made.

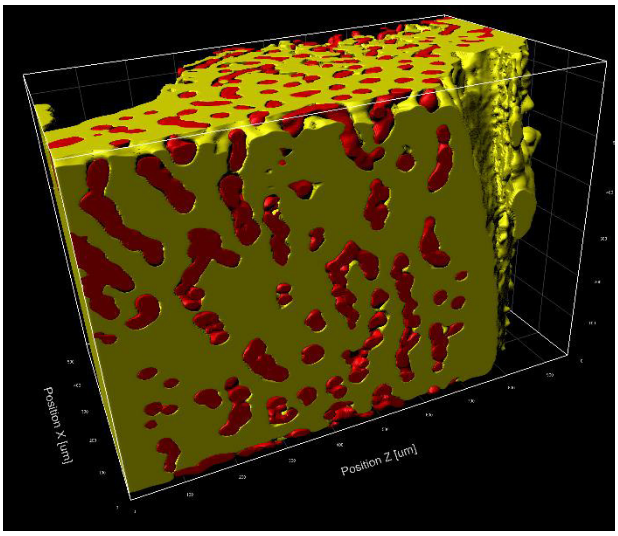

Figure 30: Cell-surface rendering; vessel objects (red) and BM (yellow); grid: 100µm.

6.4.7. Quantification of vessel interspace

For a quantification of vessel interspace, Distance transformation maps were calculated using a Matlab XTension within Imaris® for the segmented vessel objects. Distance transformation maps allocate intensity values to each voxel outside the surface objects representing the distance to the closest vessel wall within the three-dimensional image stack. These distance measures are calculated independently from specific imaging planes and allow an accurate measure of the distance of every single voxel in relation to the closest vessel object as a space diagonal.

Based on the distance transformation maps, quantification of vessel interspace is realized using local intensity maxima. For an extraction of statistical information on local intensity maxima, objects needed to be created in Imaris®. Spots objects are able to model such point-like structures within the 3D stack and can be used for statistical analysis of this purpose (Bitplane 2013). Prior to segmentation of spot-objects, contrast enhancement is applied to duplicated distance transformation maps using the unsharp-mask filter in Fiji (Schneider, Rasband et al. 2012). This procedure was intended to reduce the linear and continuous intensity flow within the distance maps and to create “sharpened” local maxima. Parameters set for this filtering step were critically determined empirically and Spot-objects were segmented subsequently. In contrasts to previous object segmentation steps, automatic definition of spot-intensity thresholds lead to the required spot generation along the local maxima. A minimum intensity-value in a median filtered version of the masked marrow channel (median filter previously applied with radius of 20 pixels) was defined for each image stack individually in the Surpass-preview and included as condition during spot-generation. This ensured that spot-objects were solely generated inside the BM within the vessel interspace (Figure 31). Distance information for the spot-objects was extracted from the original distance transformation channel derived from the Matlab XTension (maximum intensity within Spot object). Statistical information on Vessel structures, vessel trunks, MKs, bone marrow and Spot-objects were exported to excel files for further statistical analysis.

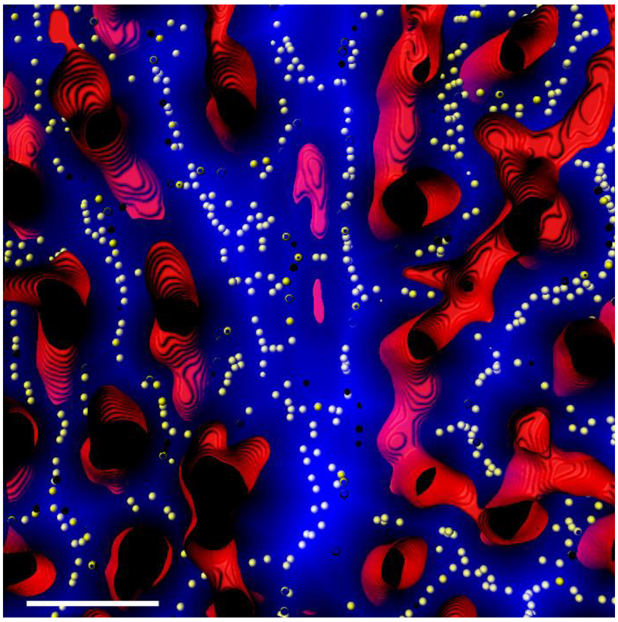

Figure 31: Mixed rendering; vessel (red), distance transformation (blue), interspace spots (yellow); scalebar: 100µm.

7. Results of statistical analysis and discussion

Within this research, a three-dimensional reconstruction of the entire bone was realized. Due to the high number of individual MKs analyzed, this study provides solid statistical evidence for processes within the BM. The statistical data from the LSFM was used as template for computational simulations.

Figure 32 outlines the sequential process of data extraction. Information is based on the position and volume of the MKs within the time series experiments. Combined with data from segmented BM and the vessel structures, information on MK, vessel or BM density is obtained.

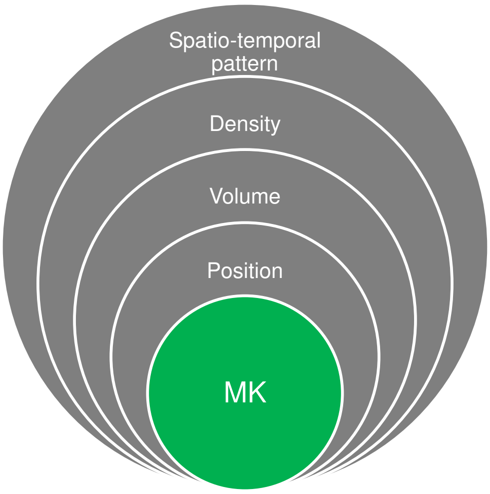

Figure 32: Data extraction from MK objects.

7.1. Advantage of light sheet fluorescence microscopy over cryosectioning

In section 6.1.1 and 6.1.2 two gedankenexperimente were introduced to demonstrate the shortcomings of the classical approach of cell imaging within the BM. Based on the data derived from this research, together with Oğuzhan Angay (OA) I performed a simulation of cryosectioning and compared the results of this approach to the actual data. The simulation was realized by virtually slicing the 3D stack in Imaris® and segmenting MK as well as vessel objects based on the virtually cryosectioned image.

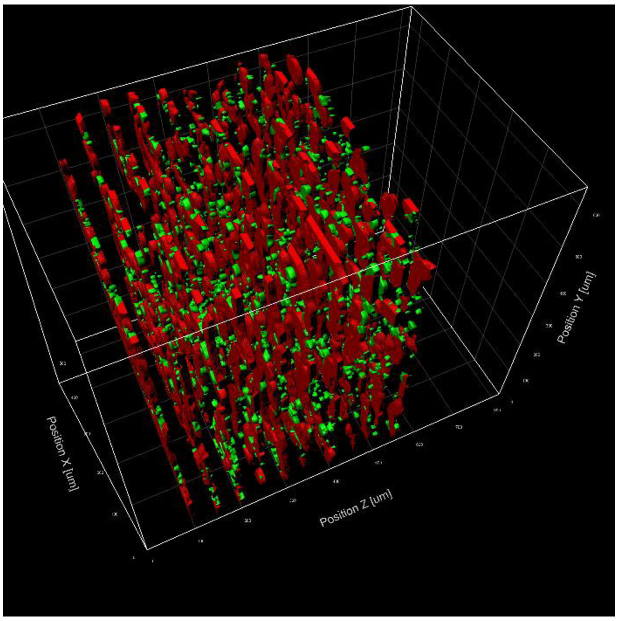

Figure 33: Isosurface rendering for simulation of cryosectioning; vessel (red), MK (green); grid: 100µm.

An image stack of approximately 750µm in z was artificially cut into 20 planes with a thickness of 6µm (Figure 33). In order to simulate cutting artefacts, OA and I considered an equally distributed gap in between the single planes. Comparison of the virtually sliced stack with the original data confirmed the hypothesis derived from the two gedankenexperimente that the three-dimensional information within the image stack significantly improves quantitative cell analysis (Figure 34). MK data is likely to be misinterpreted when “off-center” cell slicing occurs and vessel distances are falsely interpreted when only two-dimensional measures are considered. Based on the analysis I contributed to, it is shown that sectioning the bone results in an underestimation of MK diameter and volume. Analyzing the three-dimensional LSFM data sets thus provide significant gain of information when compared to conventional cryosectioning. Results from this study (Figure 36) also indicate that a higher percentage of MKs is localized in direct contact to vessel structures when compared to results from cryosectioning (Stegner, vanEeuwijk et al. 2017). It can be hypothesized that this results from loss of information on vessel structures just above or beneath the planes of bone sections (Stegner, vanEeuwijk et al. 2017).

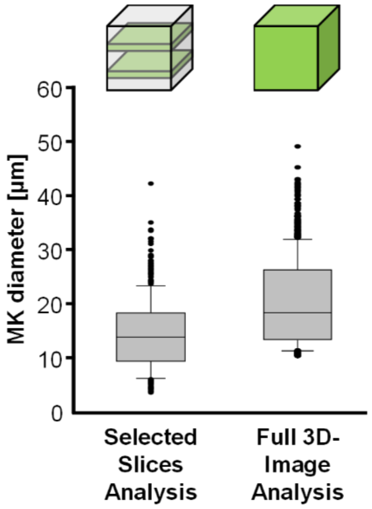

Figure 34: Statistical results of "simulated" cryosectioning and actual LSFM data, courtesy of Oguzhan Angay. Bar graphs represent mean ± SD.

7.2. Megakaryocytes primarily reside in close proximity to the vasculature

One of the main hypothesis within this research was based on observation in 2P-IVM indicating low migratory movements of MKs during maturation (Junt, Schulze et al. 2007). Reconstruction from the intact bone imaging revealed a dense vascular network spanning the BM where vessel interspace seems scarce (Figure 35). Figure 35 demonstrates that a high amount of MKs is densely packed within the intervascular space. It seems, that there is hardly any space in between vessel structures. The vasculature is so densely

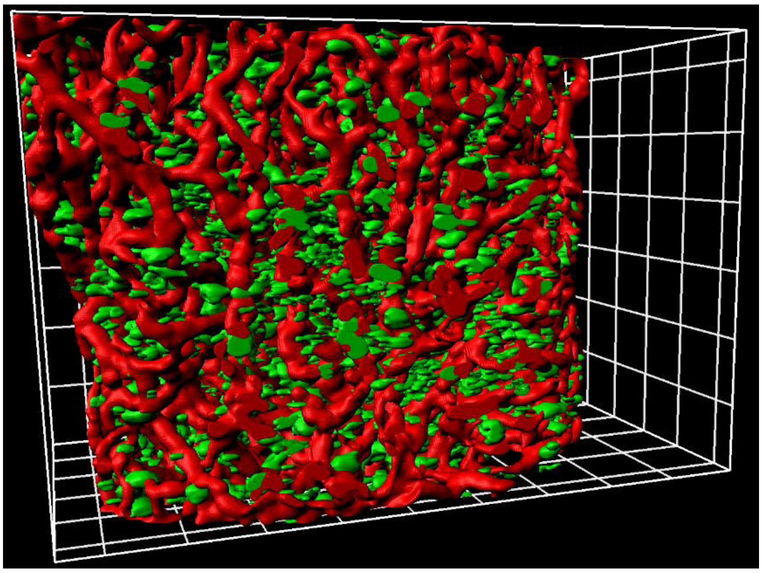

Figure 35: Final isosurface rendering; vessel (red), MK (green); grid: 100µm.

packed, that the remaining vessel interspace in our reconstructed images simply leave no space for specific niches for the stages of MK development.

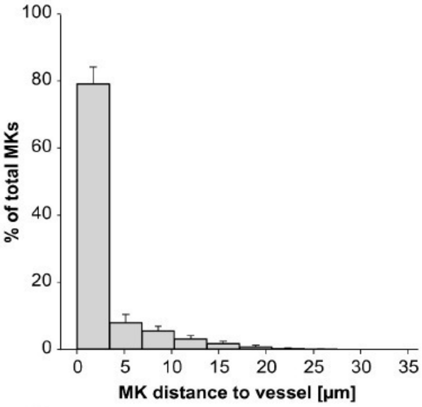

Figure 36: Localization of MKs to vessel objects (n=5 mice), bar graphs represent mean ± SD; from (Stegner, vanEeuwijk et al. 2017).

Data of MKs and vessel structures within the sternal BM support this impression. The average vessel-to-vessel distance within this research was calculated to be 43,18 ± 12,72 µm (Figure 37; (Stegner, vanEeuwijk et al. 2017)). The mean diameter of MKs on the other hand was calculated as 20,36 ± 8,19 µm (Figure 37; (Stegner, vanEeuwijk et al. 2017)). A comparison of these two figures indicates that the density of vessel structures constitutes a tight restriction on the spatial distribution of MKs within the BM. The mean diameter of two MKs accounts for vessel-to-vessel distance within the image stack and represents the constraints on spatial distribution. In accord with these findings, the statistics show that 79,3 ± 5,1% of MKs are localized with direct contact to blood vessels (Figure 36; (Stegner, vanEeuwijk et al. 2017)).

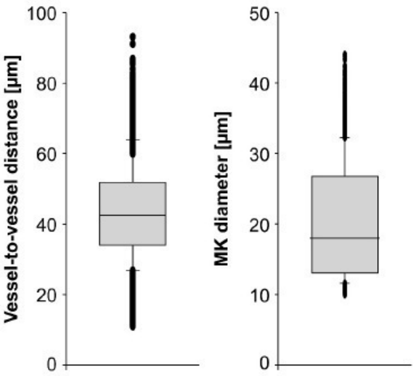

Figure 37: Limited intervascular space; vessel-to-vessel distances and average MK diameter (n=5 mice), bar graphs represent mean ± SD; from (Stegner, vanEeuwijk et al. 2017).

Furthermore, the data demonstrate that MKs are homogenously distributed throughout the vasculature within the entire BM. Five equally sized sub-stacks of the whole 3D stack confirm this hypothesis as MK parameters are almost identical within these sub-stacks (Figure 38)

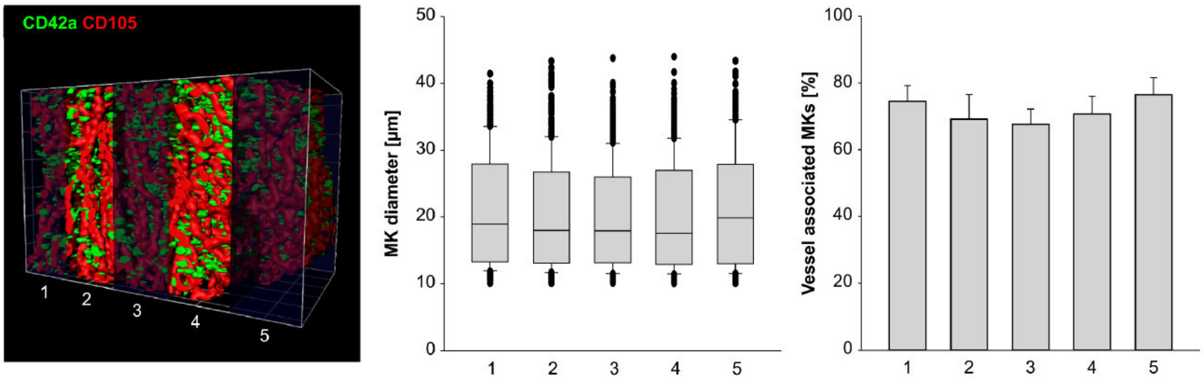

Figure 38:Distribution of MKs throughout five different sections of the reconstructed BM, bar graphs represent mean ± SD with n=5 mice, grid: 100µm; from (Stegner, vanEeuwijk et al. 2017).

supporting the hypothesis that MKs are homogenously distributed throughout the BM (Stegner, vanEeuwijk et al. 2017). Data from the sub-stacks as well as the whole images thus do not provide evidence for a tendency of MKs to locate in specific niches within the BM (Stegner, vanEeuwijk et al. 2017).

7.3. Discussion – Revised model of megakaryopoiesis

The image analysis protocol applied to images from time-series LSFM images on days 0, 1, 3, 5 and 7 showed that despite high platelet demand after depletion, the overall distribution of MKs is grossly the same as in the steady state conditions (Stegner, vanEeuwijk et al. 2017). The data provided within the time-series experiments thus clearly contradict the hypothesis of MK migration towards vessel during MK maturation (Stegner, vanEeuwijk et al. 2017). In addition to this, data from 2P-IVM-Studies (Junt, Schulze et al. 2007, Stegner, vanEeuwijk et al. 2017) indicated that MKs barely migrate within the BM. This lead to the hypothesis that MKs are randomly distributed throughout the BM and that they reach the vessel structures just by growing or random undirected movement. To evaluate this hypothesis, STEGNER ET AL. (2017) performed computer simulations of processes within the intact BM using the processed LSFM imaging data (Stegner, vanEeuwijk et al. 2017). Morphology and size of the MK as well as vessel isosurfaces served as templates for the simulations to reflect the spatial characteristics of the native environment (Stegner, vanEeuwijk et al. 2017).

The results from computer simulations as presented in STEGNER ET. AL (2017) confirm the hypothesis from the experimental data presented in section 7.2 that MKs do not migrate within the BM (Stegner, vanEeuwijk et al. 2017). Simulation results emphasize that remaining MKs without vessel contact are randomly distributed within the vessel interspace regardless of their maturation stage (Stegner, vanEeuwijk et al. 2017). This leads to the hypothesis that MKs must be replenished from progenitors in close spatial proximity to vessel structures. Furthermore, the reconstructed LSFM images demonstrate that the BM is densely vascularized. Within this dense vascular structure there is simply no space for vessel distant niches. Results from LSFM imaging as well as computational simulations performed in STEGNER ET. AL (2017) thus clearly contradict the current model of megakaryopoiesis as introduced in section 3.1.7.

In conclusion, this makes a revision of the current model of megakaryopoiesis necessary. The revised model needs to account for the absence of spatial niches within the BM. Furthermore, it should reflect the low migratory movements of MKs during maturation as they are primarily located in direct contact with the vascular system (Stegner, vanEeuwijk et al. 2017). In a revised model presented in STEGNER ET. AL (2017), MKs reside directly at the sinusoids and are replenished by precursors from this sinusoidal niche directly (Stegner, vanEeuwijk et al. 2017). This revised model is depicted in Figure 39 where the vessel interspace is densely packed with MKs from various maturation stages without the need for migratory movements during their maturation cycle. In this model MK precursors are replenished from the sinusoidal niche directly.

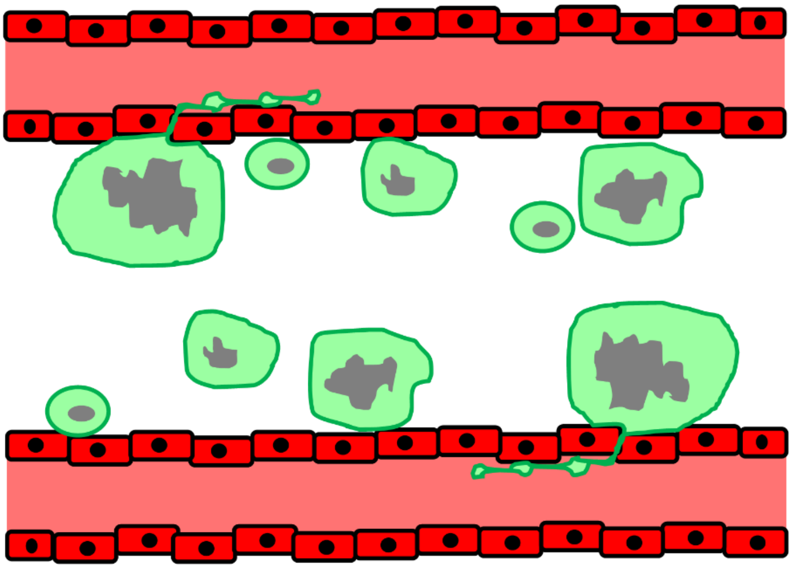

Figure 39: Revised model of megakaryopoiesis: MK precursors are replenished from the sinusoidal niche directly; adapted from (Stegner, vanEeuwijk et al. 2017).

The current model of megakaryopoiesis assumes the existence of spatial niches providing optimum conditions for various stages of maturation. It was suggested that the chemokine receptor CXCR4 and its ligand SDF1 influence the migration from the osteoblastic to the vascular niche (Avecilla, Hattori et al. 2004). Our results on the other hand do not contradict the effects of SDF1 on megakaryopoiesis but challenge the theory of its effect on MK migration. In vitro data support the current model of migrating MKs (Hamada, Mohle et al. 1998). In vitro experiments however do not manage to reflect the restriction of the extraluminal space due to the dense vascular network as identified in this study (Stegner, vanEeuwijk et al. 2017).

7.3.1. Technological limitations

A major limitation for image analysis stemmed from the limited resolution in z-direction. The characterization of the microscope revealed that the width of the light sheet is by far larger than the step-size in z (section 6.3). As discussed above this lead to a reconstructed 3D-image drawn out in the axial direction. Other studies similarly recognize the limitation of the axial resolution when imaging a single plane (Keller and Stelzer 2008). Without reduction of light sheet width, an increase in axial resolution may for example be possible by application of digital image restoration techniques such as image deconvolution without change of the imaging setup (Kundur and Hatzinakos 1996). Limited resolution in z-direction is thus a major technological limitation for LSFM imaging and subsequent image analysis at this point.

Hardware components of the image analysis setup were continuously updated. Graphics memory, random access memory (RAM), central processing unit (CPU) clock speed or disk space however constituted major constraints in image analysis. Binning was applied when gathering images for reduction of data volume (section 5.1) to account for limited disk space and limited RAM. During image analysis and processing, graphics memory and computational power in particular limited image processing (e.g. limited choice of smoothing parameters) as well as image visualization as previously described (Walter, Shattuck et al. 2010). Both Imaris® 7 and Imaris® 8 even limited the graphics memory to 8GB when performing Iso-surface segmentation. Once this limit was exceeded, Imaris® quit unexpectedly reporting “out of memory”. Advances in hardware components and hardware/software interactions may further expand the field of view of LSFM, as stitching of large data sets may become feasible.

In line with previous reports (Scholl, Aach et al. 2010), algorithms of software applied in image processing failed to utilize the full hardware potential as software components used did not manage to parallel computational processes efficiently. Furthermore, software used proved to be unstable. During image analysis, Imaris® (Imaris® 7.7.2 in particular) caused multiple unexpected Crashes so that Crash Reports such as in Figure 40 became a routinely seen undesirability abruptly causing loss of data.

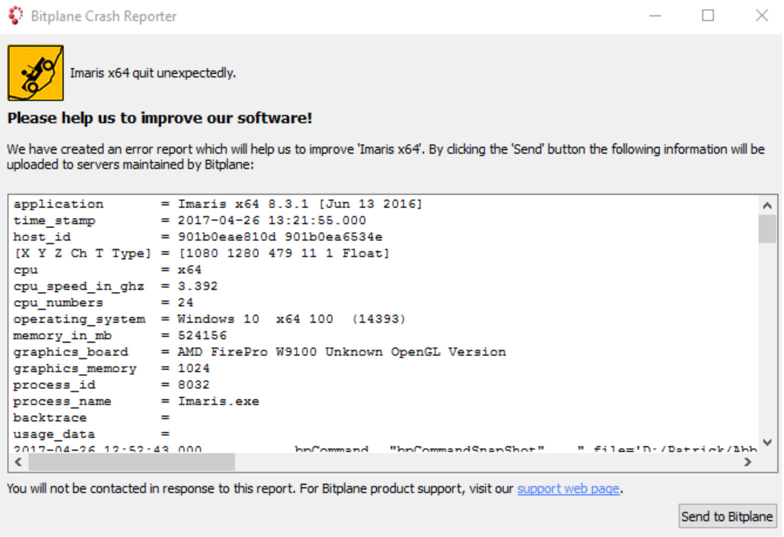

Imaris x64 quit unexpectedly.

Please help us to improve our software!

We have created an error report which will help us to improve 'Imaris x64'. By clicking the 'Send' button the following information will be uploaded to servers maintained by Bitplane:

```
application        = Imaris x64 8.3.1 [Jun 13 2016]
time_stamp         = 2017-04-26 13:21:55.000
host_id            = 901b0eae810d 901b0ea6534e
[X Y Z Ch T Type] = [1080 1280 479 11 1 Float]
cpu                = x64
cpu_speed_in_ghz   = 3.392
cpu_numbers        = 24
operating_system   = Windows 10  x64 100  (14393)
memory_in_mb       = 524156
graphics_board     = AMD FirePro W9100 Unknown OpenGL Version
graphics_memory    = 1024
process_id         = 8032
process_name       = Imaris.exe
backtrace          =
usage_data         =
```

You will not be contacted in response to this report. For Bitplane product support, visit our support web page.

Figure 40: Exemplary crash-report from Imaris® 8.3.1.

7.3.2. Methodological limitations

The pipeline for image processing used within this research proved to be effective in MK and vessel segmentation. One of the major goals of this work was comprised of elucidating MK migration during maturation. For a deeper understanding of this process, information on the relative position of MKs touching vessel structures could provide additional information on the dynamics within the bone marrow. Statistics within this research so far do not distinguish between MKs reaching into the vessel in comparison to MKs that are just located adjacent to the vessel structures. Additional statistical data could help a deeper understanding of the dynamics within the BM.

Furthermore, this research aims to improve the understanding of MK dynamics following the theory of the proplatelet model. Specimen preparation, image acquisition, image processing and statistical analysis were aimed at elucidating dynamics of MK maturation within this model. During image analysis within the present research project, we did not search for manifestation of platelet formation from the platelet territory or bust model (Albrecht 1957, Handagama, Feldman et al. 1987, Radley and Hartshorn 1987, Tong, Seth et al. 1987, Kosaki 2005, Kowata, Isogai et al. 2014, Nishimura, Nagasaki et al. 2015). Missing evidence of the latter is likely to stem from the image processing procedure applied. Platelet formation from processes such as rupture thrombopoiesis is hypothesized to result in rapid platelet provision by cytoplasmic fragmentation (Nishimura, Nagasaki et al. 2015). The proplatelets and platelets resulting from this formation method are likely to be identified in the garbage removal steps or their signal is quenched due to filter settings within the image processing pipeline. In addition, monitoring inflammatory cytokines driving MK bursting and indicating platelet formation such as IL-1 α (Nishimura, Nagasaki et al. 2015) were beyond the focus of this research.

In the course of image analysis and image processing, definition of intensity thresholds for object segmentation or binary transformation had a great effect on the resulting data. Low threshold levels resulted in a significant increase of volume of segmented objects. The choice of threshold values is inherently biased as it is part of the semi-automated image processing pipeline requiring the input from the operator. In addition to this, the definition of single intensity thresholds within the stacks for a multitude of biological structures and different cells in various locations is a compromise to capture as many structures as possible. It has been reported before, that threshold definition may lead to loss of information as it may be hard to gather information on the structure of a multitude of biological structures using single threshold values for characterization (Eils and Athale 2003). Preprocessing of the image stacks sought to reduce this effect by reducing heterogeneity such as variations in attenuation. The sequential segmentation of objects contributes in a similar way to reduce the impact of threshold definition and operator bias (e.g. sequential MK segmentation).

7.3.3. Clinical implications

As indicated in section 2.1 of this thesis, thrombocytopenia constitutes the most abundant cause of hemorrhagic diathesis (Herold 2014). Furthermore, the difficulty of treatment of such conditions was elaborated. Platelet transfusions are costly (Whitaker, Rajbhandary et al. 2016) and are associated with a high complication rate (Kruskall 1997, Kaushansky 2008). Official guidelines however primarily recommend platelet transfusions and question the efficacy of TPO treatments for hereditary thrombocytopathies and do not recommend usage of TPO (Streif, Eberl et al. 2014). In line with this, KAUSHANSKY AND DRACHMAN 2002 scrutinize the effect of TPO on thrombocytopenia and emphasize the development of neutralizing antibodies with native TPO (Kaushansky and Drachman 2002).

For development of new therapeutic strategies for thrombocytopenia, a deeper understanding of the process of megakaryopoiesis and platelet formation is required. Following the current concept of megakaryopoiesis as introduced in section 3.1.7., increasing the migratory movements of MKs from the osteoblastic to the vascular niche might constitute the basis for development of new therapeutic strategies. The revised model of megakaryopoiesis introduced in STEGNER ET AL. (2017) however indicates, that this strategy might be limited in its effect. It is hypothesized that MKs are replenished from precursors originating from the sinusoidal niche (Stegner, vanEeuwijk et al. 2017). In line with this data, an increase in migratory movements of MKs might fail to realize a significant increase in platelet production, as the majority of MKs is already vessel associated (Figure 36 and Figure 38). Increasing MK turnover rather than its migratory movements might thus be a starting point for development of new therapeutic strategies. This is in line with findings of AVECILLA ET AL (2004), who demonstrate that SDF-1 only increases platelet production in presence of bone marrow endothelial cells (Avecilla, Hattori et al. 2004). Due to a missing osteoblastic niche in our revised model, evidence for the hypothesis that SDF-1 or FGF-4 increase migratory movements ((Nagasawa, Hirota et al. 1996, Hamada, Mohle et al. 1998), section 3.1.7) is however missing. The effect of TPO on restoring platelet levels (section 3.1.3) may similarly be explained by its effect on MKs and its progenitors near vessel structures within the vascular niche.

For development of new therapeutic strategies, the revised model of megakaryopoiesis thus needs to be considered. As MKs are already mainly colocalized with vessel structures, the effect of increasing their migratory movements towards vessel may be limited. Raising numbers of MKs or accelerating their maturation process might thus be sufficient for raising platelet levels and treatment of thrombocytopenia. The revised model of megakaryopoiesis might furthermore be applied to the concept of HSC differentiation. The dense vasculature of specimen analyzed similarly constraints the existence of potential quiescent niches (section 3.1.6) spatially.

7.4. Perspective and implications from limitations

Despite basic principles being introduced already more than a century ago (section 3), mechanisms of platelet production and megakaryopoiesis are still under investigation. This thesis in particular emphasizes the dependence of research within the field of biomedicine from technological advances. In extreme terms it could be theorized that work within this thesis would be negligible, if better image acquisition and image analysis protocols in line with sufficient hardware resources would be available. This work is focused on overcoming specific challenges primarily arising from insufficiencies in clearing, imaging and object segmentation (section 6). Approaches and pipelines developed constitute compromises for image processing realizing a transition from specimen preparation and imaging to quantitative statistical evaluation and simulation. This compromise was developed in the sense of the best possible output under given technological and methodological constraints to my best knowledge.

Machine learning and computer vision

The field of computer vision and software development play crucial roles in enabling advances in digital image processing. Ultimately, a semi-automated or automated image analysis algorithm would be desirable, that reduces biased user input to a minimum. On the way to this “future algorithm” potentially performed by artificial intelligence using technologies such as machine learning or deep learning, software tools need to be optimized so that current processes can be performed without disruptions (software crash). Machine learning offers possibilities of reducing necessary user input and provides opportunities in processing large amounts of imaging data. Processes need to be parallelizable to harness existing hardware resources and tools need to be developed to account for problems arising with Big Data and data storage (section 3.3.1). Recent updates of software used such as Imaris® 7.7.2 / 8.3.1 (Bitplane AG, Zürich, Switzerland) already improved parallelization of processes from Imaris® 9.0.0 (Bitplane AG, Zürich, Switzerland) on. Furthermore, processing methods such as image deconvolution offer further optimization potential of image quality by reducing the distortion created by the optical system (Sarder and Nehorai 2006). Image deconvolution mitigates this distortion by incorporation of the characteristics of the optical system expressed in the point spread function of the specific setup (McNally, Karpova et al. 1999).

Hardware requirements

Similarly, hardware components restrain advances in the field of imaging in biomedicine. Large amounts of data not only require storage capabilities, but also exhaust computer and graphics memory to their limits. Besides development of efficient software tools for handling such large data volumes, advances in hardware development likewise contribute to advances in image analysis. In this context the limited RAM and graphics memory particularly restricted computational image processing and processing speed. Lifting the binning of data within this project would for example instantly increase data volume fourfold (binning 2x in x and in y direction, section 5.1) exceeding the limits of the image processing setup used here (section 5.1). Within Imaris® 7.7.2 / 8.3.1 (Bitplane AG, Zürich, Switzerland), only data for cell-objects was partly transferrable to the main memory thus reducing the load of RAM. With application of additional steps in image processing such as image deconvolution, the limitation of computational resources is aggravated.

Continuous improvement of the microscope hardware in the same way contributes to an increase of image analysis performance. Higher resolution in all three dimensions allows for a more detailed analysis of structures of interest. As discussed above (section 6.3), the axial resolution particularly hampers the improvement of image quality. Among other factors, it is highly determined by the thickness of the illuminating light sheet. This limitation for modern applications in biology has also been reported previously (Swoger, Verveer et al. 2007, Keller and Stelzer 2008). Strategies for overcoming this limitation in LSFM include Multi-view image fusion, in which LSFM images are captured from multiple viewing directions reducing anisotropic resolution and the effect of partially transparent samples (Swoger, Verveer et al. 2007). In a similar way introducing illumination from another angle perpendicular to the detection axis might lead to increased axial resolution and reduce low-frequency intensity variations stemming from partially opaque regions within the specimen. Other studies suggest the adoption of a tunable lens within the illumination beam to create a thin light sheet by sweeping the focal plane along the x-axis and capturing the image vertically to the illumination axis (y-direction) in a scanned fashion for each individual plane (Zong, Zhao et al. 2014). Furthermore, it has been suggested to use Bessel-beams (Gao, Shao et al. 2012) or Airy-beams in combination with computational deconvolution (Vettenburg, Dalgarno et al. 2014) in LSFM for creation of a thin light sheet and to increase contrast and resolution.

Necessity of combined technological advances

These perspectives only portray individual solution approaches and do not claim to be complete. As discussed in section 3, technological advances in imaging technology, optical clearing, computer hard- and software as well as data storage and processing for the first time allowed imaging of intact bone in this combination. However, major challenges remain. They limit the applicability of the technology used and challenge the overall acceptance of the results. These limitations however offer starting points for further research. For overcoming these technological and methodological limitations, combined efforts in the affected technological fields are necessary to avoid non-contiguous outcome and to gain further insights in MK maturation as well as involved areas of research.

VI. Bibliography

Acar, M., K. S. Kocherlakota, M. M. Murphy, J. G. Peyer, H. Oguro, C. N. Inra, C. Jaiyeola, Z. Zhao, K. Luby-Phelps and S. J. Morrison (2015). "Deep imaging of bone marrow shows non-dividing stem cells are mainly perisinusoidal." Nature **526**(7571): 126-130.

Albrecht, M. (1957). "Studien zur Thrombocytenbildung an Megakaryocyten in menschlichen Knochenmarkkulturen." Acta Haematologica **17**(3): 160-168.

Arce, G. R., J. L. Paredes and J. Mullan (2000). Nonlinear Filtering for Image Analysis and Enhancement. Handbook of Image and Video Processing. D. G. Jerry and B. Al, Academic Press, Inc.**:** pp 81-100

Avecilla, S. T., K. Hattori, B. Heissig, R. Tejada, F. Liao, K. Shido, D. K. Jin, S. Dias, F. Zhang, T. E. Hartman, N. R. Hackett, R. G. Crystal, L. Witte, D. J. Hicklin, P. Bohlen, D. Eaton, D. Lyden, F. de Sauvage and S. Rafii (2004). "Chemokine-mediated interaction of hematopoietic progenitors with the bone marrow vascular niche is required for thrombopoiesis." Nat Med **10**(1): 64-71.

Becker, K., N. Jährling, S. Saghafi, R. Weiler and H.-U. Dodt (2012). "Chemical Clearing and Dehydration of GFP Expressing Mouse Brains." PLOS ONE **7**(3): e33916.

Behnke, O. (1969). "An electron microscope study of the rat megacaryocyte." Journal of Ultrastructure Research **26**(1): 111-129.

Behrends, J. C., J. Bischofberger, R. Deutzmann, H. Ehmke, S. Frings, S. Grissmer, M. Hoth, A. Kurtz, J. Leipziger, F. Müller, C. Pedain, J. Rettig, C. Wagner and E. Wischmeyer (2012). Physiologie. Stuttgart, New York, Georg Thieme Verlag.

Bender, M., S. Stritt, P. Nurden, J. M. M. van Eeuwijk, B. Zieger, K. Kentouche, H. Schulze, H. Morbach, D. Stegner, K. G. Heinze, S. Dütting, S. Gupta, W. Witke, H. Falet, A. Fischer, J. H. Hartwig and B. Nieswandt (2014). "Megakaryocyte-specific Profilin1-deficiency alters microtubule stability and causes a Wiskott–Aldrich syndrome-like platelet defect." Nat Commun **5**: 4746.

Bitplane (2013). ReferenceManual 7.6.0. Zuerich, Switzerland, Bitplane AG.

Bluteau, D., L. Lordier, A. Di Stefano, Y. Chang, H. Raslova, N. Debili and W. Vainchenker (2009). "Regulation of megakaryocyte maturation and platelet formation." J Thromb Haemost **7 Suppl 1**: 227-234.

Bluteau, O., T. Langlois, P. Rivera-Munoz, F. Favale, P. Rameau, G. Meurice, P. Dessen, E. Solary, H. Raslova, T. Mercher, N. Debili and W. Vainchenker (2013).

"Developmental changes in human megakaryopoiesis." J Thromb Haemost **11**(9): 1730-1741.

Böck, M. (2015, 03.06.2015). "Herstellung / Indikation von Thrombozytenkonzentraten (TKs)." Hauptvorlesung Transfusionsmedizin Retrieved 25.05.2018, 2018, from http://www.transfusionsmedizin.ukw.de/studenten/hauptvorlesung/herstellung-indikation-tks/lagerung-transport.html.

Bootsma, G. J. and G. W. Brodland (2005). "Automated 3-D reconstruction of the surface of live early-stage amphibian embryos." IEEE Trans Biomed Eng **52**(8): 1407-1414.

Brede, C., M. Friedrich, A. L. Jordan-Garrote, S. S. Riedel, C. A. Bauerlein, K. G. Heinze, T. Bopp, S. Schulz, A. Mottok, C. Kiesel, K. Mattenheimer, M. Ritz, V. von Krosigk, A. Rosenwald, H. Einsele, R. S. Negrin, G. S. Harms and A. Beilhack (2012). "Mapping immune processes in intact tissues at cellular resolution." J Clin Invest **122**(12): 4439-4446.

Buades, A., B. Coll and J. M. Morel (2005). A non-local algorithm for image denoising. 2005 IEEE Computer Society Conference on Computer Vision and Pattern Recognition (CVPR'05).

Buggenthin, F., C. Marr, M. Schwarzfischer, P. S. Hoppe, O. Hilsenbeck, T. Schroeder and F. J. Theis (2013). "An automatic method for robust and fast cell detection in bright field images from high-throughput microscopy." BMC Bioinformatics **14**: 297.

Calvi, L. M., G. B. Adams, K. W. Weibrecht, J. M. Weber, D. P. Olson, M. C. Knight, R. P. Martin, E. Schipani, P. Divieti, F. R. Bringhurst, L. A. Milner, H. M. Kronenberg and D. T. Scadden (2003). "Osteoblastic cells regulate the haematopoietic stem cell niche." Nature **425**(6960): 841-846.

Canny, J. (1986). "A computational approach to edge detection." IEEE Trans Pattern Anal Mach Intell **8**(6): 679-698.

Cardona, A. and P. Tomancak (2012). "Current challenges in open-source bioimage informatics." Nat Methods **9**(7): 661-665.

Chang, Y., D. Bluteau, N. Debili and W. Vainchenker (2007). "From hematopoietic stem cells to platelets." Journal of Thrombosis and Haemostasis **5 Suppl 1**: 318-327.

Chen, H., J. R. Swedlow, M. Grote, J. W. Sedat and D. A. Agard (1995). The collection, processing, and display of digital three-dimensional images of biological specimens. Handbook of Biological Confocal Microscopy. J. B. Pawley. NY, Plenum Press: 197-210.

Chung, K. and K. Deisseroth (2013). "CLARITY for mapping the nervous system." Nat Methods **10**(6): 508-513.

Cline, H. E., W. E. Lorensen, S. Ludke, C. R. Crawford and B. C. Teeter (1988). "Two algorithms for the three-dimensional reconstruction of tomograms." Med Phys **15**(3): 320-327.

Cramer, E. M., F. Norol, J. Guichard, J. Breton-Gorius, W. Vainchenker, J.-M. Massé and N. Debili (1997). "Ultrastructure of Platelet Formation by Human Megakaryocytes Cultured With the Mpl Ligand." Blood **89**(7): 2336-2346.

Day, R. B. and D. C. Link (2014). "Megakaryocytes in the hematopoietic stem cell niche." Nat Med **20**(11): 1233-1234.

Deng, G. and L. W. Cahill (1993). An adaptive Gaussian filter for noise reduction and edge detection. 1993 IEEE Conference Record Nuclear Science Symposium and Medical Imaging Conference.

Dodt, H. U., U. Leischner, A. Schierloh, N. Jahrling, C. P. Mauch, K. Deininger, J. M. Deussing, M. Eder, W. Zieglgansberger and K. Becker (2007). "Ultramicroscopy: three-dimensional visualization of neuronal networks in the whole mouse brain." Nat Methods **4**(4): 331-336.

Dorn, J. F., G. Danuser and G. Yang (2008). "Computational processing and analysis of dynamic fluorescence image data." Methods Cell Biol **85**: 497-538.

Eils, R. and C. Athale (2003). "Computational imaging in cell biology." The Journal of Cell Biology **161**(3): 477.

Eliasson, P. and J. I. Jonsson (2010). "The hematopoietic stem cell niche: low in oxygen but a nice place to be." J Cell Physiol **222**(1): 17-22.

Erturk, A., K. Becker, N. Jahrling, C. P. Mauch, C. D. Hojer, J. G. Egen, F. Hellal, F. Bradke, M. Sheng and H. U. Dodt (2012). "Three-dimensional imaging of solvent-cleared organs using 3DISCO." Nat Protoc **7**(11): 1983-1995.

Ferreira, T. and W. Rasband (2012). ImageJ User Guide IJ 1.46r.

Fisher, R., S. Perkins, A. Walker and E. Wolfart. (2003). "Unsharp Filter - Hypermedia Image Processing Reference (HIPR2)." Hypermedia Image Processing Reference (HIPR2) Retrieved 31.05.2018, 2018, from http://homepages.inf.ed.ac.uk/rbf/HIPR2/unsharp.htm.

Gao, L., L. Shao, C. D. Higgins, J. S. Poulton, M. Peifer, M. W. Davidson, X. Wu, B. Goldstein and E. Betzig (2012). "Noninvasive imaging beyond the diffraction limit of 3D dynamics in thickly fluorescent specimens." Cell **151**(6): 1370-1385.

Garraud, O., F. Cognasse, J. D. Tissot, P. Chavarin, S. Laperche, P. Morel, J. J. Lefrere, B. Pozzetto, M. Lozano, N. Blumberg and J. C. Osselaer (2016). "Improving platelet transfusion safety: biomedical and technical considerations." Blood Transfus **14**(2): 109-122.

Geddis, A. E., N. E. Fox, E. Tkachenko and K. Kaushansky (2007). "Endomitotic Megakaryocytes that Form a Bipolar Spindle Exhibit Cleavage Furrow Ingression Followed by Furrow Regression." Cell Cycle **6**(4): 455-460.

Grozovsky, R., A. J. Begonja, K. Liu, G. Visner, J. H. Hartwig, H. Falet and K. M. Hoffmeister (2015). "The Ashwell-Morell receptor regulates hepatic thrombopoietin production via JAK2-STAT3 signaling." Nat Med **21**(1): 47-54.

Grozovsky, R., S. Giannini, H. Falet and K. M. Hoffmeister (2015). "Regulating billions of blood platelets: glycans and beyond." Blood.

Guo, T., X. Wang, Y. Qu, Y. Yin, T. Jing and Q. Zhang (2015). "Megakaryopoiesis and platelet production: insight into hematopoietic stem cell proliferation and differentiation." Stem Cell Investigation **2**: 3.

Gurney, A. L., K. Carver-Moore, F. J. de Sauvage and M. W. Moore (1994). "Thrombocytopenia in c-mpl-deficient mice." Science **265**(5177): 1445-1447.

Hama, H., H. Kurokawa, H. Kawano, R. Ando, T. Shimogori, H. Noda, K. Fukami, A. Sakaue-Sawano and A. Miyawaki (2011). "Scale: a chemical approach for fluorescence imaging and reconstruction of transparent mouse brain." Nat Neurosci **14**(11): 1481-1488.

Hamada, T., R. Mohle, J. Hesselgesser, J. Hoxie, R. L. Nachman, M. A. Moore and S. Rafii (1998). "Transendothelial migration of megakaryocytes in response to stromal cell-derived factor 1 (SDF-1) enhances platelet formation." J Exp Med **188**(3): 539-548.

Handagama, P. J., B. F. Feldman, N. C. Jain, T. B. Farver and C. S. Kono (1987). "Circulating proplatelets: isolation and quantitation in healthy rats and in rats with induced acute blood loss." Am J Vet Res **48**(6): 962-965.

He, N., L. Zhang, J. Cui and Z. Li (2014). "Bone marrow vascular niche: home for hematopoietic stem cells." Bone Marrow Res **2014**: 128436.

Helmchen, F. and W. Denk (2005). "Deep tissue two-photon microscopy." Nat Methods **2**(12): 932-940.

Herold, G. u. M. (2014). Innere Medizin. Köln, Herold.

Hornick, J. E. and E. H. Hinchcliffe (2015). "It's all about the pentiums: The use, manipulation, and storage of digital microscopy imaging data for the biological sciences." Molecular Reproduction and Development **82**(7-8): 508-517.

Huisken, J. and D. Y. Stainier (2009). "Selective plane illumination microscopy techniques in developmental biology." Development **136**(12): 1963-1975.

Huisken, J., J. Swoger, F. Del Bene, J. Wittbrodt and E. H. Stelzer (2004). "Optical sectioning deep inside live embryos by selective plane illumination microscopy." Science **305**(5686): 1007-1009.

Italiano, J. (2008). "The structure and production of blood platelets." Platelets in Hematologic and Cardiovascular Disorders-A Clinical Handbook. Gresele, P: 1-20.

Italiano, J. E., Jr. (2013). "Unraveling mechanisms that control platelet production." Semin Thromb Hemost **39**(1): 15-24.

Italiano, J. E., Jr., P. Lecine, R. A. Shivdasani and J. H. Hartwig (1999). "Blood platelets are assembled principally at the ends of proplatelet processes produced by differentiated megakaryocytes." J Cell Biol **147**(6): 1299-1312.

Ito, T., Y. Ishida, R. Kashiwagi and S.-I. Kuriya (1996). "Recombinant human c-Mpl ligand is not a direct stimulator of proplatelet formation in mature human megakaryocytes." British Journal of Haematology **94**(2): 387-390.

Jayaraman, S., S. Esakkirajan and T. Veerakumar (2009). Digital Image Processing Tata McGraw Hill Education.

Junt, T., H. Schulze, Z. Chen, S. Massberg, T. Goerge, A. Krueger, D. D. Wagner, T. Graf, J. E. Italiano, Jr., R. A. Shivdasani and U. H. von Andrian (2007). "Dynamic visualization of thrombopoiesis within bone marrow." Science **317**(5845): 1767-1770.

Kaushansky, K. (2008). "Historical review: megakaryopoiesis and thrombopoiesis." Blood **111**(3): 981-986.

Kaushansky, K. and J. G. Drachman (2002). "The molecular and cellular biology of thrombopoietin: the primary regulator of platelet production." Oncogene **21**(21): 3359-3367.

Ke, M. T., S. Fujimoto and T. Imai (2013). "SeeDB: a simple and morphology-preserving optical clearing agent for neuronal circuit reconstruction." Nat Neurosci **16**(8): 1154-1161.

Keller, P. J. and E. H. K. Stelzer (2008). "Quantitative in vivo imaging of entire embryos with Digital Scanned Laser Light Sheet Fluorescence Microscopy." Current Opinion in Neurobiology **18**(6): 624-632.

Kiefel, V. (2008). "Reactions Induced by Platelet Transfusions." Transfus Med Hemother **35**(5): 354-358.

Kile, B. T. (2015). "Aging platelets stimulate TPO production." Nat Med **21**(1): 11-12.

Klauschen, F., H. Qi, J. G. Egen, R. N. Germain and M. Meier-Schellersheim (2009). "Computational reconstruction of cell and tissue surfaces for modeling and data analysis." Nat Protoc **4**(7): 1006-1012.

Koller, T., G. Gerig, G. Szekely and D. Dettwiler (1995). Multiscale detection ofcurvilinear structure in 2-D and 3-D image data. Fifth International Conference on Computer Vision ICCV'95, Cambridge, MA, IEEE Computer Society Press.

Kosaki, G. (2005). "In Vivo Platelet Production from Mature Megakaryocytes: Does Platelet Release Occur via Proplatelets?" International Journal of Hematology **81**(3): 208-219.

Kowata, S., S. Isogai, K. Murai, S. Ito, K. Tohyama, M. Ema, J. Hitomi and Y. Ishida (2014). "Platelet demand modulates the type of intravascular protrusion of megakaryocytes in bone marrow." Thromb Haemost **112**(4): 743-756.

Kruskall, M. S. (1997). "The perils of platelet transfusions." New England Journal of Medicine **337**(26): 1914-1915.

Kundur, D. and D. Hatzinakos (1996). "Blind image deconvolution." IEEE Signal Processing Magazine **13**(3): 43-64.

Kunisaki, Y., I. Bruns, C. Scheiermann, J. Ahmed, S. Pinho, D. Zhang, T. Mizoguchi, Q. Wei, D. Lucas, K. Ito, J. C. Mar, A. Bergman and P. S. Frenette (2013). "Arteriolar niches maintain haematopoietic stem cell quiescence." Nature **502**(7473): 637-643.

Landhuis, E. (2017). "Neuroscience: Big brain, big data." Nature **541**(7638): 559-561.

Langer, S. G. (2011). "Challenges for Data Storage in Medical Imaging Research." Journal of Digital Imaging **24**(2): 203-207.

Larson, M. K. and S. P. Watson (2006). "A product of their environment: do megakaryocytes rely on extracellular cues for proplatelet formation?" Platelets **17**(7): 435-440.

Lorensen, W. E. and H. E. Cline (1987). "Marching cubes: A high resolution 3D surface construction algorithm." ACM SIGGRAPH Computer Graphics **21**(4): 163-169.

Lucas, L. F. R., N. M. M. Rodrigues, L. A. da Silva Cruz and S. M. M. de Faria (2017). "Lossless Compression of Medical Images Using 3-D Predictors." IEEE Trans Med Imaging **36**(11): 2250-2260.

Lüllmann-Rauch, R. (2012). Taschenlehrbuch Histologie : 10 Tabellen. Stuttgart ; New York, NY, Thieme

Machlus, K. R. and J. E. Italiano, Jr. (2013). "The incredible journey: From megakaryocyte development to platelet formation." J Cell Biol **201**(6): 785-796.

Machlus, K. R., J. N. Thon and J. E. Italiano, Jr. (2014). "Interpreting the developmental dance of the megakaryocyte: a review of the cellular and molecular processes mediating platelet formation." Br J Haematol **165**(2): 227-236.

Malara, A., V. Abbonante, C. A. Di Buduo, L. Tozzi, M. Currao and A. Balduini (2015). "The secret life of a megakaryocyte: emerging roles in bone marrow homeostasis control." Cell Mol Life Sci **72**(8): 1517-1536.

McNally, J. G., T. Karpova, J. Cooper and J. A. Conchello (1999). "Three-dimensional imaging by deconvolution microscopy." Methods **19**(3): 373-385.

Mohyeldin, A., T. Garzon-Muvdi and A. Quinones-Hinojosa (2010). "Oxygen in stem cell biology: a critical component of the stem cell niche." Cell Stem Cell **7**(2): 150-161.

Moore, J., C. Allan, J. M. Burel, B. Loranger, D. MacDonald, J. Monk and J. R. Swedlow (2008). "Open tools for storage and management of quantitative image data." Methods Cell Biol **85**: 555-570.

Nagasawa, T., S. Hirota, K. Tachibana, N. Takakura, S. Nishikawa, Y. Kitamura, N. Yoshida, H. Kikutani and T. Kishimoto (1996). "Defects of B-cell lymphopoiesis and bone-marrow myelopoiesis in mice lacking the CXC chemokine PBSF/SDF-1." Nature **382**(6592): 635-638.

Navjeet, K., D. Punetha and F. Ehiagwina (2016). "Preserving the Edges of a Digital Image Using Various Filtering Algorithms and Tools." International Journal of Signal Processing, Image Processing and Pattern Recognition **9**(12): 11-18.

Nilsson, S. K., M. E. Debatis, M. S. Dooner, J. A. Madri, P. J. Quesenberry and P. S. Becker (1998). "Immunofluorescence characterization of key extracellular matrix proteins in murine bone marrow in situ." J Histochem Cytochem **46**(3): 371-377.

Nishimura, S., M. Nagasaki, S. Kunishima, A. Sawaguchi, A. Sakata, H. Sakaguchi, T. Ohmori, I. Manabe, J. E. Italiano, Jr., T. Ryu, N. Takayama, I. Komuro, T. Kadowaki, K. Eto and R. Nagai (2015). "IL-1alpha induces thrombopoiesis through megakaryocyte rupture in response to acute platelet needs." J Cell Biol **209**(3): 453-466.

Nombela-Arrieta, C., G. Pivarnik, B. Winkel, K. J. Canty, B. Harley, J. E. Mahoney, S. Y. Park, J. Lu, A. Protopopov and L. E. Silberstein (2013). "Quantitative imaging of haematopoietic stem and progenitor cell localization and hypoxic status in the bone marrow microenvironment." Nat Cell Biol **15**(5): 533-543.

Ntziachristos, V. (2010). "Going deeper than microscopy: the optical imaging frontier in biology." Nat Meth **7**(8): 603-614.

Paddock, S. W. (2000). "Principles and practices of laser scanning confocal microscopy." Molecular Biotechnology **16**(2): 127-149.

Pallotta, I., M. Lovett, W. Rice, D. L. Kaplan and A. Balduini (2009). "Bone marrow osteoblastic niche: a new model to study physiological regulation of megakaryopoiesis." PLoS One **4**(12): e8359.

Parmar, K., P. Mauch, J. A. Vergilio, R. Sackstein and J. D. Down (2007). "Distribution of hematopoietic stem cells in the bone marrow according to regional hypoxia." Proc Natl Acad Sci U S A **104**(13): 5431-5436.

Patel, S. R., J. H. Hartwig and J. E. Italiano, Jr. (2005). "The biogenesis of platelets from megakaryocyte proplatelets." J Clin Invest **115**(12): 3348-3354.

Peng, H., J. Zhou, Z. Zhou, A. Bria, Y. Li, D. M. Kleissas, N. G. Drenkow, B. Long, X. Liu and H. Chen (2016). Bioimage Informatics for Big Data. Focus on Bio-Image Informatics. W. H. De Vos, S. Munck and J.-P. Timmermans. Cham, Springer International Publishing**:** 263-272.

Periayah, M. H., A. S. Halim and A. Z. Mat Saad (2017). "Mechanism Action of Platelets and Crucial Blood Coagulation Pathways in Hemostasis." International Journal of Hematology-Oncology and Stem Cell Research **11**(4): 319-327.

Pschyrembel, W. (2007). Pschyrembel Klinisches Wörterbuch Berlin ; New York: de Gruyter

Radley, J. M. and C. J. Haller (1982). "The demarcation membrane system of the megakaryocyte: a misnomer?" Blood **60**(1): 213-219.

Radley, J. M. and M. A. Hartshorn (1987). "Megakaryocyte fragments and the microtubule coil." Blood Cells **12**(3): 603-614.

Rasband, W. (2000, 09.02.2004). "Particle Remover Plugin." from https://imagej.nih.gov/ij/plugins/particle-remover.html.

Reddi, A. H., R. Gay, S. Gay and E. J. Miller (1977). "Transitions in collagen types during matrix-induced cartilage, bone, and bone marrow formation." Proc Natl Acad Sci U S A **74**(12): 5589-5592.

Richardson, J. L., R. A. Shivdasani, C. Boers, J. H. Hartwig and J. E. Italiano (2005). "Mechanisms of organelle transport and capture along proplatelets during platelet production." Blood **106**(13): 4066-4075.

Sabri, S., M. Jandrot-Perrus, J. Bertoglio, R. W. Farndale, V. M.-D. Mas, N. Debili and W. Vainchenker (2004). "Differential regulation of actin stress fiber assembly and proplatelet formation by alpha2beta1 integrin and GPVI in human megakaryocytes." Blood **104**(10): 3117-3125.

Santi, P. A. (2011). "Light Sheet Fluorescence Microscopy: A Review." Journal of Histochemistry and Cytochemistry **59**(2): 129-138.

Sarder, P. and A. Nehorai (2006). "Deconvolution methods for 3-D fluorescence microscopy images." IEEE Signal Processing Magazine **23**(3): 32-45.

Schindelin, J., I. Arganda-Carreras, E. Frise, V. Kaynig, M. Longair, T. Pietzsch, S. Preibisch, C. Rueden, S. Saalfeld, B. Schmid, J.-Y. Tinevez, D. J. White, V. Hartenstein, K. Eliceiri, P. Tomancak and A. Cardona (2012). "Fiji: an open-source platform for biological-image analysis." Nat Meth **9**(7): 676-682.

Schindelin, J., C. T. Rueden, M. C. Hiner and K. W. Eliceiri (2015). "The ImageJ ecosystem: An open platform for biomedical image analysis." Mol Reprod Dev **82**(7-8): 518-529.

Schneider, C. A., W. S. Rasband and K. W. Eliceiri (2012). "NIH Image to ImageJ: 25 years of image analysis." Nat Meth **9**(7): 671-675.

Schofield, R. (1978). "The relationship between the spleen colony-forming cell and the haemopoietic stem cell." Blood Cells **4**(1-2): 7-25.

Scholl, I., T. Aach, T. M. Deserno and T. Kuhlen (2010). "Challenges of medical image processing." Computer Science - Research and Development **26**(1-2): 5-13.

Schulze, H., M. Korpal, J. Hurov, S. W. Kim, J. Zhang, L. C. Cantley, T. Graf and R. A. Shivdasani (2006). "Characterization of the megakaryocyte demarcation membrane system and its role in thrombopoiesis." Blood **107**(10): 3868-3875.

SFB688. (2018, 20.05.2018). "Ziele des SFB 688." Retrieved 25.05.2018, 2018, from http://www.sfb688.uni-wuerzburg.de/ziele/.

Siedentopf, H. and R. Zsigmondy (1903). "Über Sichtbarmachung und Größenbestimmung ultramikroskopischer Teilchen mit besonderer Anwendung auf Rubingläser." Annalen der Physik(10): 1-39.

Stegner, D., J. M. M. vanEeuwijk, O. Angay, M. G. Gorelashvili, D. Semeniak, J. Pinnecker, P. Schmithausen, I. Meyer, M. Friedrich, S. Dütting, C. Brede, A. Beilhack, H. Schulze, B. Nieswandt and K. G. Heinze (2017). "Thrombopoiesis is spatially regulated by the bone marrow vasculature." Nature Communications **8**(1): 127.

Sternberg, S. R. (1983). "Biomedical Image Processing." Computer **16**(1): 22-34.

Streif, W., W. Eberl and R. Knöfler (2014). Leitlinie-Thrombozytopathien Therapie (angeborene Störungen der Thrombozytenfunktion bei Kindern und Jugendlichen). AWMF Register Nr. 086-004, Klasse: S2K. http://www.awmf.org/uploads/tx_szleitlinien/086-

004I_S2k_Thrombozytopathien_Therapie_2014-04.pdf, Arbeitsgemeinschaft der Wissenschaftlichen Medizinischen Fachgesellschaften e.V.

Susaki, E. A., K. Tainaka, D. Perrin, F. Kishino, T. Tawara, T. M. Watanabe, C. Yokoyama, H. Onoe, M. Eguchi, S. Yamaguchi, T. Abe, H. Kiyonari, Y. Shimizu, A. Miyawaki, H. Yokota and H. R. Ueda (2014). "Whole-brain imaging with single-cell resolution using chemical cocktails and computational analysis." Cell **157**(3): 726-739.

Susaki, E. A., K. Tainaka, D. Perrin, H. Yukinaga, A. Kuno and H. R. Ueda (2015). "Advanced CUBIC protocols for whole-brain and whole-body clearing and imaging." Nat. Protocols **10**(11): 1709-1727.

Svoboda, K. and R. Yasuda (2006). "Principles of two-photon excitation microscopy and its applications to neuroscience." Neuron **50**(6): 823-839.

Swedlow, J. R., I. Goldberg, E. Brauner and P. K. Sorger (2003). "Informatics and Quantitative Analysis in Biological Imaging." Science **300**(5616): 100.

Swedlow, J. R., I. G. Goldberg and K. W. Eliceiri (2009). "Bioimage informatics for experimental biology." Annu Rev Biophys **38**: 327-346.

Swoger, J., P. Verveer, K. Greger, J. Huisken and E. H. K. Stelzer (2007). "Multi-view image fusion improves resolution in three-dimensional microscopy." Optics Express **15**(13): 8029-8042.

Tablin, F., M. Castro and R. M. Leven (1990). "Blood platelet formation in vitro. The role of the cytoskeleton in megakaryocyte fragmentation." J Cell Sci **97 (Pt 1)**(1): 59-70.

Tania, S. and R. Rowaida (2016). "A Comparative Study of Various Image Filtering Techniques for Removing Various Noisy Pixels in Aerial Image." International Journal of Signal Processing, Image Processing and Pattern Recognition **9**(3): 113-124.

Theer, P., M. T. Hasan and W. Denk (2003). "Two-photon imaging to a depth of 1000 µm in living brains by use of a Ti:Al_2O_3 regenerative amplifier." Optics Letters **28**(12): 1022-1024.

Thon, J. N., A. Montalvo, S. Patel-Hett, M. T. Devine, J. L. Richardson, A. Ehrlicher, M. K. Larson, K. Hoffmeister, J. H. Hartwig and J. E. Italiano, Jr. (2010). "Cytoskeletal mechanics of proplatelet maturation and platelet release." J Cell Biol **191**(4): 861-874.

Tong, M., P. Seth and D. G. Penington (1987). "Proplatelets and stress platelets." Blood **69**(2): 522-528.

Tozawa, K., Y. Ono-Uruga and Y. Matsubara (2014). "Megakaryopoiesis." Clinical & Experimental Thrombosis and Hemostasis **1**(2): 54-58.

Vettenburg, T., H. I. C. Dalgarno, J. Nylk, C. Coll-Lladó, D. E. K. Ferrier, T. Čižmár, F. J. Gunn-Moore and K. Dholakia (2014). "Light-sheet microscopy using an Airy beam." Nature Methods **11**: 541.

Voie, A. H. (2002). "Imaging the intact guinea pig tympanic bulla by orthogonal-plane fluorescence optical sectioning microscopy." Hear Res **171**(1-2): 119-128.

Voie, A. H., D. H. Burns and F. A. Spelman (1993). "Orthogonal-plane fluorescence optical sectioning: three-dimensional imaging of macroscopic biological specimens." J Microsc **170**(Pt 3): 229-236.

Walter, T., D. W. Shattuck, R. Baldock, M. E. Bastin, A. E. Carpenter, S. Duce, J. Ellenberg, A. Fraser, N. Hamilton, S. Pieper, M. A. Ragan, J. E. Schneider, P. Tomancak and J.-K. Hériché (2010). "Visualization of image data from cells to organisms." Nature Methods **7**(3 Suppl): S26.

Whitaker, B., S. Rajbhandary, S. Kleinman, A. Harris and N. Kamani (2016). "Trends in United States blood collection and transfusion: results from the 2013 AABB Blood Collection, Utilization, and Patient Blood Management Survey." Transfusion **56**(9): 2173-2183.

Wright, J. H. (1906). "The Origin and Nature of the Blood Plates." The Boston Medical and Surgical Journal **154**(23): 643-645.

Wright, J. H. (1910). The histogenesis of the blood platelets. Boston.

Wrigth, J. H. (1906). "Die Entstehung der Blutplättchen." Boston Medical Surgery Journal **154**.

Yin, T. and L. Li (2006). "The stem cell niches in bone." The Journal of Clinical Investigation **116**(5): 1195-1201.

Yoon, K. A., H. S. Cho, H. I. Shin and J. Y. Cho (2012). "Differential regulation of CXCL5 by FGF2 in osteoblastic and endothelial niche cells supports hematopoietic stem cell migration." Stem Cells Dev **21**(18): 3391-3402.

Zhang, J., F. Varas, M. Stadtfeld, S. Heck, N. Faust and T. Graf (2007). "CD41-YFP mice allow in vivo labeling of megakaryocytic cells and reveal a subset of platelets hyperreactive to thrombin stimulation." Experimental Hematology **35**(3): 490-499.e491.

Zimmet, J. and K. Ravid (2000). "Polyploidy: Occurrence in nature, mechanisms, and significance for the megakaryocyte-platelet system." Experimental Hematology **28**(1): 3-16.

Zipfel, W. R., R. M. Williams and W. W. Webb (2003). "Nonlinear magic: multiphoton microscopy in the biosciences." Nat Biotech **21**(11): 1369-1377.

Zong, W., J. Zhao, X. Chen, Y. Lin, H. Ren, Y. Zhang, M. Fan, Z. Zhou, H. Cheng, Y. Sun and L. Chen (2014). "Large-field high-resolution two-photon digital scanned light-sheet microscopy." Cell Research **25**: 254.

VII. Appendix

Crosstalk Calculation

File	ROI-Signal in Vessel Channel	ROI-Signal in MK Channel	Factor for Crosstalk Removal (actually used)
20141023_GPIb_day0[…]_893_1	363,01	268,71	0,74
20141023_GPIb_day0[…]_891_1	835,04	447,28	0,78
20141023_GPIb_day0[…]_893_3	415,80	199,62	0,48
20141201_GPIb_day0_[…]_1_1	945,55	258,59	0,27
[…]_GPIb_day5_[…]_3_1	651,28	197,53	0,30
[…]_GPIb_day5_[…]_2_1	540,00	1.788,61	0,33
20141201_GPIb_day0_[…]_8_3	518,64	153,02	0,30
20141201_GPIb_day0_[…]_4_1	319,38	155,32	0,49
[…]_GPIb_day5_[…]_4_1	437,32	169,83	0,39
20141201_GPIb_day0_[…]_7_1	436,47	151,27	0,35
[…]_GPIb_day5_[…]_1_1	331,04	146,44	0,44
20141201_GPIb_day0_[…]_3_1	443,11	223,69	0,51
[…]_GPIb_day7_[…]_3_1	1.020,05	285,29	0,28
[…]_GPIb_day7_[…]_1_3	831,13	279,84	0,34
[…]_GPIb_day7_[…]_5_3	488,84	327,39	0,67
[…]_GPIb_day7_[…]_6_3	580,53	291,01	0,50
[…]_GPIb_day7_[…]_7_3	651,35	367,71	0,57
[…]_GPIb_day5_[…]_8_1	412,06	152,60	0,37
20141201_GPIb_day0_[…]_2_1	701,09	2.360,26	0,34
[…]_GPIb_day5_[…]_7_3	373,93	156,64	0,42
[…]_GPIb_day7_[…]_4_1	659,70	280,85	0,43
(TestFile)_Profilin_[…]_10_1	1.407,60	312,40	0,22
[…]_SdF1a[…]_8_1	1.071,28	383,32	0,36
[…]_SdF1a[…]_5_1	908,80	313,43	0,35
[…]_SdF1a[…]_2_1	719,07	307,72	0,43
[…]_SdF1a[…]_3_2	1.066,14	382,64	0,36
20150313_SdF1a_day2_[…]_6_3	876,66	343,95	0,39
20150313_SdF1a_day2_[…]_7_3	850,48	443,46	0,52
20150313_SdF1a_day2_[…]_4_2	783,77	372,38	0,48
20150313_SdF1a_day2_[…]_11_2	723,24	313,39	0,43

20150422_SdF1a_day1_[…]_5_2	686,39	373,11	0,54
20150422_SdF1a/5D7[…]_7_2	612,64	266,64	0,44
[…]_AMD3100[…]_2_2	620,84	270,43	0,44
[…]_AMD3100[…]_3_2 (1h)	684,13	306,51	0,45
[…]_AMD3100[…]_4_1 (1h)	907,04	198,05	0,22
[…]_femur_day10_[…]_5_1	360,75	271,49	0,75
[…]_RhoA[…]_1_1	651,57	293,20	0,45
[…]_RhoA[…]_5_2	753,87	346,90	0,46
20150210_RhoA[…]_4_2	776,13	357,42	0,42
20150730_femur_[…]_1_2	605,16	241,25	0,48
20150730_femur_[…]_3_1	532,99	255,32	0,48
20150730_femur_[…]_5_2	423,54	170,04	0,40
[…]_femur_[…]_7_2	795,66	382,88	0,48
20150210_RhoA[…]_7_1	810,56	206,40	0,26
20150210_RhoA[…]_6_2	866,35	285,05	0,33
[…]_RhoA[…]_2_1	857,62	338,02	0,39
20150130_Profilin_[…]_8_2_RegionA	1.659,24	314,72	0,19
20150130_Profilin_[…]_8_2_RegionB	1.536,30	318,95	0,21
20150130_Profilin_[…]_11_3_RegionA	1.374,87	273,04	0,20
20150130_Profilin_[…]_8_2_RegionB	1.455,44	294,43	0,20
[…]_RhoA[…]_4_2	815,83	191,95	0,24
20160225_RhoA_[…]_2_1	493,16	175,75	0,36

MW (Factor for Crosstalk Removal)	Max (Factor for Crosstalk Removal)	Min (Factor for Crosstalk Removal)
0,41	0,78	0,19
Stdabw (Factor for Crosstalk Removal)		
0,14		

Table 2: Calculation of vessel crosstalk in MK channel.

VIII. Affidavit / Eidesstattliche Erklärung

Affidavit

I hereby confirm that my thesis entitled *Three-dimensional fluorescence image analysis of megakaryocytes and vascular structures in intact bone* is the result of my own work. I did not receive any help or support from commercial consultants. All sources and / or materials applied are listed and specified in the thesis.

Furthermore, I confirm that this thesis has not yet been submitted as part of another examination process neither in identical nor in similar form.

Place, Date Signature

Eidesstattliche Erklärung

Hiermit erkläre ich an Eides statt, die Dissertation *Dreidimensionale Fluoreszenzbildanalyse von Megakaryozyten und Gefäßstrukturen in intaktem Knochen* eigenständig, d.h. insbesondere selbständig und ohne Hilfe eines kommerziellen Promotionsberaters, angefertigt und keine anderen als die von mir angegebenen Quellen und Hilfsmittel verwendet zu haben.

Ich erkläre außerdem, dass die Dissertation weder in gleicher noch in ähnlicher Form bereits in einem anderen Prüfungsverfahren vorgelegen hat.

Ort, Datum Unterschrift